DOMAIN WALL DYNAMICS IN ION-IMPLANTED MAGNETIC BUBBLE MATERIALS

Thesis by

Timothy Gallagher

In Partial Fulfillment of the Requirements

for the Degree of

Doctor of Philosophy

California Institute of Technology

Pasadena, California

1980

(Submitted May 15, 1980)

Acknowledgements

I would like to express my appreciation to Professor Floyd Humphrey for his help and understanding throughout my stay at Caltech. I would also like to thank Professor Charles Wilts, Dr. Kochan Ju, Dr. Bruce MacNeal, and Kadri Vural for their helpful discussions. I gratefully acknowledge the financial support given to me by the California Institute of Technology, the IBM Corporation, and the National Science Foundation. Finally, I would like to thank Vijaya Korwar and Joyce Liddell for their help in the preparation of the manuscript.

Abstract

The object of this work is to extend the experimental and theoretical understanding of domain wall dynamics in implanted magnetic bubble materials. The presence of the implanted layer was incorporated into the theory of domain wall dynamics by considering both the modified demagnetizing field and the surface pinning associated with the implanted surface. Using this model, calculations of peak wall velocities were made to explain the velocity asymmetry with respect to in-plane field direction. An experimental technique was developed to determine the influence of implantation on bubble state switching, and the results were interpreted using the surface pinning condition. Based on predictions of the model, a new class of bubble states was found in implanted films and the unique dynamic characteristics of these states were investigated.

Table of Contents

Chapter 1

Introduction

Magnetic bubble devices constitute a new information storage technology[1-5]. In a bubble device, data is stored in the magnetic domain structure of a thin ferromagnetic film. With the application of the appropriate magnetic bias field, the domains in these films have the shape of isolated cylinders, called bubbles, as shown in Fig. (1.1). A bubble is simply a region in which the magnetization is antiparallel to that in the surrounding area. As shown in the figure, the magnetization $\overline{M}$ in bubble films is oriented perpendicular to the film plane. Bubbles are typically a few microns in diameter. In order that bubbles be stable, it is necessary to apply a bias magnetic field, H_b, opposite to the direction of the magnetization inside the bubble. Bubbles can be created, destroyed, and moved about the film through the controlled application of localized magnetic fields. In a storage device, bubbles are arranged on the film in the form of a rectangular lattice. A bit of information is thus represented by the presence or absence of a bubble at a particular location in the lattice. The lattice points are created by depositing a soft magnetic structure onto the bubble film, thus forming the required equilibrium positions for the bubbles. To store information, bubbles are created at a nucleation site and transferred to a particular bit location. Conversely, information is accessed by moving the contents of a particular bit location past a detector. The bubble motion required for these operations is produced by the action of an externally-

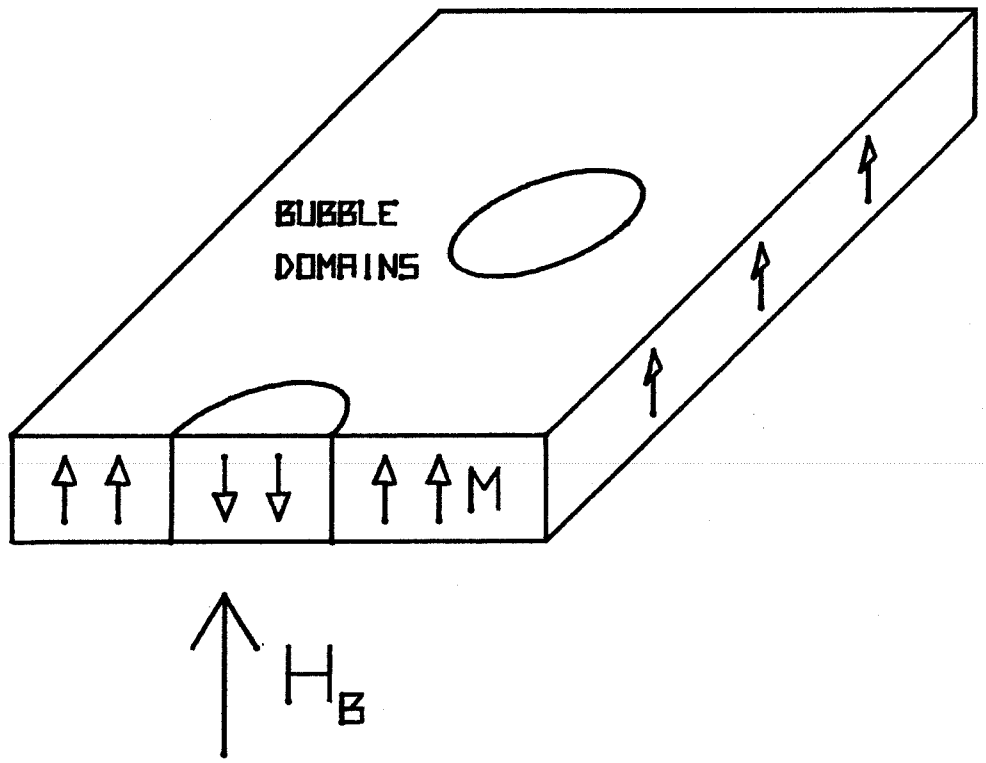

Fig. (1.1). Bubble domains in a thin ferromagnetic film, showing the direction of the magnetization $\overline{M}$ and the applied bias field $\overline{H}_b$.

applied magnetic field, rotating in the plane of the film. The addition of a small number of current lines from the chip to supporting electronics completes the construction of a bubble device.

Bubble devices have a number of desirable characteristics[4]. Unlike other magnetic storage technologies, bubble devices are fully integrated solid-state devices. This results in a highly reliable memory with a small physical size. Requiring one magnetic overlay and one conductor pattern, bubble devices have fewer processing steps than do semiconductor devices. The data in a bubble memory is nonvolatile because the bias field that stabilizes the bubbles is produced by a permanent magnet. Possible applications[5] of bubble devices include microcomputer memories, data terminals, and voice recording systems. New applications can be expected when the particular performance capabilities of bubble devices are fully exploited.

A detailed look at the structure of a bubble device chip is given in Fig. (1.2). Bubble devices typically have a major/minor loop organization. In this type of organization, the array of bit locations is composed of many parallel loops, called minor loops, each of which is a shift register. Each station of the shift register provides an equilibrium position for one bubble. The minor loops are connected with transfer gates to another shift register known as the major loop, where the bubble nucleator[6] and detector[7] are located. When the in-plane field rotates, the bubbles circulate around the loops, moving from one station of the shift register to the next. Newly created bubbles can be transferred from the major loop into the pattern of data in the minor loops. Bubbles in the minor loops can also be

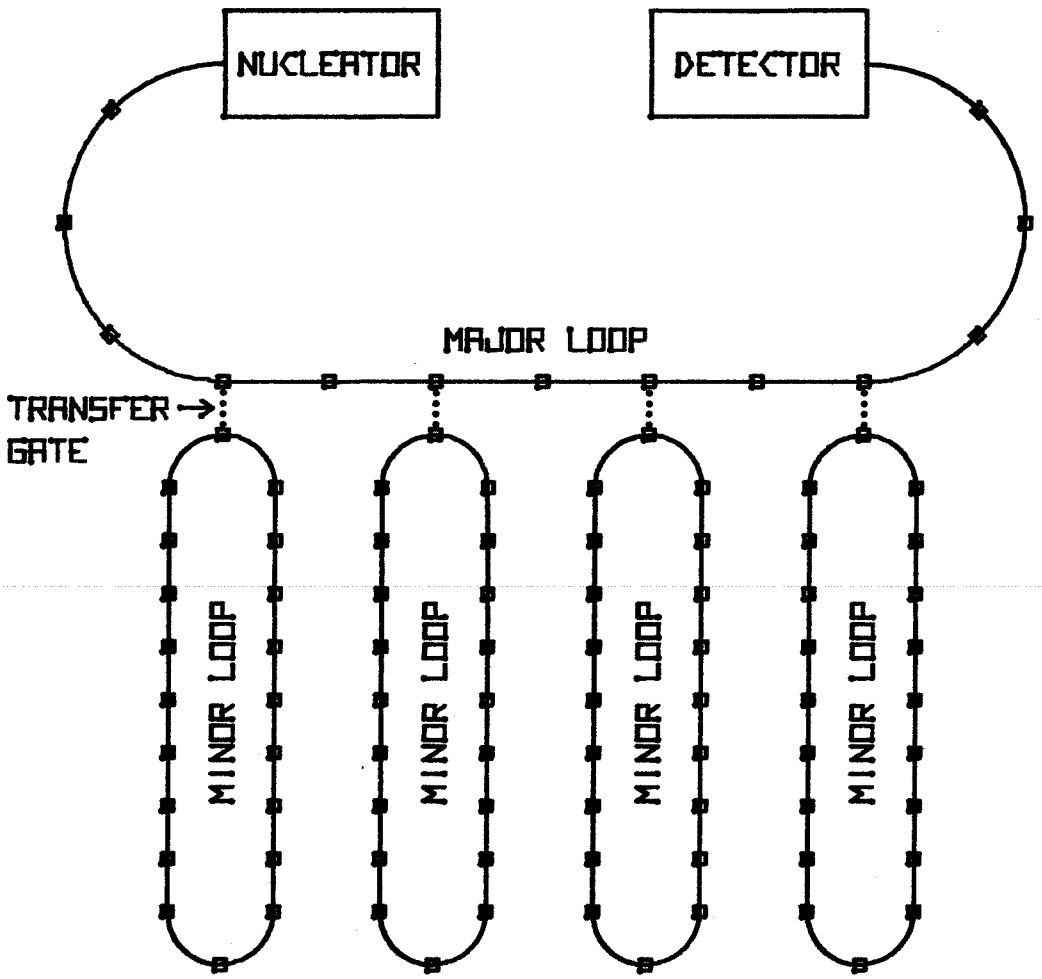

Fig. (1.2). Organization of a bubble device chip.

selectively transferred out of the loop for detection. Each of the nucleation, transfer, and detection functions requires current lines to other electronic circuits in order to carry input or output information. Bubble propagation, however, requires only an external rotating field, a feature that gives bubble devices a particularly simple construction.

The transfer of bubbles between adjacent stations of the shift register is the central part of bubble device operation. The deposited material that makes up the shift register is typically patterned in the form of adjacent asymmetric chevrons[8], as shown in Fig. (1.3), each about 10 μm long. When the in-plane drive field is applied to the film, the chevrons become magnetized. Stray fields emanating from the chevrons can be thought of as due to the presence of induced magnetic charges. These charges attract the bubbles in the underlying film. When the field rotates, the bubble moves across the stations of the shift register as it follows the changing position of the induced charges. As seen in the figure, the magnetic poles (indicated by the + and - signs) induced by the field are located at the ends of the chevrons, along the in-plane field direction. In the case shown here, the orientation of M inside the bubble is such that the bubble is attracted to the negatively charged poles. The figure shows the location of the bubble at different times during one cycle of the rotating field. In the first 180^{o} of field rotation ((a) through (c)), the bubble moves across the chevron as it follows the negative charges. During the final 180^{o} of the cycle, the bubble transfers to the next chevron ((c) through (e)). After 360^{o} of field rotation, the bubble

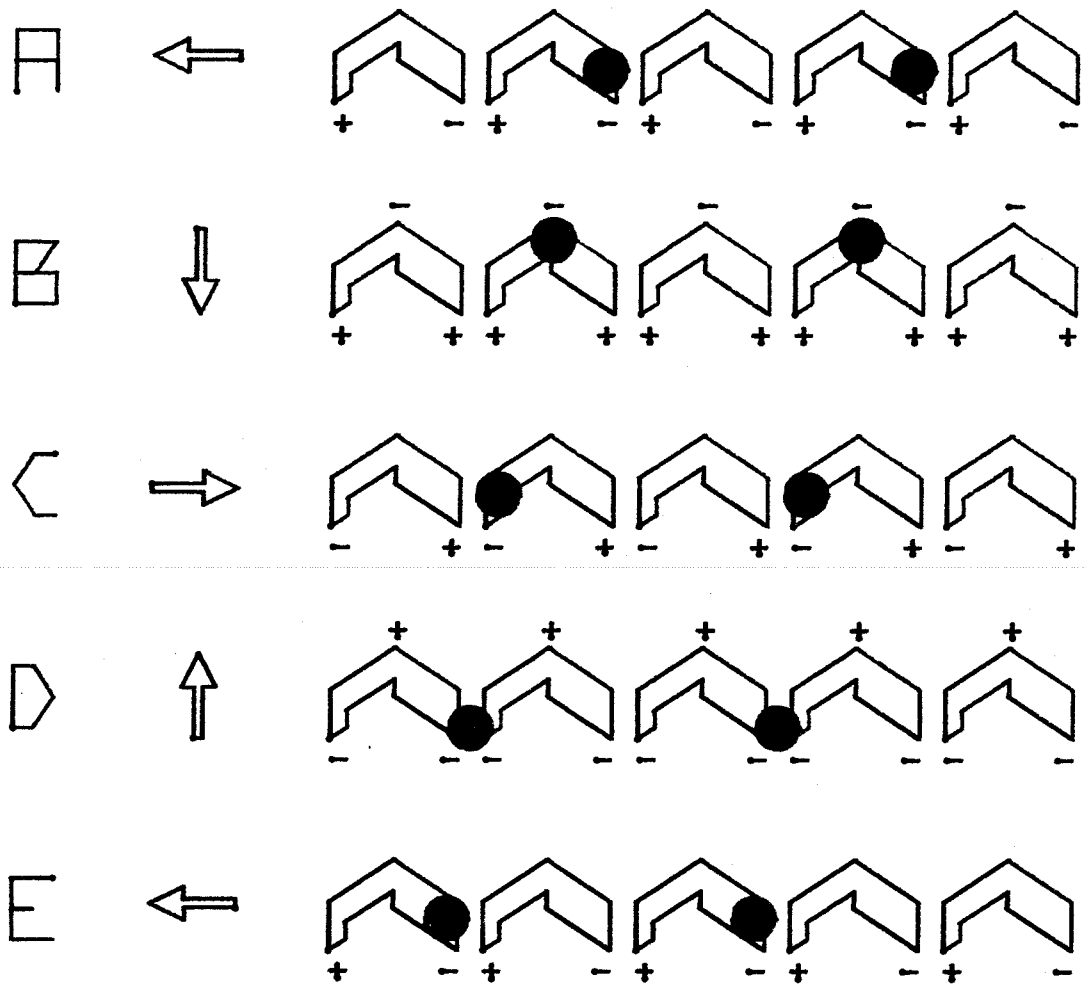

Fig. (1.3). Movement of the bubbles through a shift register. The arrows indicate the direction of the rotating field.

has moved across one chevron of the shift register. The pattern of bubbles in adjacent stations of the shift register remains unchanged.

Device operation imposes certain conditions on the characteristics of the magnetic film[9]. The film must support bubbles which are both small and highly mobile. The existence of bubble domains depends on the presence of a uniaxial anisotropy which orients the magnetization perpendicular to the film plane. The magnitude of the anisotropy must be large enough to overcome the magnetostatic energy, which favors a planar orientation of $\overline{M}$. The required condition is expressed as

$$Q = K/2\pi M^2 > 1 \quad , \qquad (1.1)$$

where K is the increase in anisotropy energy density that results when $\overline{M}$ rotates from an easy direction to a hard direction. Other constraints on K and $\overline{M}$ occur because the bubble velocity is inversely related to $\sqrt{K}$ while the bubble diameter is proportional to $\sqrt{K}/M$ [5]. The film thickness affects both the bubble size and the stability of the bubble shape against distortions. A film thickness of half the desired bubble size is optimum in this respect[10]. Because of these considerations, typical bubble films have $Q \simeq 5$, $4\pi M \simeq 250$ Gauss, and the thickness $h \simeq 2$ μm. These characteristics are significantly different than those of magnetic films studied before the advent of bubble devices. Consequently, a new type of magnetic thin film is required for bubble devices.

Magnetic garnet[11] materials have a number of properties that make them the most commonly used materials for bubble device films.

These garnets have a basic chemical composition of $Q_3R_5O_{12}$, where Q represents one or more rare earth elements and R represents Fe, which is also partially substituted by elements such as Al and Ga. An attractive feature of the garnet system is that the proper combination of rare earths results in a uniaxial anisotropy that is created during film growth. Furthermore, control of the iron content permits the adjustment of the value of the magnetization. Thus the garnet system provides enough flexibility for the control of magnetic properties.

Garnet films have other desirable characteristics. They can be grown epitaxially on a non-magnetic substrate, $Gd_3Ga_5O_{12}$, whose structure is compatible with the magnetic garnets. Thin single crystal device films can thereby be made nearly defect free. Certain film compositions also show relatively little temperature sensitivity. Finally, garnets are transparent to a portion of the visible spectrum, which allows the observation of bubble domains using a magneto-optic phenomenon known as the Faraday effect[12]. This effect causes a rotation of plane polarized light traveling through a magnetic film; the direction of rotation depends on the local orientation of the magnetization. Consequently, bubble domains and their motion can be studied microscopically.

The internal structure of the domain wall has been found to be particularly important in the study of magnetic bubble films[13]. The Bloch wall section is the most elementary of the many possible wall structures. A cross section of the Bloch wall is shown in Fig. (1.4a). In this structure, the magnetic moments (spins) lie in the plane of the

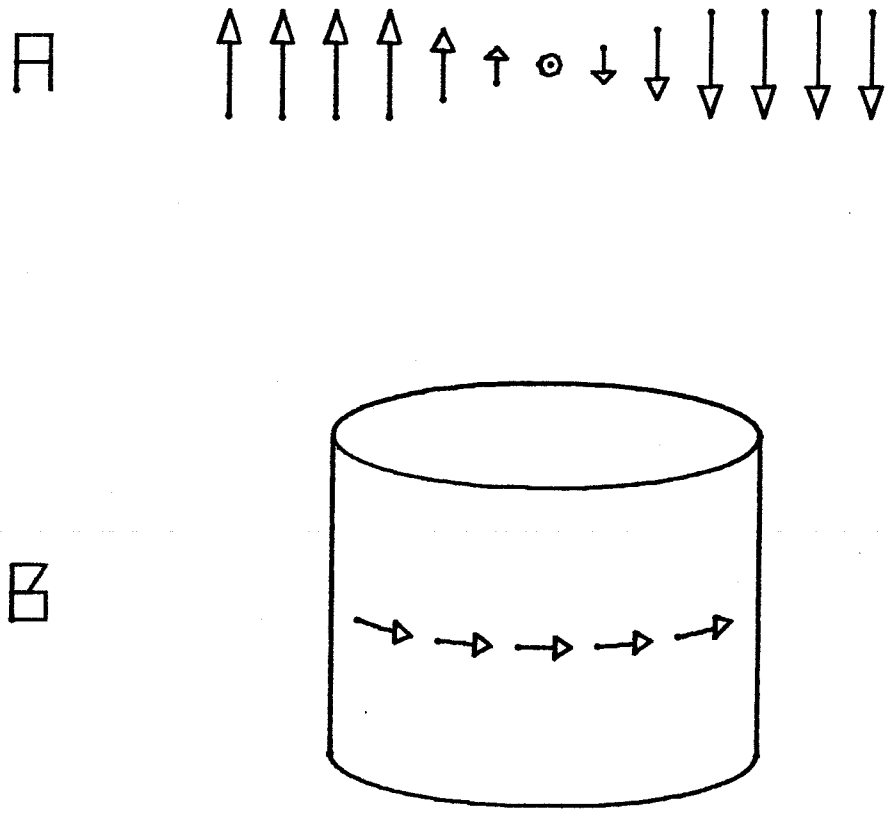

Fig. (1.4). (a) The orientation of spins through a Bloch wall.
(b) One of the unichiral bubbles. The center spins in the wall lie in the plane of the wall, all in the same direction.

domain wall as they rotate between the two antiparallel directions of $\overline{M}$ in adjacent domains. At the center of the wall, the moments are also in the plane of the film. There are two kinds of Bloch walls because the center spin can be oriented in either of the two horizontal directions that are parallel to the domain wall. The particular orientation of the center spin indicates a property of the Bloch wall that is known as its chirality. A bubble whose entire domain wall is composed of a single chirality is called unichiral. One of the unichiral bubbles is shown in Fig. (1.4b). Here, only the center spin in the wall is shown. The other unichiral bubble has its spins directed clockwise around the bubble instead of counterclockwise. These two unichiral bubbles have the simplest wall structures to be found in magnetic bubble films.

More complicated domain wall structures also exist[14,15]. These are shown in Fig. (1.5). The bubble shown in (a) has two adjacent wall sections of opposite chirality. The narrow transition region between them is known as a vertical Bloch line (VBL). The magnetic moments in the center of the VBL are oriented perpendicular to the domain wall. Similar to the VBL is the horizontal Bloch line (HBL), shown in (b). This time the two unichiral sections are located one above the other. The wall structure in a bubble domain may contain any number of twists such as VBL's and HBL's. A specific combination of wall structures in a bubble domain is known as a bubble state. Each bubble state has characteristic dynamic properties.

During wall motion, the internal wall structure changes with time. The simplest case involves the motion of a unichiral bubble. When a

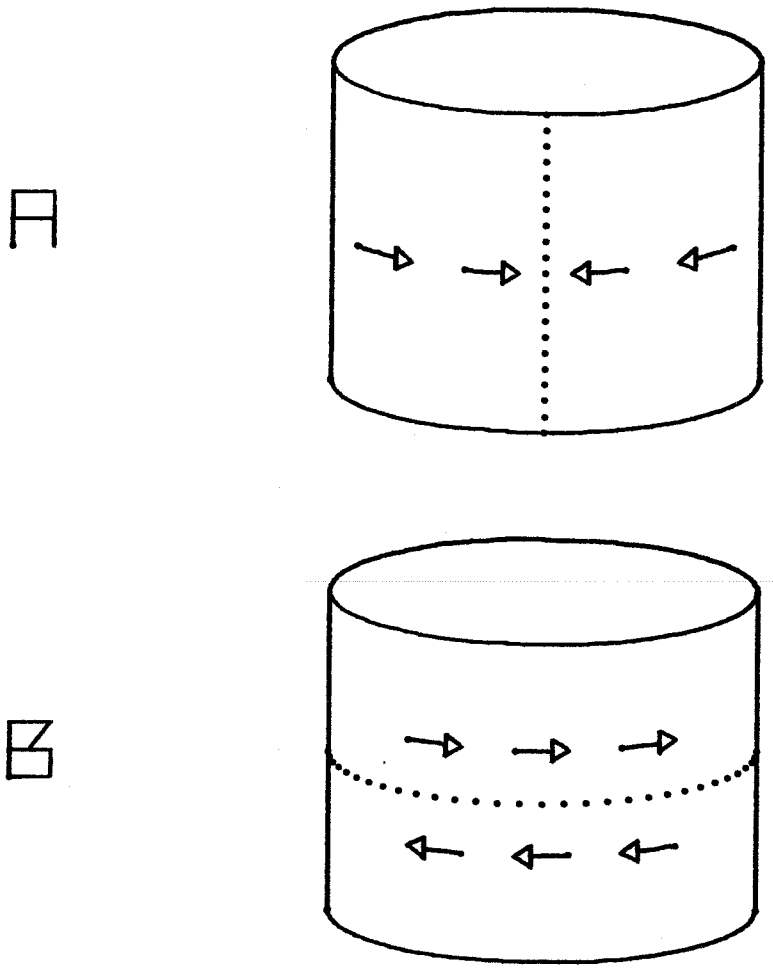

Fig. (1.5). (a) A wall section containing a VBL (shown by the dotted line. (b) A wall section containing an HBL (shown by the dotted line).

pulsed magnetic field is applied to move the bubble, the moments in the domain wall precess out of the plane of the wall. If the drive field is below a certain threshold, the moments will eventually reach an equilibrium orientation. Wall motion with such an unchanging internal structure is called steady-state motion. During steady-state motion, the wall velocity is proportional to the drive field:

$$v = \mu H \quad , \qquad (1.2)$$

where H is the drive field and μ is a constant, called the mobility, whose value depends on the material properties of the film. Above a certain critical drive field, however, the velocity no longer increases linearly. Instead, it remains relatively constant upon further increases in drive field. This change of the velocity characteristic at the critical drive field is called breakdown and is associated with changes in the internal wall structure. Above the critical drive field, the uniformly rotated wall no longer exists during the motion. Instead, the wall structure continually changes in a process which involves the periodic nucleation of an HBL and its propagation through the film thickness[16]. Reduced domain wall velocities always accompany the presence of HBL's in the domain wall. Thus, the onset of HBL nucleation is related to the peak velocity at which bubbles can move.

Vertical Bloch lines also lower the wall velocity, to an extent depending on the number of VBL's in the bubble. Bubbles with closely-packed VBL's, called hard bubbles, have a wall velocity that is

typically two or three orders of magnitude less than that of a unichiral bubble. Hard bubbles disrupt device operation. Since a unichiral bubble can be transformed into a hard bubble during wall motion, some method is required to prevent the conversion of bubbles into these undesirable states.

Hard bubbles do not exist in garnet films that have been properly ion-implanted. The implantation process[17] typically consists of bombarding the film with 100 keV Ne^+ ions. The implantation creates a 0.2 μm damaged layer at the film surface. After implantation, the magnetic properties of the surface are altered. An in-plane anisotropy replaces the original growth-induced perpendicular anisotropy. Thus the magnetic moments in the implanted layer lie in the plane of the film. The in-plane layer acts as a kind of boundary condition to the bulk of the film, limiting the amount of different wall structures that can exist in a bubble. In particular, hard bubbles can not be formed. Consequently, ion implantation is universally applied to bubble device films.

Implantation affects a number of other bubble state transitions aside from those involving hard bubbles. This feature of implantation in fact allows a great deal of control over the production of selected bubble states. Such a control has led to the development of unconventional device concepts. An example of this is the so-called bubble lattice file[18]. In this device, bit information is not represented as the presence or absence of a bubble. Instead, a bubble exists at every station of the shift register while the information is stored in the

form of the bubbles' wall structure. Bit information is accessed by capitalizing on the dynamic behavior of the two states. In such unconventional device schemes, the interaction between the wall structure and the implanted layer becomes crucially important.

A good understanding of the behavior of bubbles in devices rests upon a knowledge of the internal structure of the domain wall. Specific dynamic behavior is associated with particular kinds of wall structure. Ion implantation, necessary for good device operation, affects both the static and dynamic wall structure.

References

1. A. H. Bobeck, P. I. Bonyhard, and J. E. Geusic, IEEE Proc. 63, 1176 (1975).
2. A. H. Bobeck and H. E. D. Scovil, Scientific American 224, 78 (June, 1971).
3. A. B. Smith, Bubble-Domain Memory Devices (Artech House, Dedham, Mass., 1974).
4. Magnetic Bubble Technology: Integrated-Circuit Magnetics for Digital Storage and Processing, ed. Hsu Chang, (IEEE Press, New York, 1975).
5. Hsu Chang, Magnetic-Bubble Memory Technology (Marcel Dekker, New York, 1978).
6. A. H. Bobeck, Bell Sys. Tech. J. 46, 1901 (1967).
7. L. R. Tocci, P. K. George, and J. L. Archer, AIP Conf. Proc. 10, 197 (1972).
8. A. H. Bobeck, R. F. Fisher, and J. L. Smith, AIP Conf. Proc. 5, 45 (1971).
9. J. W. Nielsen, IEEE Trans. MAG-12, 327 (1976).
10. A. A. Thiele, J. Appl. Phys. 41, 1139 (1970).
11. L. K. Shick, J. W. Nielsen, A. H. Bobeck, A. J. Kurzig, P. C. Michaelis, and J. P. Reekstin, Appl. Phys. Lett. 18, 89 (1971).
12. R. Carey and E. D. Isaac, Magnetic Domains and Techniques for Their Observation, (Academic, New York, 1966).
13. A. P. Malozemoff and J. C. Slonczewski, Magnetic Domain Walls in Bubble Materials, (Academic, New York, 1979).

14. A. P. Malozemoff, Appl. Phys. Lett. 21, 190 (1972).

15. G. P. Vella-Coleiro, A. Rosencweig, and W. J. Tabor, Phys. Rev. Lett. 29, 949 (1972).

16. B. E. Argyle, J. C. Slonczewski, and A. E. Mayadas, AIP Conf. Proc. 5, 175 (1972).

17. R. Wolfe and J. C. North, Bell. Sys. Tech. J. 51, 1436 (1972).

18. B. R. Brown, R. A. Burn, A. M. Desouches, D. M. Hannon, T. Hsu, C. Y. Liu, E. G. Moore, D. Y. Saiki, and W. E. Weresin, IEEE Trans. MAG-15, 1501 (1979).

Chapter 2

The Theory of Domain Wall Structure and Motion

A mathematical model can be created for the study of domain wall structure and motion. In the model[1], a continuous vector function of space and time is used to describe the orientation of $\overline{M}$, the magnetic moment per unit volume. The magnitude of $\overline{M}$ is considered to be independent of its direction. The objective of the analysis is the specification of the orientation of $\overline{M}$ throughout the domain wall. For a determination of static structure, this is done by considering the various potential energies associated with the magnetic structure of the garnet film. There are three sources of potential energy. First, an exchange energy arises because of the interaction between neighboring magnetic moments, which favors a parallel alignment of the moments. Second, there is a uniaxial anisotropy energy whose easy axis is along the film normal. Finally, there is the magnetostatic energy, which is produced both by external fields and by fields arising from the magnetic structure itself. For a determination of the instantaneous dynamic structure, two other magnetic characteristics become important. Associated with $\overline{M}$ is an angular momentum $\overline{L}$ which gives rise to the gyroscopic nature of magnetization dynamics. The magnitude of $\overline{L}$ is equal to M/γ, where γ, called the gyromagnetic ratio, is a constant of the material. Dynamic processes also entail a transfer of energy to the lattice. In the model, this process is incorporated through the use of a phenomenological damping parameter, α, which relates energy loss to $\dot{\overline{M}}$. The specification of these few parameters allows the construction of a mathematical model

to describe domain wall structure and dynamics.

2.1 Static wall structure

The equilibrium magnetic configuration inside the domain wall is found by minimizing the total energy. Particular expressions for each term of the energy are made using the coordinate system shown in Fig. (2.1). A polar angle θ and azimuthal angle ϕ specify the orientation of the magnetic moment at each point $\bar{r}$ in the material. The z axis coincides with the film normal. The total energy is the sum of contributions from exchange, anisotropy, external fields and internal demagnetizing fields. The standard expressions[1,2] for the energy densities are written in the following way. Exchange energy density is expressed as

$$w_{ex} = A\{\nabla\theta\cdot\nabla\theta + \sin^2\theta(\nabla\phi\cdot\nabla\phi)\} \quad , \qquad (2.1)$$

where A is the exchange constant. The uniaxial anisotropy has an associated energy density of

$$w_{an} = K\sin^2\theta \quad , \qquad (2.2)$$

where K is a constant. Energy due to an externally applied field $\bar{H}$ is

$$w_H = -\bar{M}\cdot\bar{H} \quad , \qquad (2.3)$$

while the demagnetizing field $\bar{H}_d$, produced by the divergence of the magnetization, gives a contribution to the energy of

$$w_d = -\frac{\bar{M}\cdot\bar{H}_d}{2} \quad . \qquad (2.4)$$

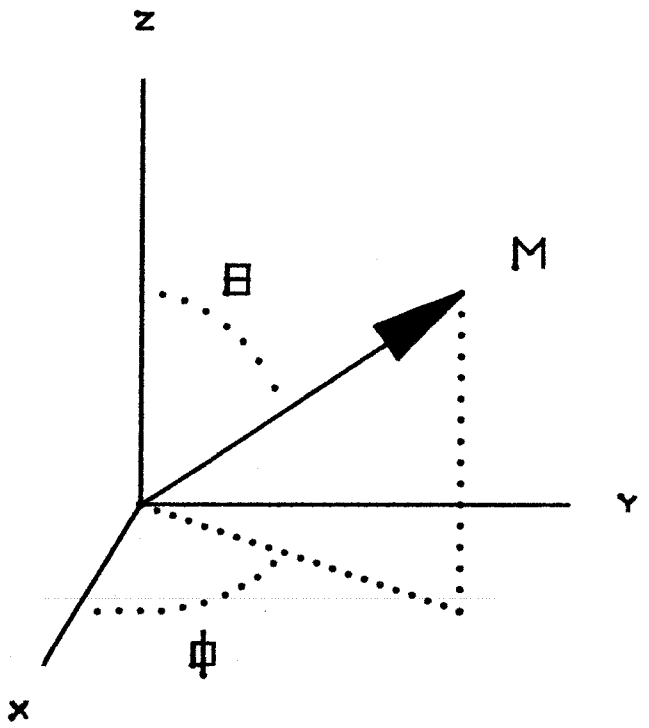

Fig. (2.1). The spherical polar coordinate system. The angles θ and ϕ specify the orientation of $\overline{M}$ while (x,y,z) specifies the location in the material.

A determination of the form of the demagnetizing field completes the specification of the total energy.

The magnetic structure is found in the standard way by equating the total torque equal to zero and solving the resulting equation. Because the total energy depends on the spatial derivatives of $\overline{M}(\overline{r})$ as well as on $\overline{M}$ itself, techniques from the calculus of variations[3] must be used to give the conditions for zero torque. The two conditions are

$$\frac{\delta w}{\delta \theta} = 0 \qquad (2.5a)$$

and

$$\frac{\delta w}{\delta \phi} = 0 \quad , \qquad (2.5b)$$

where w is the total energy and $\frac{\delta}{\delta \theta}$ is the functional derivative defined by

$$\frac{\delta}{\delta \theta} = \frac{\partial}{\partial \theta} - \nabla \cdot \frac{\partial}{\partial\, \nabla \theta} \quad . \qquad (2.6)$$

Each of the two conditions (2.5) is a differential equation which is, in general, nonlinear. The variables ϕ and θ are functions of the three coordinates. Boundary conditions for these equations will be apparent from consideration of the particular physical situation. In theory, the two simultaneous differential equations could be solved for the exact three dimensional magnetic configuration.

In the absence of fields from external sources and nonlocal internal sources, the problem reduces to a particularly simple one that can be solved analytically. For example, one can solve for the magnetic

structure of a 180^{o} domain wall of infinite extent, where the material surfaces are considered to be far enough away so as to have no effect on the wall structure. Although this is a somewhat artificial situation, it illustrates the basic domain wall structure. Because the energy expressions remain the same at different points along the surface of the domain wall, the equations become one-dimensional. Nonzero exchange terms occur only for the direction perpendicular to the wall. For convenience, a wall located in the x-z plane is considered. The boundary conditions are $\theta = 0$ as $y \to -\infty$ and $\theta = \pi$ as $y \to +\infty$, thus representing the fact that the moments are aligned with the film normal far from the wall. There are no conditions on ϕ since it is undefined when $\theta = 0,\pi$. The total energy consists of three terms (2.1, 2.2, and 2.4) with the demagnetizing energy written explicitly as

$$w_d = 2\pi M^2 \sin^2\theta \sin^2\phi \quad . \qquad (2.7)$$

Equations (2.5a) and (2.5b) now become

$$-2A\frac{d^2\theta}{dy^2} + A\sin 2\theta\left(\frac{d\phi}{dy}\right)^2 + K\sin 2\theta + 2\pi M^2 \sin 2\theta \sin^2\phi = 0 \qquad (2.8)$$

and

$$-2A\sin^2\theta\,\frac{d^2\phi}{dy^2} - 2A\sin 2\theta\left(\frac{d\theta}{dy}\,\frac{d\phi}{dy}\right) + 2\pi M^2 \sin^2\theta \sin 2\phi = 0 \quad . \qquad (2.9)$$

These two equations describe the static one-dimensional wall structure.

Inspection of Eqs. (2.8) and (2.9) suggests a particular form for $\phi(y)$, which then leads to an exact solution of the equations. If ϕ is assumed constant in y, then the equations are simplified to

$$-2A\,\frac{d^2\theta}{dy^2} + (K + 2\pi M^2 \sin^2\phi)\sin 2\theta = 0 \qquad (2.10)$$

$$\sin^2\theta \sin 2\phi = 0 \quad . \qquad (2.11)$$

The second equation has the solution $\phi = \frac{n\pi}{2}$, where n is an integer. Further calculation shows that the solution giving an energy minimum are $\phi = 0,\pi$. The first equation can then be solved by integration to give the so-called Bloch wall[4] configuration:

$$\theta(y) = 2\tan^{-1}(\exp(\frac{y}{\sqrt{A/K}})) \quad , \qquad (2.12)$$

which specifies the orientation of the spins as a function of distance from the center of the wall.

The Bloch wall configuration is the most elementary domain wall structure that can occur in magnetic materials. It is illustrated in Fig. (2.2). In (a), a diagram of the spin orientations in a cross section of the domain wall is shown. On either side of the wall, the moments are aligned along the film normal. Inside the wall, as the spin orientation rotates by 180^o, the spins remain oriented in the plane of the wall. The center spin in the wall can be directed in either of the two directions parallel to the film surface. The spin orientation is shown quantatively in (b), in which the polar angle of the spin orientation, given by Eq. (2.12), is plotted as a function of distance through the domain wall. At the center of the wall, the slope of the distribution $\frac{d\theta}{dy} = \frac{1}{\sqrt{A/K}} \equiv \frac{1}{\Delta}$. Thus the entire 180^o rotation of the spins occurs in a distance of about $\pi\Delta$, which is on the order of 0.15 μm for typical bubble materials.

A more complicated situation than that just considered involves

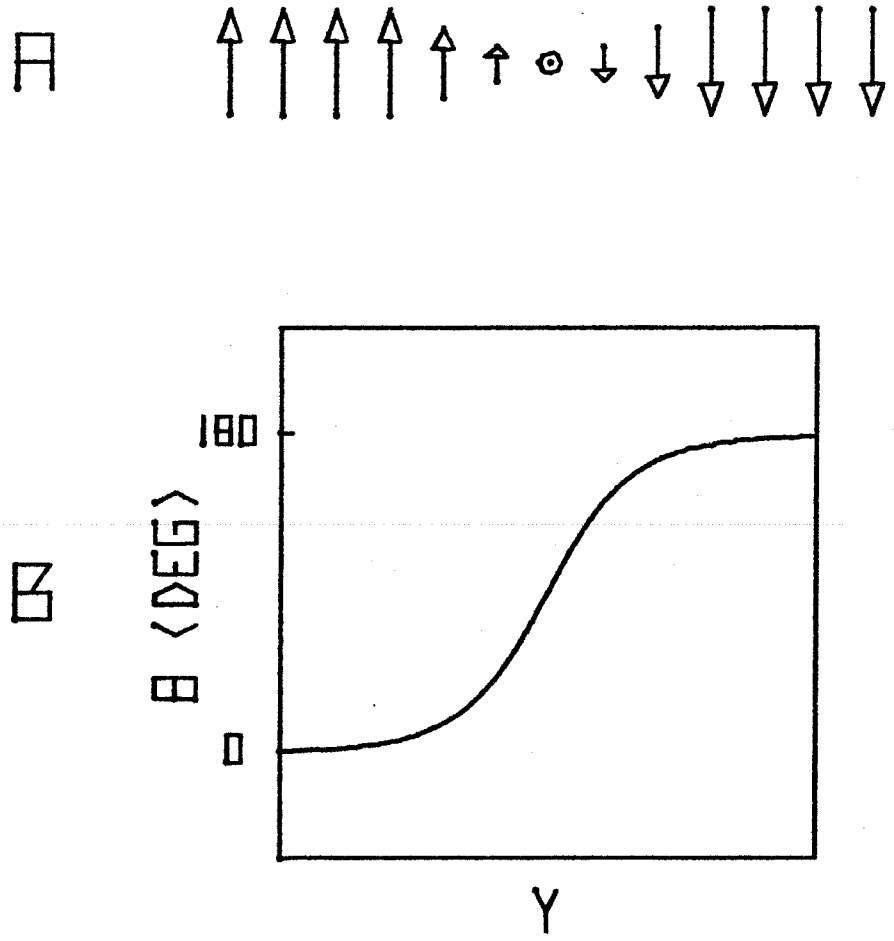

Fig. (2.2). (a) A cross sectional view of the spin orientation in the Bloch wall. (b) A graph of the value of the polar angle as a function of distance through the Bloch wall.

the presence of a uniform in-plane field H_1. Although the problem is still one-dimensional, it is too complicated to allow an exact analytical solution because ϕ cannot be strictly constant through the wall. This becomes evident upon analysis of the differential equations when the additional torque due to the in-plane field is added:

$$-2A\frac{d^2\theta}{dy^2} + A\sin 2\theta\left(\frac{d\phi}{dy}\right)^2 + K\sin 2\theta + 2\pi M^2\sin^2\theta\sin^2\phi$$

$$-MH_x\cos\theta\cos\phi - MH_y\cos\theta\sin\phi = 0 \qquad (2.13)$$

and

$$-2A\sin^2\theta\left(\frac{d^2\phi}{dy^2}\right) - 2A\sin 2\theta\left(\frac{d\theta}{dy}\frac{d\phi}{dy}\right) + 2\pi M^2\sin^2\theta\sin 2\phi$$

$$+ MH_x\sin\theta\sin\phi + MH_y\sin\theta\sin\phi = 0 \quad , \qquad (2.14)$$

where H_x and H_y are the components of the in-plane field. Setting ϕ constant in the equations does not give a solution. Even though the Eqs. (2.13) and (2.14) could be solved numerically, such a solution would not lend itself for applications. An approximate solution to these equations, made flexible with a few parameters, is most useful. Such a solution can be created by making the assumption that $\theta(y)$ is not affected by the in-plane field. This assumption is good because the exchange and anisotropy energies are on the order of Q times the size of the typical magnetostatic energies. Thus the $\theta(y)$ structure will be dominated by exchange and anisotropy energies for the typical high Q materials. On the other hand, the value of ϕ does depend on the applied in-plane field. If it is assumed that ϕ is constant and that $\theta(y)$ is given by Eq. (2.12), then the equilibrium value of ϕ can be found by

minimizing the total wall energy as a function of ϕ. The result is

$$H_x \sin\phi - H_y \cos\phi + 4M \sin 2\phi = 0 \quad . \qquad (2.15)$$

The effect of the in-plane field on the value of ϕ is shown in Fig. (2.3), for the case where the in-plane field is perpendicular to the wall ($H_x = 0$). In (a), the coordinate system is shown. In (b), the solution to Eq. (2.15) is plotted as a function of in-plane field magnitude. Without the in-plane field, the spins lie in the plane of the wall ($\phi = 0$). For nonzero fields, the spins lie at an angle to the wall. If the in-plane field is above 8M, the spins are perpendicular to the wall. In-plane fields therefore strongly affect the azimuthal orientation of the magnetic moments in the domain wall, while the polar orientation remains unchanged.

In magnetic bubble films, the effects of the finite film thickness must be considered. Internal demagnetizing fields become important because the boundaries of the magnetic material are not infinitely distant. A cross sectional view of a bubble film is shown in Fig. (2.4a). The magnetization is perpendicular to the film surfaces and therefore an effective surface magnetic charge density exists. Its magnitude is $\bar{M} \cdot \hat{n}$, where $\hat{n}$ is a unit vector along the outward film normal. As shown in the figure, the charge density at a particular surface changes sign across a domain wall. Consequently, the demagnetizing (stray) field H_s at a surface near a domain wall is oriented in the film plane, perpendicular to the wall. It can be seen that the stray fields at the two film surfaces are in opposing directions. The magnitude of the stray field

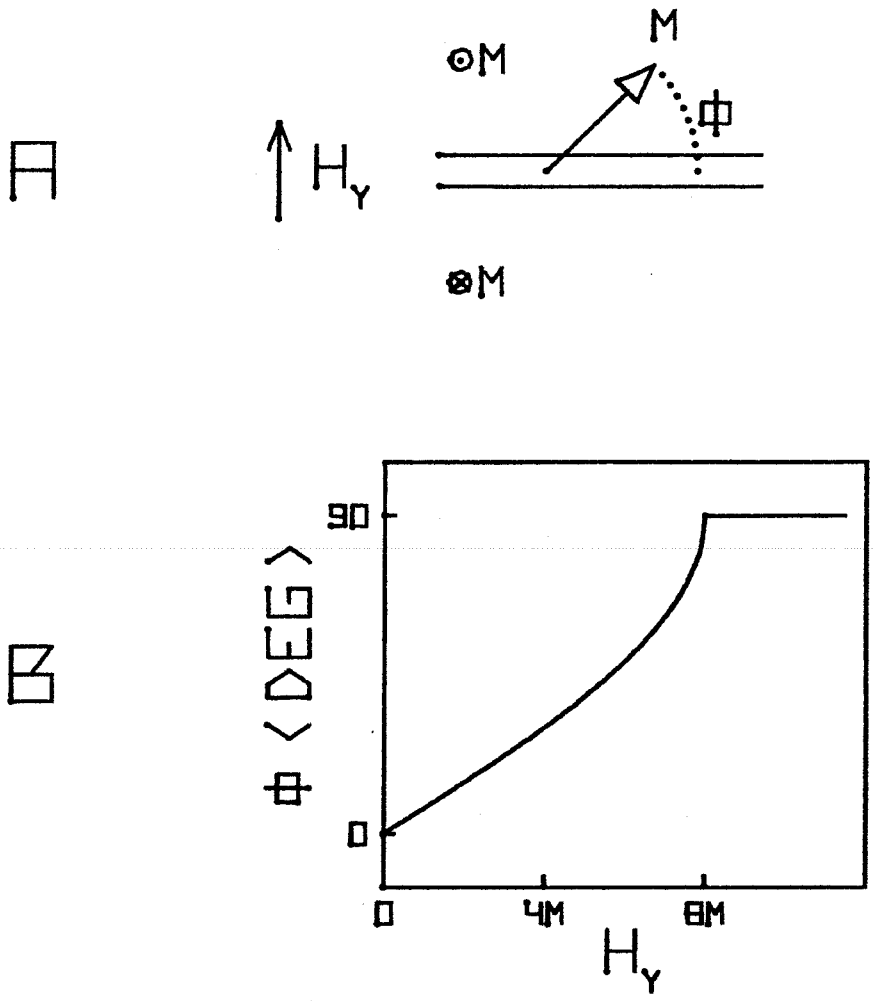

Fig. (2.3). (a) The coordinate system, showing the orientation of the in-plane field. (b) The azimuthal angle ϕ is plotted as a function of the magnitude of the applied field.

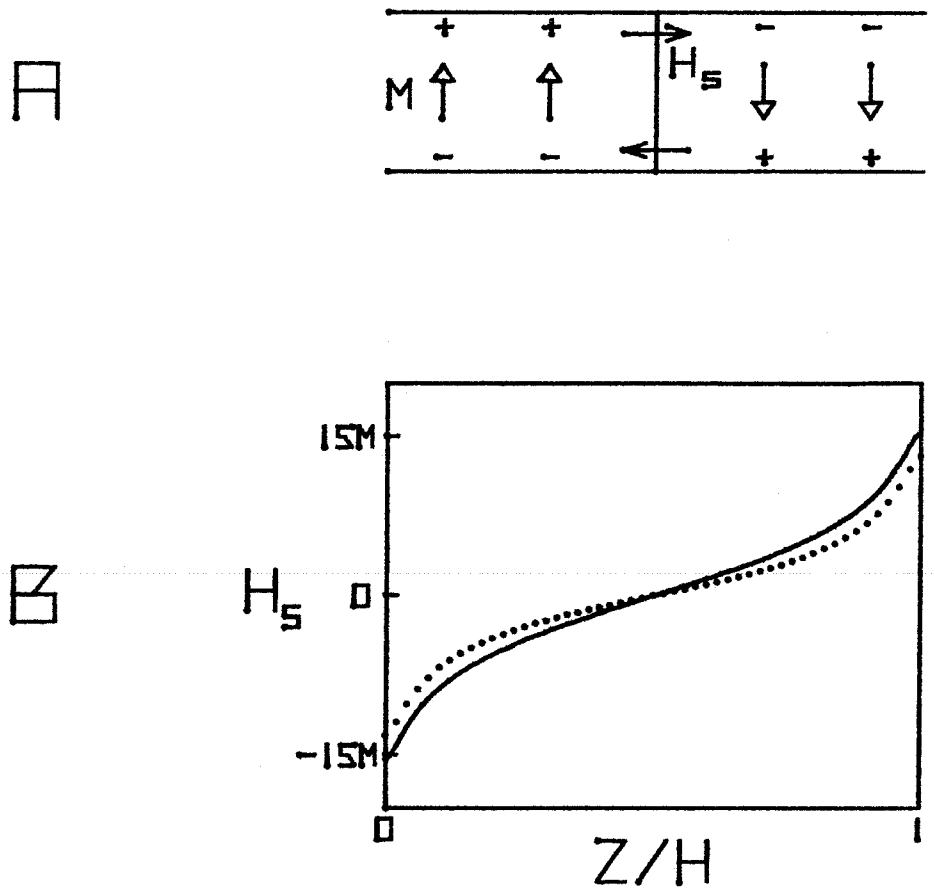

Fig. (2.4). (a) The orientation of the stray field H_s at a domain wall. (b) The magnitude of the stray field at the wall, as a function of position. The solid line is for an isolated wall while the dotted line is for a 5 μm diameter bubble in a 4 μm thick film.

at the wall thus varies through the film thickness.

The magnitude of the stray field at the wall as a function of position through the film thickness is shown by the solid line in Fig. (2.4b). Equal to zero at the mid-plane of the film, the field increases rapidly towards the film surfaces. Mathematical expressions for the stray field involve a two-dimensional integration over the surface charges. The result[5] for an isolated straight wall is

$$H_s = 4M \ln\left(\frac{z}{z-h}\right) \quad . \tag{2.16}$$

This expression includes an unphysical singularity at each surface because the wall width was assumed to be zero in the derivation. A coordinate transformation[6], which affects only the values close to the surfaces, is commonly used to suppress the singularity. This results in a peak surface field of about 15M, which is typically 250 Oe. The presence of the strong stray field is a complicating factor which certainly affects the static wall structure. Consequently, a one-dimensional model cannot describe bubble wall structure.

Approximate solutions for the total wall structure, including the effect of the stray field, can be obtained. Because the stray field changes through the film thickness, ϕ also changes with position. Consequently, the exchange energy due to changes in ϕ in the z direction must be considered. Including this effect into the analysis gives a model[7,8] which is realistic enough to apply to physical situations. The model still has the same assumptions described earlier, namely that $\theta(y)$ always has the same form as expressed in Eq. (2.12) and that ϕ is constant through the wall. The domain wall is assumed flat. Finally, it is

assumed that changes in ϕ along the z direction are small over a distance equal to the wall width. This condition insures that the local demagnetizing energy at the wall retains the simple form given by Eq. (2.7). With these assumptions, the wall structure is characterized solely by $\phi(z)$. The condition for static stability, Eq. (2.5b), can be written explicitly as

$$\frac{-A}{\pi M^2}\frac{d^2\phi}{dz^2} + \sin 2\phi + \frac{H_x}{4M}\sin\phi - \frac{(H_s + H_y)}{4M}\cos\phi = 0. \quad (2.17)$$

This is an expanded version of Eq. (2.15), which did not include the stray field or the exchange term. Because there are no surface anisotropies, the boundary condition for this differential equation is $\frac{d\phi}{dz} = 0$ at each film surface. The equation must be solved numerically.

The numerical technique used to solve the differential equation is essentially an iterative Newton's method[6]. Given an initial trial solution, the deviations from the exact solution are expressed by a linearized equations. The linear equation is solved by dividing the film thickness into typically 100 points, replacing the derivatives by the appropriate finite difference expressions, and solving in the standard way. The trial solution is adjusted by the calculated deviations to construct a new trial solution. Repetition of this procedure continues until sufficient accuracy (e.g., 1 part in 10^6) is obtained. Usually, convergence is rapid enough so that only a few iterations are required to determine the wall structure.

Wall structure obtained by the numerical method outlined above is shown in Fig. (2.5). When the surface stray field is the only field

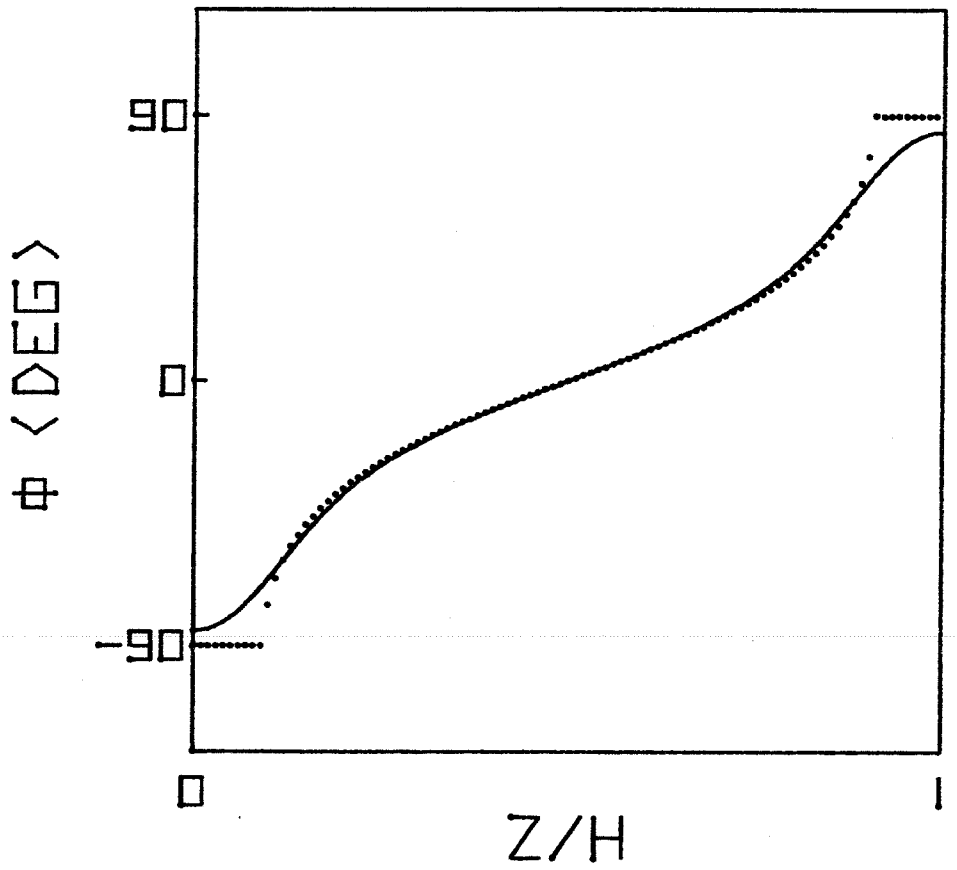

Fig. (2.5). The azimuthal angle of the spin orientation is plotted as a function of distance through the film thickness. The dotted line shows the magnetostatic minimum.

present, the wall structure assumes a shape such as that shown by the solid line. The stray field for 5 μm bubbles in a 4.1 μm thick film was used (shown by the dotted line in Fig. (2.4b)). The solution is nearly equal to the magnetostatic minimum (dotted line), that is, the solution to the problem if exchange energy is neglected in the z direction. For typical bubble films, the presence of the exchange interaction simply smooths out the curve given by the magnetistatic minimum. The extent to which it does so is determined by the magnitude of the parameter $\pi M^2 h^2/A$; for the case shown here the value is equal to 539 (P206). Another curve also satisfies the differential equation and the boundary conditions. The reflection of the solution in Fig. (2.5) across the $\phi = 90^o$ line produces this other solution. This corresponds to the opposite wall chirality. In either case, the stray field produces a twisting wall structure like that shown in the figure.

Externally applied fields modify wall structure. If, for example, an in-plane field is applied perpendicular to a domain wall, then the in-plane field competes with the stray field, changing the magnetostatic minimum. A typical solution, for which $H_y = 2\pi M = 90$ Oe, is shown by the solid curve in Fig. (2.6). As before, the curve essentially follows the magnetostatic minimum (dotted line). At the top film surface (z=h), the combined field is strong enough to align a large portion of the curve along the field direction. At the bottom surface, the total field is reduced by the in-plane field. Consequently, the value of ϕ at the bottom surface does not reach its previous value of nearly -90^o, as it did without the in-plane field. If the in-plane field is larger than the peak stray field (roughly 15M = 215 Oe for the film P206), then all

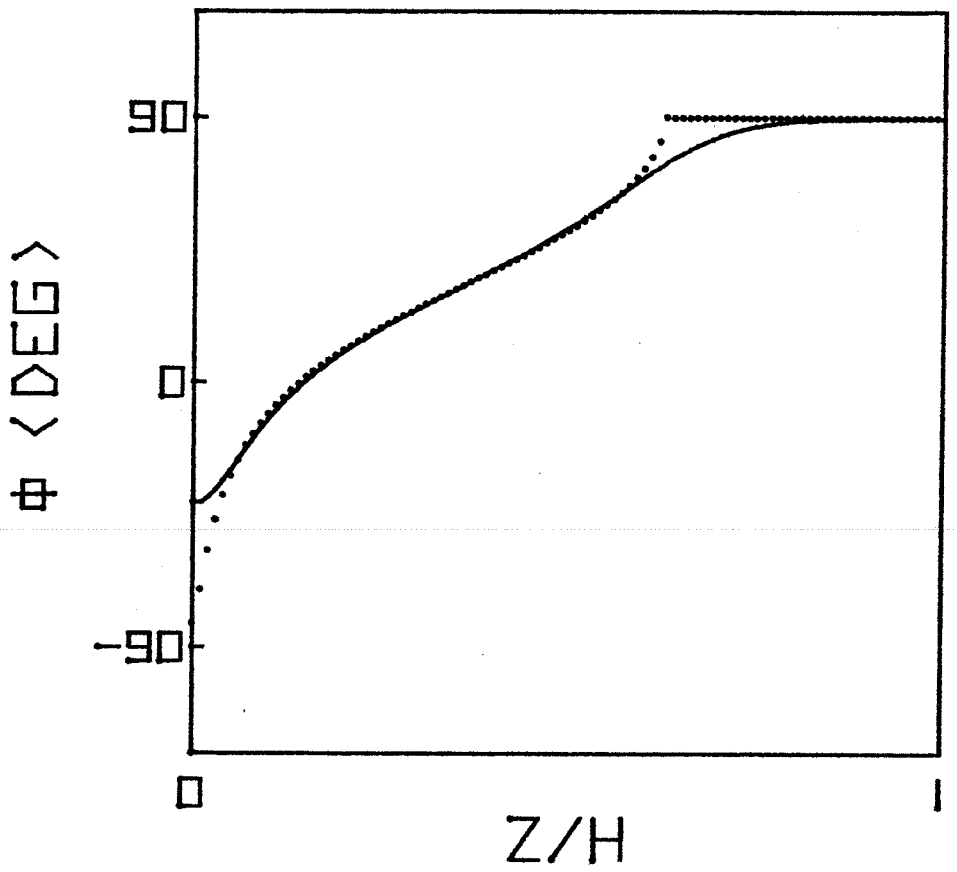

Fig. (2.6). The azimuthal angle of the spin orientation plotted as a function of position through the film thickness for $H_y = 2\pi M = 90$ Oe. The dotted line shows the magnetostatic minimum.

all the moments will be aligned along the in-plane field at $\phi = 90^{o}$. For in-plane fields less than 15M, the field reduces but does not destroy the wall twist produced by the surface stray field.

In summary, the determination of the static wall structure involves the specification of $\theta(\bar{r})$ and $\phi(\bar{r})$. Because of the overwhelming size exchange and anisotropy energies for changes in θ through the wall, $\theta(y)$ is essentially independent of ϕ. The specification of $\phi(z)$ defines the wall structure. Domain walls in real bubble films do not have a one-dimensional structure because of the presence of the surface stray field. The structure of a unichiral domain wall therefore has a twist through the film thickness. The application of in-plane fields modifies the wall structure, reducing the twist if the field is applied perpendicular to the domain wall.

2.2 Domain wall dynamics

The study of domain wall motion has as its starting point the phenomenological model proposed by Landau and Lifshitz[4]. In this model, the magnetic moment precesses in response to an effective magnetic field, $\bar{H}_{eff}$. As in classical mechanics, the time rate of change of the angular momentum associated with the moment is equal to the torque. This gives the classical expression for spin precession:

$$\dot{\bar{L}} = \frac{-\dot{\bar{M}}}{|\gamma|} = \bar{M} \times \bar{H}_{eff} \quad . \tag{2.18}$$

This model also incorporates relaxation effects, which cause the eventual alignment of $\bar{M}$ with the applied field. An additional torque is therefore

required to describe the damping. Landau and Lifshitz proposed a torque of the form $\overline{M} \times (\overline{M} \times \overline{H}_{eff})$. An alternate form, $\overline{M} \times \dot{\overline{M}}$, that was proposed by Gilbert[9] is more commonly used. For small damping, the two forms are equivalent. Thus the complete equation governing the dynamic behavior of the magnetization is

$$\dot{\overline{M}} = -|\gamma|(\overline{M} \times \overline{H}_{eff}) + \frac{\alpha}{M}(\overline{M} \times \dot{\overline{M}}) \quad . \qquad (2.19)$$

This is called the Landau-Lifshitz-Gilbert (LLG) equation.

Applying the LLG equation to dynamic problems involving complex three-dimensional spin structures necessitates a number of simplifying assumptions. As was assumed for the static case, the polar angle θ follows the Bloch wall shape. Although originally proposed for static situations, this is also true during wall motion because the additional dynamic torques are small. The azimuthal angle ϕ is again considered to be constant through the wall. As before, rapid changes of ϕ in distances along the wall equal to about a wall width are not considered in order that the demagnetizing field retains the simple form used previously. Wall bulging is neglected. With the use of these assumptions, the model is simple enough to use yet realistic enough to apply to a number of physical problems.

The equations of wall motion for a general three-dimensional wall can be derived using a Lagrangian formulation for the magnetic system.[1,10,11] This approach involves the definition of a Lagrangian function L and a dissipation function F, which are used to produce the equations of motion via Hamilton's variational principle. Specifically, L is defined

as the kinetic energy density minus the potential energy density. The dissipation function F is proportional to the rate of energy loss to the lattice during wall motion. Once L and F are specified, standard techniques from the calculus of variations transform the integral form of Hamilton's principle into the differential equations of motion[1,3], which are

$$\frac{d}{dt}\left(\frac{\partial L}{\partial \dot{\xi}_i}\right) + \sum_{j=1}^{3} \frac{d}{dx_j}\left[\frac{\partial L}{\partial\left(\frac{\partial \xi_i}{\partial x_j}\right)}\right] - \frac{\partial L}{\partial \xi_i} + \frac{\partial F}{\partial \dot{\xi}_i} = 0 \quad . \tag{2.20}$$

The boundary conditions are

$$\frac{\partial L}{\partial\left(\frac{\partial \xi_i}{\partial x_j}\right)} = 0 \quad . \tag{2.21}$$

The ξ_i represent the two variables describing the magnetic configuration, θ and ϕ, while the x_j represent the three spatial coordinates. Solutions to the equations of motion can be found once explicit forms of L and F are given.

Specific expressions for the Lagrangian and dissipation functions are made in terms of the polar and azimuthal angles of the magnetization. The particular expressions chosen for L and F must be such that the resulting equation of motion (Eq. (2.20)) must be consistent with the LLG equation. One convenient choice for the kinetic energy that fulfills this requirement is

$$w_k = \frac{M}{|\gamma|}\dot{\theta}\phi\sin\theta \quad . \tag{2.22}$$

The potential energy is the same as for the static case, namely

$$w_p = A(\nabla\theta^2 + \sin^2\theta\nabla\phi^2) + K\sin^2\theta + 2\pi M^2\sin^2\theta\sin^2\phi$$
$$-H_x\sin\theta\cos\phi - H_y\sin\theta\sin\phi - H_z\cos\theta \quad , \tag{2.23}$$

where H_z is the magnitude of the drive field, which is oriented perpendicular to the film. Finally, the form of the dissipation function that is consistent with the LLG equation is

$$F = \frac{\alpha M}{2\gamma} (\dot{\theta}^2 + \sin^2\theta \, \dot{\phi}^2) \quad . \tag{2.24}$$

With these expressions, the mathematical model is complete.

Integration of L and F through the domain wall, using the Bloch wall dependence of $\theta(y)$, produces a simpler and therefore more usable form for these quantities. In the integration, ϕ is constant. The final result for the new Lagrangian and dissipation functions are

$$L' = \int_{-\infty}^{+\infty} L \, dy = -4\sqrt{AK} + \frac{2M}{\gamma} \dot{\phi} q + 2MH_z q - 4\pi M^2 \sin^2\phi + \pi H_x M \cos\phi + \pi H_y M \sin\phi \tag{2.25}$$

and

$$F' = \int_{-\infty}^{+\infty} F \, dy = \frac{\alpha \Delta M}{\gamma} \{(\frac{\dot{q}}{\Delta})^2 + \dot{\phi}^2\} \quad , \tag{2.26}$$

where q is the wall position as measured from any convenient reference point. Using q and ϕ as the dependent coordinates, the equations of motion specifically become[7,8]

$$\dot{q} = 2\pi M \Delta \gamma \sin 2\phi - \frac{2A\gamma}{M} \frac{d^2\phi}{dz^2} + \frac{\pi \Delta \gamma}{2} (H_y \sin\phi - H_x \cos\phi) + \alpha \Delta \dot{\phi} \tag{2.27}$$

and

$$\dot{\phi} = \gamma H_z - \frac{\alpha}{\Delta} \dot{q} \quad . \tag{2.28}$$

The boundary conditions at the film surfaces are $\frac{d\phi}{dz} = 0$ if there are no surface anisotropies. From these equations, it can be seen that the wall velocity is closely linked to the configuration of the azimuthal

angle ϕ in the domain wall. These coupled equations of motion describe the dynamics of a wall in which ϕ is allowed to vary in the z direction, along the wall surface.

An important application of the equations of motion is to steady-state motion. Steady-state motion is defined as that type of wall motion having the following two characteristics: a constant wall velocity and an internal structure that does not change with time ($\dot{\phi} = 0$ everywhere along the wall). If steady-state motion occurs, then it has certain velocity characteristics, as specified by the equations of motion. Equation (2.28) reduces to

$$\dot{q} = \left(\frac{\Delta\gamma}{\alpha}\right) H_z \quad , \qquad (2.29)$$

where the constant term $\frac{\Delta\gamma}{\alpha}$ is called the mobility. Thus, the steady-state wall velocity is proportional to the drive field H_z. This relation holds only if the other equation of motion, Eq. (2.27), can also be satisfied simultaneously. In other words, steady-state motion with a linear mobility occurs only if there exists a wall structure compatible with such a motion.

The linear mobility does not extend to arbitrarily high values of the drive field. This can be seen by considering the torques that produce wall motion. Equation (2.27) can be rewritten as

$$\dot{q} = \left(\frac{\gamma}{2M}\right) \frac{\delta\sigma}{\delta\phi} \quad , \qquad (2.30)$$

where σ is the wall energy per unit area, defined as $\sigma = \int w\, dy$. The term $\frac{\delta\sigma}{\delta\phi}$ represents the torque along the z direction on the spins in the

wall. According to the LLG equation, this torque causes a time rate of change in the polar angle θ, which in turn implies a changing wall position. Thus the torque $\frac{\delta\sigma}{\delta\phi}$ is directly responsible for wall motion. It is the torques from the internal demagnetizing field and the applied in-plane field, not the drive field, which contributes to $\frac{\delta\sigma}{\delta\phi}$. Thus an upper limiting velocity exists because these torques are limited by the magnitude of M, H_x, and H_y. The limiting velocity is a result of internal constraints, not external drive conditions.

The simultaneous equations of motion can be solved analytically for walls of infinite extent, that is, if the structure is one-dimensional. In this case, there is no surface stray field and therefore ϕ is constant in z. If the effects of a uniform in-plane field are included, then the equations of motion are

$$\dot{q} = 2\pi M\Delta\gamma \sin 2\phi + \frac{\pi\Delta\gamma}{2}(H_x \sin\phi - H_y \cos\phi) \qquad (2.31)$$

and

$$\dot{q} = \frac{\Delta\gamma}{\alpha} H_z \quad . \qquad (2.32)$$

As is evident from Eq. (2.31), for every velocity there is an associated value for the azimuthal angle of the internal wall structure. Because of the particular functional dependence of the velocity on ϕ, there is clearly an upper limit to the velocity. In the absence of an in-plane field, this peak value is [12,13]

$$v_p = 2\pi M\Delta\gamma \quad . \qquad (2.33)$$

This is called the Walker critical velocity. For nonzero in-plane

fields, the peak velocity is larger than the Walker velocity. The peak velocity increases steadily with increasing in-plane field. Steady-state motion above the peak velocity is inconsistent with the equations of motion. For every peak velocity is an associated drive field H_c, called the critical or breakdown field, as given by Eq. (2.32). Thus, one-dimensional wall structures exhibit a linear mobility region of velocity for drive fields less than the breakdown field.

In films of finite thickness, determination of the limiting velocity is complicated by the presence of the nonuniform stray field. In the one-dimensional case, it was seen that the peak velocity depends on the magnitude of the in-plane field. In a thin film, the in-plane stray field varies along the wall. Thus, it is not immediately clear what will be the peak velocity in a thin film. An additional complication is the torque produced by the exchange term that must now be considered. Therefore, solutions of the differential equations of motion, Eqs. (2.27) and (2.28), now have to be produced using numerical techniques[6]. The approach is similar to that used when solving for the static wall structure. In the dynamic case, there is an additional term in the equation that depends on wall velocity. In this case, the peak velocity is found by repeatedly solving for the wall structure for increasing values of the velocity. For velocities greater than a certain peak velocity, solutions to the equations of motion do not exist.

The peak velocity of walls in thin films is significantly lower than that of one-dimensional walls. For example, the peak velocity in the absence of an in-plane field for a typical film (P197) is $0.19v_w$, where

v_w is the Walker critical velocity. The steady-state wall structure at the peak velocity is shown by the solid line in Fig. (2.7). The dotted line shows the static equilibrium configuration for reference. It can be seen that, at the peak velocity, the spins have rotated by varying amounts from their static orientations, depending on position through the thickness. Near the top film surface, a bulge in the dynamic wall structure is seen, which will ultimately be identified as the formation of a horizontal Bloch line.

The reduced peak velocity in thin films can be understood by considering the detailed effects of wall structure. For a given point in the wall, the velocity depends mostly on the local value of ϕ and on the magnitude of the in-plane field, via Eq. (2.27). Qualitatively, one can consider that the velocity at a given point in the wall is given by the formula for the one-dimensional case, Eq. (2.31), using the local value of ϕ. The dependence of the wall velocity on ϕ is shown in Fig. (2.8), for two different in-plane field values. In (a), the in-plane field is zero. It can be seen that the wall velocity has a sinusoidal dependence on ϕ and that there are four zero-velocity orientations of ϕ. The ones labelled A and B are positions of stable equilibrium, while the others are unstable equilibrium positions. Thus the value of ϕ for zero velocity can be either 0^o or 180^o. Each of these points has the same $v(\phi)$ behavior in its immediate neighborhood. The value of ϕ increases with increasing wall velocity. The maximum velocity is equal to the Walker velocity and occurs when ϕ reaches a value of 45^o or 225^o. Thus the peak velocity is the same regardless of whether the initial value of ϕ

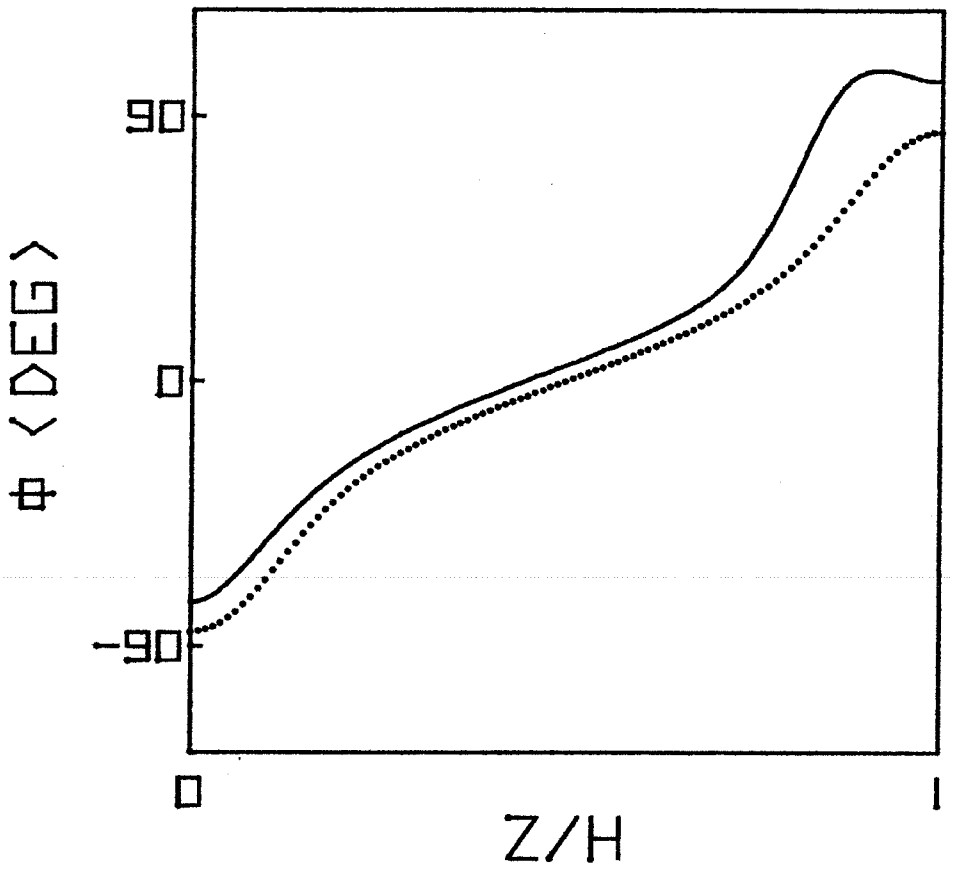

Fig. (2.7). The dynamic spin configuration at the peak steady-state wall velocity for zero in-plane field. The dotted line shows the static wall structure.

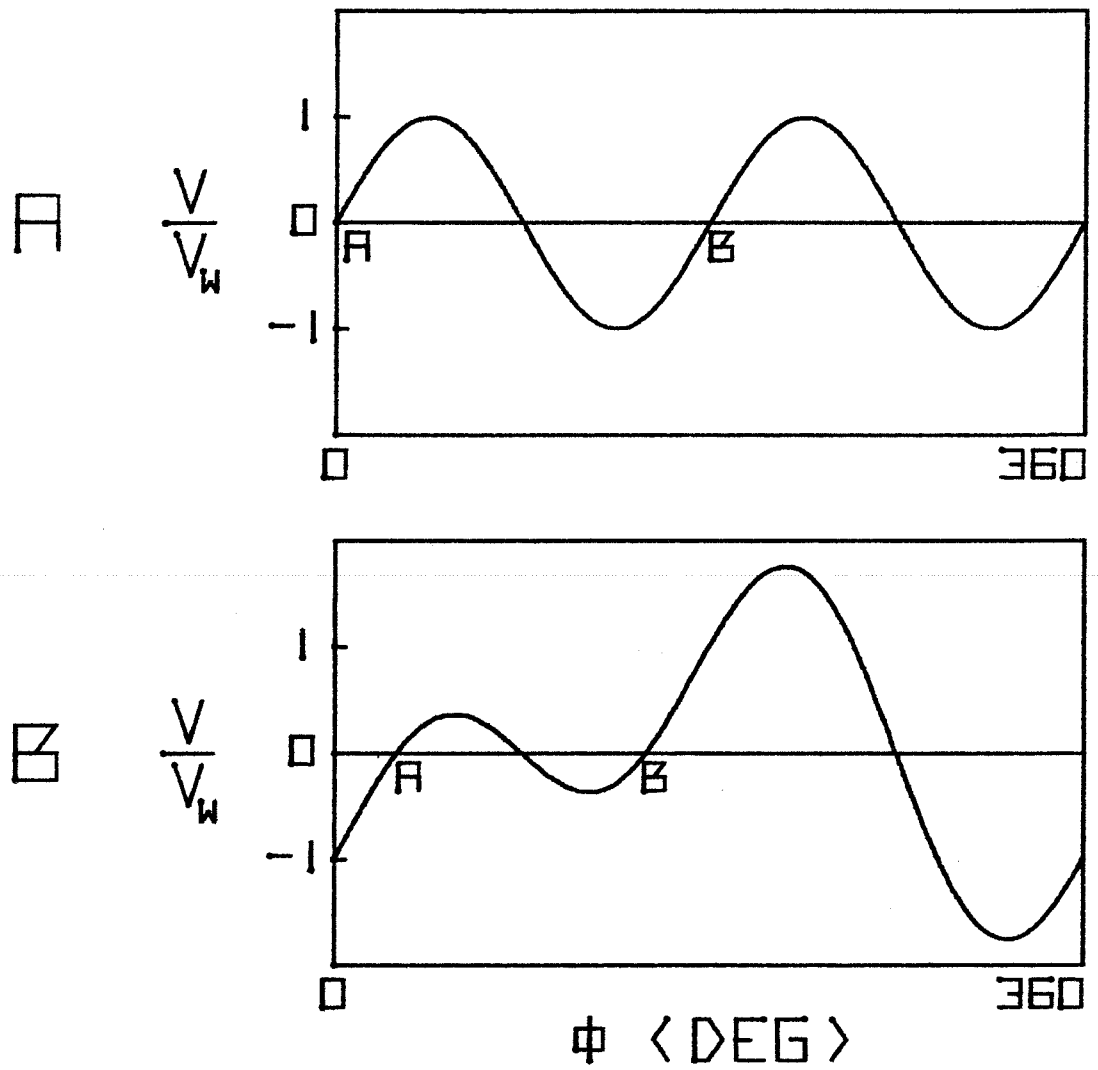

Fig. (2.8). The velocity vs. ϕ characteristic for (a) $H_y = 0$ and (b) $H_y = 4M$. The velocity is normalized to the Walker peak velocity.

was 0^{o} or 180^{o}. However, when an in-plane field is present, the symmetry between the two equilibrium points is broken. In (b), the $v(\phi)$ curve is shown for $H_y = 4M$ (typically 50 Oe). Starting from point B, as ϕ increases, the velocity increases to a value beyond the Walker critical velocity. For point A, however, the velocity peaks at a much lower value as ϕ increases. If the value of ϕ were constrained to remain in the neighborhood of point A, the peak velocity for the wall would be much smaller than the Walker critical velocity.

These results can be applied qualitatively to thin films. In these films, the static wall structure is nearly identical to that produced by the magnetostatic minimum. Thus, the static value of ϕ at the center of the film, where $H_s = 0$, is one of the two points A or B in Fig. (2.8a). At some point nearer the film surface, the stray field is equal to 4M, so the value of ϕ is that of point A or B in (b). The crucial point is that the spin distribution in the film is such that a part of it necessarily lies near the unfavorable point in (b), that is, the point with an associated low peak velocity. For steady-state motion to occur, all sections of the wall must move with the same velocity. The wall section near the unfavorable point consequently reduces the peak velocity of the entire domain wall. Thus, walls in thin films have lower peak velocities than do one-dimensional walls.

A uniform in-plane field applied to the domain wall affects the peak velocity. For example, the calculated peak velocity for an in-plane field applied perpendicular to the wall is shown in Fig. (2.9). The velocity is plotted as a function of in-plane field. For $H_y = 0$, the

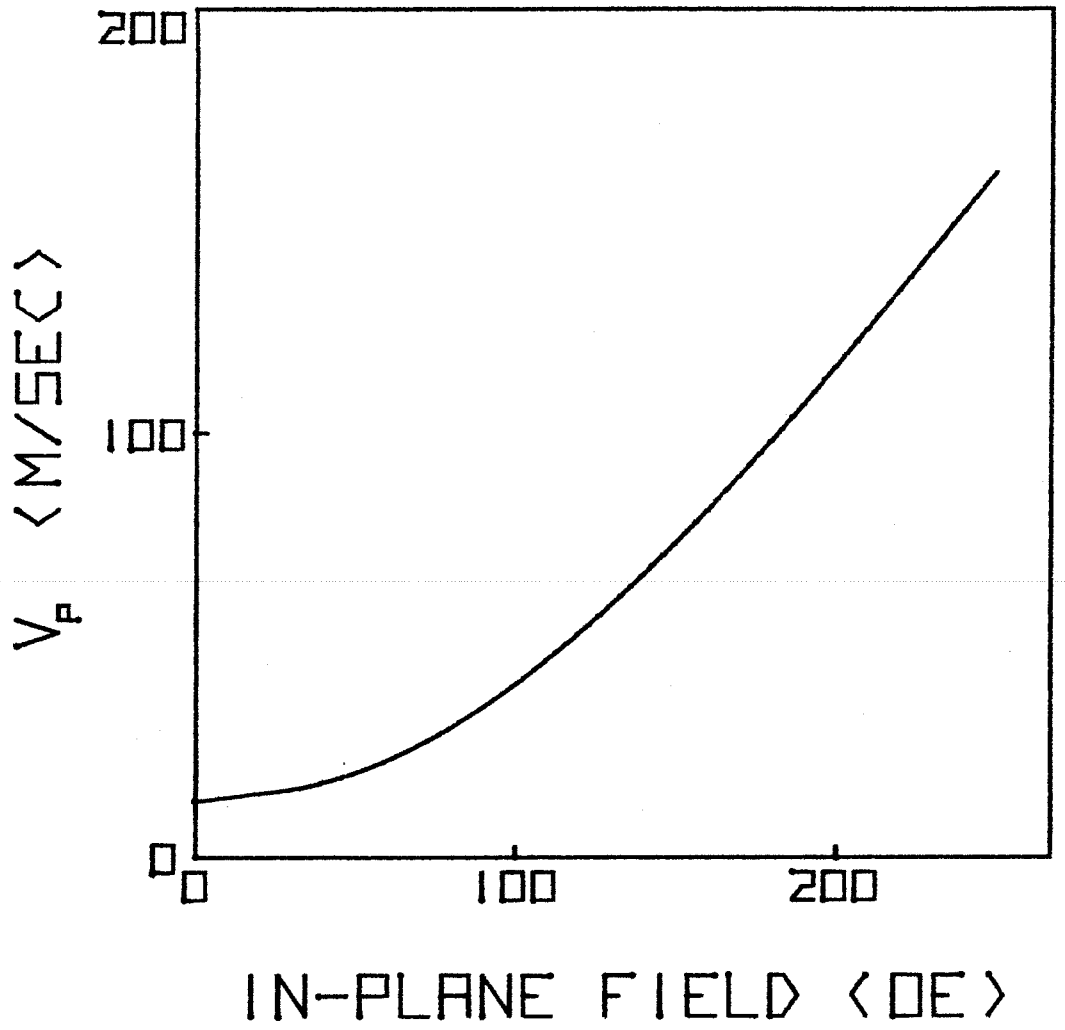

Fig. (2.9). Peak velocity as a function of in-plane field magnitude. The field is applied perpendicular to the wall.

peak velocity is 13 m/sec, much less than the 71 m/sec Walker critical velocity. Although the peak velocity increases somewhat up to 100 Oe, the bulk of the increase occurs for higher in-plane fields. Peak velocities far in excess of the Walker velocity can be obtained. It is clear that the application of an in-plane field significantly increases the peak velocity.

Steady-state motion is impossible for drive fields greater than the breakdown field. For the simple one-dimensional case, the exact behavior of q and ϕ can be obtained by the use of the equations of motion (2.27) and (2.28), without the exchange term. Above breakdown, the spins precess continually at a rate which depends on the instantaneous velocity, which in turn depends on the value of ϕ. Thus the velocity itself is continually changing, even becoming negative for certain ranges of ϕ. The time-averaged velocity is always less than the peak velocity.

In thin films, spin precession also occurs after breakdown, although in a fashion that is nonuniform through the film thickness. A qualitative description of this process[8,14,15] is shown in Fig. (2.10), in which the instantaneous wall configuration is shown for various times after the start of a drive pulse. The azimuthal angle for individual spins in the wall is plotted as a function of position through the normalized film thickness. Initially, the configuration is all of one chirality, as shown in (a). When the pulse field is applied (b), breakdown begins first at a point near one film surface. Here, the spins begin to precess and jump to the next chirality, forming a horizontal Bloch line that bridges the two chiralities. As the pulse continues, (c), more spins jump to the next chirality, or

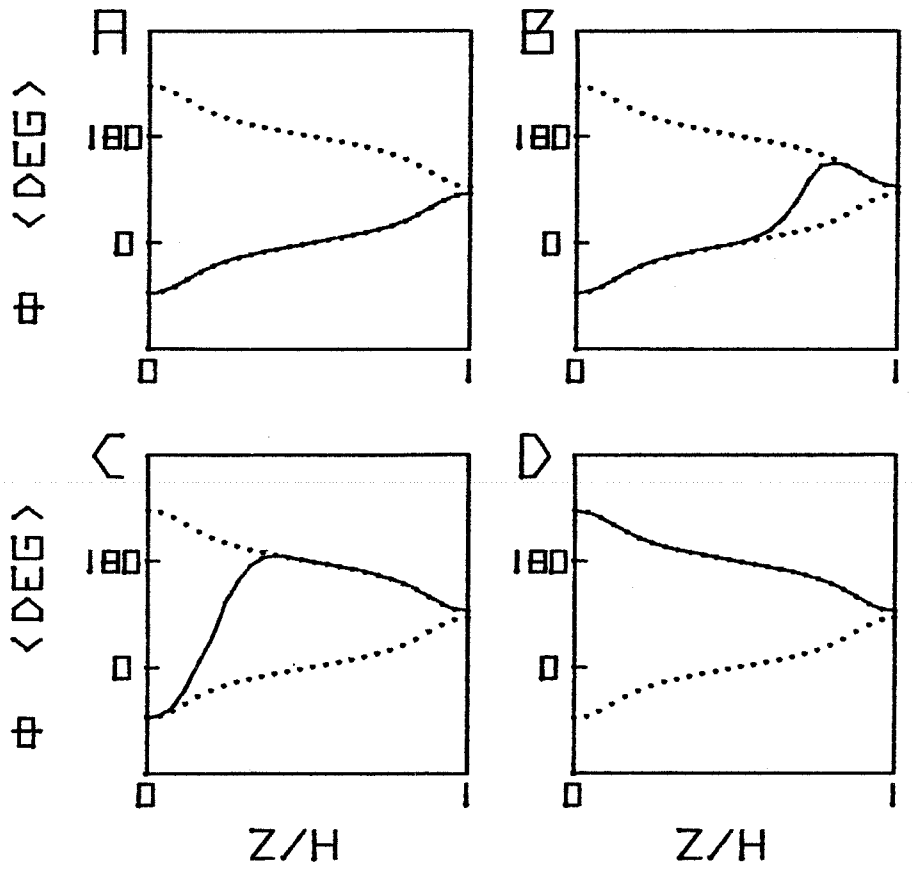

Fig. (2.10). The time evolution of the spin configuration during a pulse, showing qualitatively the nucleation, propagation and punch-through of a horizontal Bloch line.

equivalently, the HBL moves down through the film thickness. When the HBL meets a free surface, (d), it disappears and the wall has a chirality that is opposite from that with which it started. As the pulse continues, the process begins again, with the HBL nucleating at the bottom film surface. The process in which an HBL meets a surface and disappears is called punch-through. At any particular time during the pulse, most of the spins lie reasonably close to one of the two chiralities. Thus, spin precession above breakdown in thin films occurs via the formation and propagation of an HBL.

During wall motion that involves HBL's, the wall velocity is nearly independent of drive field. Calculations can be made to predict the so-called saturation velocity. An approximate analytical model[8] gives a time-averaged velocity as

$$v_0 = \frac{7.1 A\gamma}{h\sqrt{K}} \quad . \qquad (2.34)$$

This result is independent of drive field because, in the model, the instantaneous velocity depends only on the position of the HBL in the film. This property is supported by the results of numerical calculations[15]. Thus, wall motion with HBL's has a constant low velocity with a continual precession of ϕ.

2.3 Summary

Domain walls in thin films have a Bloch wall structure with a variable azimuthal angle. The wall structure is characterized by the value of the azimuthal angle as a function of position through the film

thickness. The existence of the surface stray field causes a static twist in the wall structure. In-plane fields affect the wall twist. The dynamic behavior of domain walls shows a linear mobility at low drives. Above a certain critical field, the velocity remains constant as HBL's form and propagate through the film thickness.

References

1. W. F. Brown, Micromagnetics, (Interscience, New York, 1963).
2. S. Chikazumi, Physics of Magnetism, (John Wiley and Sons, New York, 1964).
3. A. R. Forsyth, Calculus of Variations, (Dover, New York, 1927).
4. L. Landau and E. Lifshitz, Physic. A. Sowjetunion 8, 153 (1935).
5. E. Schlomann, J. Appl. Phys. 45, 369 (1974).
6. A. Hubert, J. Appl. Phys. 46, 2276 (1975).
7. J. C. Slonczewski, Intern. J. Magnetism 2, 85 (1972).
8. J. C. Slonczewski, J. Appl. Phys. 44, 1759 (1973).
9. T. L. Gilbert, Phys, Rev. 100, 1243 (1955).
10. J. A. Cape and W. F. Hall, Phys. Rev. Lett. 30, 801 (1973).
11. J. A. Cape and W. F. Hall, J. Appl. Phys. 45, 3572 (1974).
12. J. F. Dillon, Magnetism, ed. Rado and Suhl (Academic Press, New York, 1963).
13. N. L. Schryer and L. R. Walker, J. Appl. Phys. 45, 5406 (1974).
14. B. E. Argyle, J. C. Slonczewski, and A. F. Mayadas, AIP Conf. Proc. 5, 175 (1971).
15. B. E. MacNeal and F. B. Humphrey, IEEE Trans. MAG-15, 1272 (1979).

Chapter 3

Effects of Implantation on Bubble Wall Structure

3.1 Material characteristics of the implanted layer

Ion implantation is used to create a layer of different magnetic properties at the surface of the garnet film. In this procedure[1], the film is irradiated with a beam of 100 keV Ne^+ ions. Atoms in the film are displaced from their equilibrium positions in the lattice by collisions with the incoming ions. Because of these collisions, the ions penetrate the film to a distance of only 0.2 μm. The result is a thin damaged layer at the surface of the film.

Although the damage to the crystal structure favors an expansion of the lattice, the lattice cannot expand in a direction parallel to the film surface because of the presence of the bulk of the film. Thus the implanted layer is put into a state of lateral compression. Associated with this stress is a magnetoelastic energy which depends on the orientation of the stress and the orientation of the magnetization. This energy is a result of an interaction between the electron spin and the orbital motion of the electron. On a macroscopic level, the magnetoelastic energy can be written as[2]

$$E = -\frac{3}{2}\lambda\sigma\sin^2\theta \quad , \qquad (3.1)$$

where θ is the polar angle, σ is the stress (compressive stress has $\sigma > 0$), and λ is the magnetostriction constant. If the magnetostriction constant is negative, it can be seen from Eq. (3.1) that a compressive

stress favors an in-plane orientation of the magnetization.

The precise amount of magnetoelastic energy produced by implantation varies with position through the implanted layer because of the nonuniform distribution of the radiation damage. Investigations can be made to determine both the amount of damage to the lattice and the resulting strength of the stress-induced anisotropy[3,4]. A profile for the anisotropy in the implanted layer is shown in Fig. (3.1) for the following implantation conditions: 100 keV Ne^+ ions with a dosage of $2x10^7/cm^2$. These results were obtained through the study of the ferromagnetic resonance on successively etched films[4]. The effective anisotropy field resulting from the sum of the original growth-induced anisotropy and the stress-induced anisotropy is plotted as a function of depth into the film. In the bulk of the film, unaffected by implantation, the anisotropy is purely growth-induced and has a value of about 1310 Oe. In the 0.1 μm nearest to the film surface, the stress induces an anisotropy of about -2100 Oe, giving a total of about -800 Oe. There is a transition region, about 0.1 μm wide, near the bulk of the film in which the anisotropy changes smoothly from the bulk to the surface value.

3.2 Spin configuration in the implanted layer

The extent to which the magnetization in the implanted layer will lie in the plane of the film is affected by both the anisotropy profile and the exchange interaction. The differential equation governing the spin

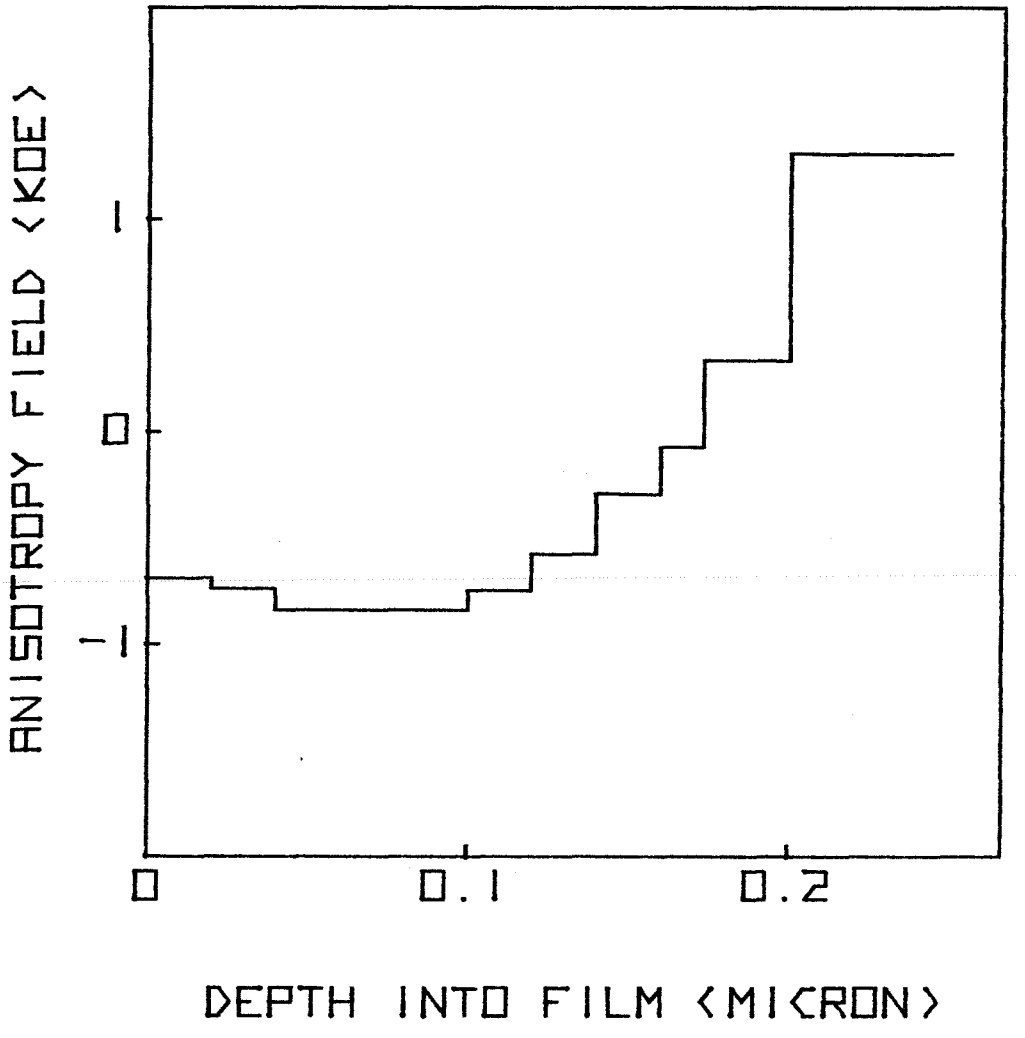

Fig. (3.1). The anisotropy field as a function of depth into the film.

orientation can be written as follows:

$$(K_u - 2\pi M^2) \sin 2\theta - 2A\frac{d^2\theta}{dz^2} = 0 \quad , \qquad (3.2)$$

where θ is the polar angle and z specifies the position through the film thickness. This equation describes the case for those locations far from the bubble wall. The equation can be solved numerically when $K_u(z)$ is given. The results are shown in Fig. (3.2) for a smooth approximation to the H_k distribution that was shown in Fig. (3.1). In (a), the polar angle of the spin distribution is plotted as a function of distance into the film. In (b), the H_k distribution is shown. It can be seen that there is a 0.1 μm region near the film surface in which the magnetization is essentially in-plane ($\theta = 90^o$). Between the bulk of the film and the in-plane layer is a 0.1 μm transition region in which the spins rotate by 90^o from the vertical to the horizontal. Films implanted under these conditions clearly have a layer of in-plane magnetization.

In the calculation of the spin structure in the implanted layer, the value of the azimuthal angle was unspecified. Neither the uniaxial anisotropy nor the exchange torque considered in that analysis has an effect on the value of ϕ. Instead, as in the Bloch wall case, the local value of the effective in-plane field determines the azimuthal orientation of the spins in the implanted layer. The effective field is composed of three terms: the external in-plane field, the stray field from nearby bubble domains, and the cubic anisotropy in garnet materials. Close to bubble domain walls, the stray field is the dominant factor

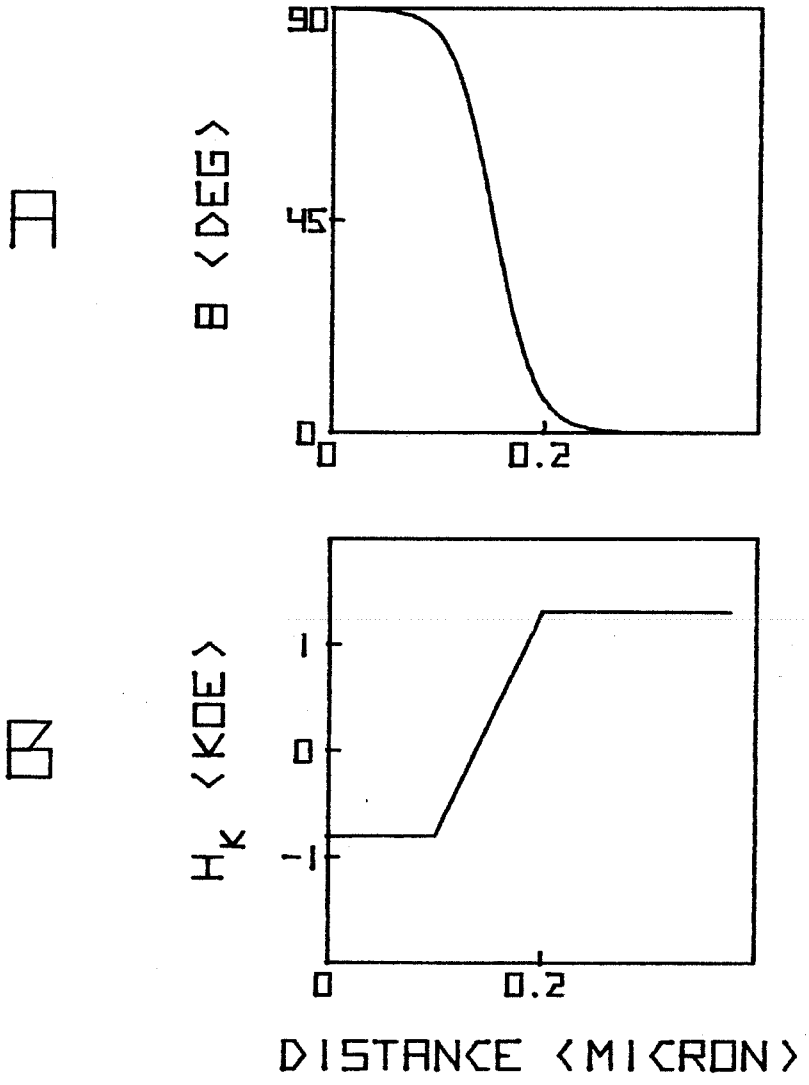

Fig. (3.2). (a) The polar angle of the magnetization is plotted as a function of distance into the film. The H_k distribution is shown in (b).

in determining the spin orientation. Further from the wall, where the stray field is smaller, the in-plane field and cubic anisotropy become the more significant terms. Thus the implanted layer has its own magnetic structure, given by $\phi(x,y)$, which depends on the magnitude and direction of external in-plane fields and the position of nearby bubble domain walls.

The magnetic structure of the implanted layer varies with in-plane field. There are two different structures, as shown in Fig. (3.3), each existing in a different range of in-plane field. In (a), the spin configuration is shown for an external in-plane field less than the peak bubble stray field. The azimuthal orientation of the spins in the implanted layer is shown by the arrows; the position of an underlying bubble domain is indicated by the dotted line. Near the bubble domain wall, the bubble stray field is the dominant field, orienting the spins radially outward from the bubble. However, at some point far from the bubble wall, the magnitude of the stray field becomes less than that of the external in-plane field. At these locations, then, the spins are directed along the external field. (The small cubic anisotropy is neglected in this discussion.) Near the bubble wall, there must exist a closure domain wall (solid line) in the implanted layer, where the spin orientation changes abruptly. This domain is located in the region where the bubble stray field is opposed to the external in-plane field. Inside the domain, the stray field is dominant; outside the domain, the external field is dominant. In (b), the spin configuration is shown for an external in-plane field much greater than the peak bubble stray

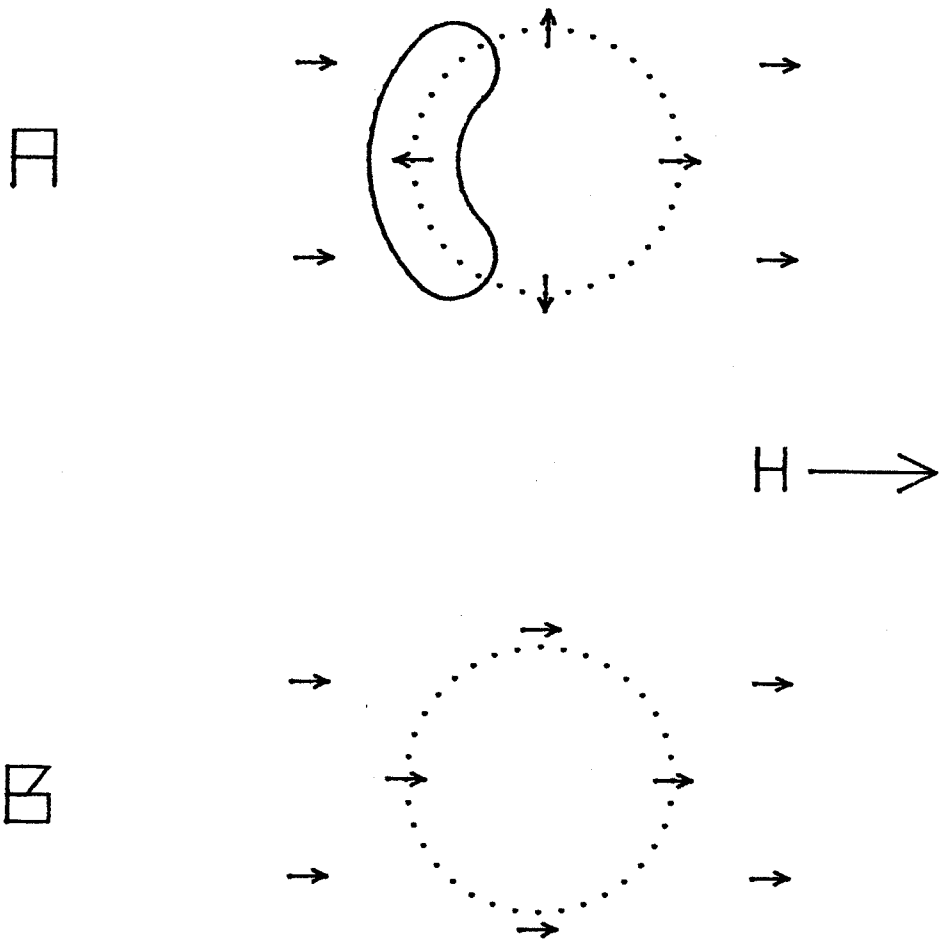

Fig. (3.3). Spin configuration in the implanted layer for an external in-plane field H much less than (a) and much greater than (b) the peak bubble stray field.

field. In this case, the implanted layer is saturated so there are no closure domains. The spins are then aligned with the external field.

The size of the closure domain, particularly its width, depends on the magnitude of the external field. For a given field, the side walls of the closure domain are positioned where the total in-plane field is zero. (Wall curvature effects are neglected.) The total field not only includes the external and the bubble stray fields, but also the demagnetizing field from the closure domain itself. The external field and the demagnetizing field oppose the bubble stray field. As the external field is increased, the two side walls of the closure domain move closer to the bubble domain wall. Thus the increase in external field is counterbalanced by an increase in the value of the bubble stray field at the location of the closure domain walls. Above a certain critical in-plane field, called the cap switch field, the closure domain is no longer stable. This point occurs when the sum of the external field and the demagnetizing field from the closure domain exceeds the peak value of the bubble stray field. Above the cap switch field, the implanted layer is saturated.

The cap switch field can be accurately predicted by considering the demagnetizing field of the closure domain, along with the external field[5]. This demagnetizing field reduces the cap switch field to a value that is considerably lower than the peak bubble stray field. In order to estimate the magnitude of the demagnetizing field, it is assumed that the side walls of the closure domain are sufficiently long and straight so that the wall energy plays a negligible role in determining the width of

the domain. This assumption is most valid for high external field, H_1, near the cap switch field. The form used for the demagnetizing field is then equal to that for two long, parallel charged walls:

$$H_d = \frac{Q_m}{2\pi}\left(\tan^{-1}\left(\frac{z}{x+a}\right) + \tan^{-1}\left(\frac{h_c-z}{x+a}\right) + \tan^{-1}\left(\frac{z}{a-x}\right) + \tan^{-1}\left(\frac{h_c-z}{a-x}\right)\right) \qquad (3.3)$$

where Q_m is the effective charge density of the wall, h_c is the thickness of the implanted layer, and 2a is the width of the closure domain. The coordinate system is shown in Fig. (3.4a). The origin of the coordinate system is located at the top of the bubble domain wall, at the interface between the bulk and the implanted layer. The side walls of the closure domain have an equilibrium position at that point where the total in-plane field, averaged over the thickness of the implanted layer, is equal to zero. Thus:

$$\int_{z=0}^{z=h_c} (\bar{H}_1 + \bar{H}_s + \bar{H}_d)\, dz = 0 \quad , \qquad (3.4)$$

where H_s is the stray field. The cap switch field is defined as the minimum H_1 for which Eq. (3.4) can no longer hold.

The calculation assigns a value for the width of the closure domain, 2a, for every value of the external in-plane field. This is shown in Fig. (3.4b). The numerical calculation was made using $4\pi M$ = 180 Oe and h_c = 0.15 μm. The bubble stray field that was used is that for a 5 μm bubble diameter in a 4.1 μm thick film. It can be seen that the width of the domain decreases with increasing in-plane field, from 1.8 μm at H_1 = 50 Oe to 0.15 μm at H_1 = 136 Oe. The calculated cap switch field of 136 Oe is close to the experimentally determined

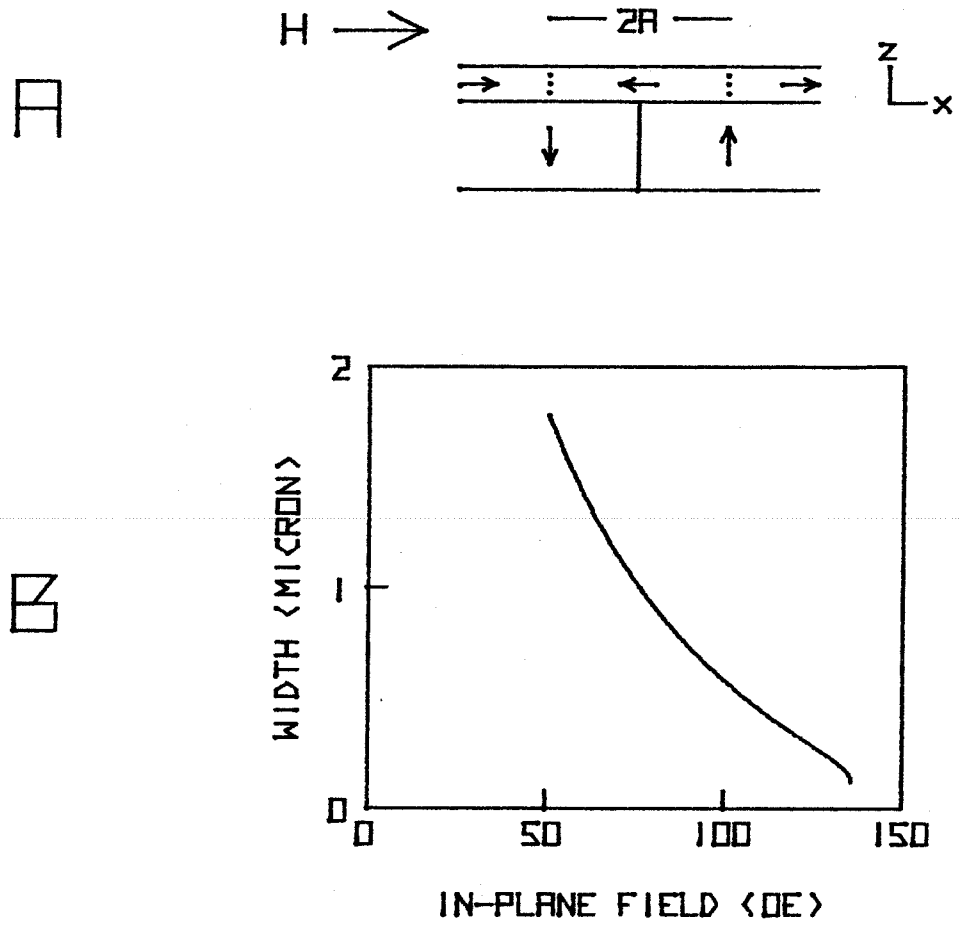

Fig. (3.4). (a) The orientation of spins in the implanted layer. (b) The width of the closure domain, 2a, as a function of external in-plane field magnitude.

value of 130 Oe for the film P206, whose material characteristics were used in the calculation.

3.3 Static bubble wall structure in implanted films

The presence of the implanted layer limits the possible wall structure that can exist in the bubble layer. Because of exchange, the azimuthal orientation of spins in the implanted layer must be equal to that of the spins at the top of the bubble domain wall. Thus, if a wall structure such as a VBL exists in a bubble, a corresponding twist in the implanted layer will also be necessary[6]. The compatibility of the spin configuration in the two layers can be judged quantatively by comparing their respective winding numbers[7]. The winding number S is defined as

$$S = \frac{1}{2\pi} \oint \frac{d\phi}{ds} ds \quad . \qquad (3.5)$$

The contour integral is taken over a counterclockwise circuit of the bubble perimeter, and measures the total rotation of the azimuthal orientation of the spins. The parameter S thus measures the general topological properties of the spin configuration and does not depend on such details as the location of twists in the structure. Similarly, an S number for the spin structure in the implanted layer can be defined by measuring ϕ in the implanted layer at the perimeter of the underlying bubble. The winding number in the implanted layer should be the same as that for the bubble for the two to be compatible.

Some examples of bubbles with different winding numbers are given in Fig. (3.5). In (a), the spin configuration at the center of an S = 1 bubble wall is shown. It contains two VBL's of opposite winding sense. Because the direction of the magnetization makes exactly one complete revolution during a circuit of the bubble circumference, the winding number is equal to 1, as specified by Eq. (3.5). In (b), another bubble wall structure containing two VBL's is shown. Here the winding sense of the two VBL's is identical, and opposite to that in the rest of the bubble wall. Consequently, the direction of the magnetization does not rotate over one circuit of the bubble circumference, so that S=0.

The bubble winding number can be experimentally identified using bubble translation[8]. In this experiment, a bubble is propagated across the film using a bias field gradient. Bubbles with winding numbers different from zero translate at angles to the direction of the gradient. Each winding number is associated with a specific angle. Observation of the translation angle thus allows the bubble S number to be determined. In implanted films, detailed observations[9,10] show that only S=0 and S=1 bubbles exist. (States with Bloch points[6,9], namely the S=½ states, will not be discussed.) This reflects the particular structure of the implanted layer. As shown in Fig. (3.3), there are two different structures. One that occurs for low in-plane fields has the characteristic that along the perimeter of the underlying bubble, the magnetization is directed radially outward from the bubble. For one circuit of the bubble circumference, then, the magnetization makes exactly one revolution.

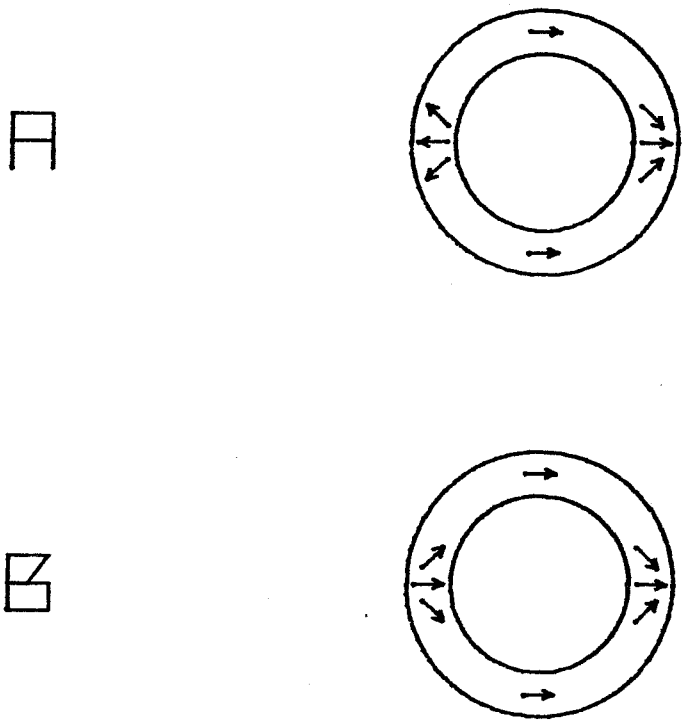

Fig. (3.5). The internal wall structure of (a) an S=1 bubble and (b) an S=0 bubble.

This structure has an S=1 winding number and is therefore associated with the S=1 bubble wall structures. For high in-plane fields, the implanted layer is saturated. The magnetization thus makes no revolution in one circuit of the bubble circumference, so S=0. This structure is associated with an S=0 bubble wall structure. Only S=0 and S=1 bubbles can therefore be expected to occur in implanted films.

The implanted layer suppresses hard bubbles, i.e., those bubble states with many VBL's. The extent to which hard bubbles exist in a film can be quantified by measuring static magnetic properties of a large number of bubbles. Hard bubbles have a higher collapse field than do normal bubbles. The collapse field is defined as that value of the perpendicular bias field above which bubble domains do not exist. It depends on the value of the magnetization, the film thickness, and the surface energy of the bubble domain wall (see Appendix A). When a bubble wall is filled with VBL's, the wall energy is noticeably increased, and the collapse field of the bubble becomes higher. Thus a hard bubble can be distinguished from a normal bubble by its collapse field. The extent to which bubble walls can support a large number of VBL's is gauged by the range of collapse fields for bubbles in a film. A large selection of bubbles will contain both normal and hard bubbles, if they exist. Fig. (3.6) shows the range of collapse fields (ΔH) for bubbles in a series of etched implanted films. A small layer of variable thickness was etched from the surface of each film. It can be seen that, for unetched implanted films, ΔH is nearly zero, implying that there are no hard bubbles. This is also true for etching depths up to 0.15 μm. When more

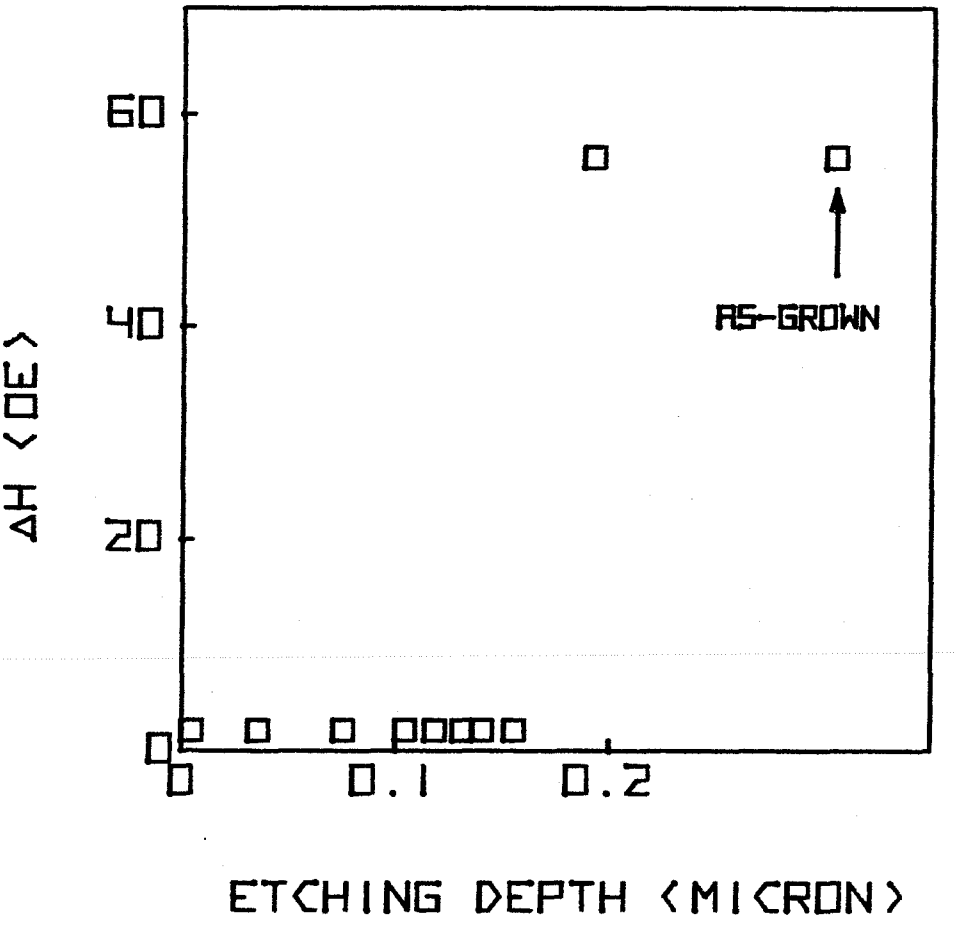

Fig. (3.6). The spread in collapse fields for bubbles in a series of etched films is plotted as a function of etching depth.

than that amount is etched from the film, hard bubbles begin to appear, giving a characteristic ΔH of about 55 Oe, the same as that for the as-grown film. The experimental measurement of 0.15 μm for the thickness of the implanted layer agrees with the results shown in Figs. (3.1) and (3.2). Only a thin in-plane layer is required to suppress those bubble wall structures that are incompatible with the structure of the implanted layer.

In summary, ion implantation in garnet films produces an in-plane magnetic layer. The magnetization in the layer is oriented mostly by the bubble stray field and the applied in-plane field. Because of the exchange interaction between the layer and the bulk of the film, bubble states in these films must have a structure compatible with that of the implanted layer. Consequently, only a few states exist in implanted films.

References

1. R. Wolfe and J. C. North, Bell Sys. Tech. J. 51, 1436 (1972).
2. S. Chikazumi, Physics of Magnetism, (John Wiley and Sons, New York, 1964).
3. V. Speriosu, H. Glass, and T. Kobayashi, Appl. Phys. Lett. 34, 539 (1979).
4. C. H. Wilts, J. Zebrowski, and K. Komenou, J. Appl. Phys. 50, 5878 (1979).
5. Y. Okabe, IEEE Trans. MAG-14, 602 (1978).
6. E. Feldkeller, Z. Angew. Phys. 19, 530 (1965).
7. J. C. Slonczewski, A. P. Malozemoff, and O. Voegeli, AIP Conf. Proc. 34, 138 (1978).
8. A. A. Thiele, Phys. Rev. Lett. 30, 230 (1973).
9. T. J. Beaulieu, B. R. Brown, B. A. Calhoun, T. Hsu, and A. P. Malozemoff, AIP Conf. Proc. 34, 997 (1979).
10. T. J. Gallagher, K. Ju, and F. B. Humphrey, J. Appl. Phys. 50, 997 (1979).

Chapter 4

Effects of Implantation on Bubble Dynamics

Ion implantation influences the dynamic behavior of the internal wall structure. Because the material properties of the film surface are changed after implantation, surface-related phenomena are different in as-grown and implanted films. In particular, the nucleation and punch-through of horizontal Bloch lines are affected by the implanted layer. Of the number of observable phenomena that are affected by HBL nucleation, the peak steady-state velocity is that which is the most dramatically changed by implantation. The peak velocity directly depends on the drive field at which HBL nucleation begins. The punch-through of HBL's is also affected by implantation. Since punch-through is an important process involved in the transitions between bubble states, the allowable state transitions are different in as-grown and implanted films.

4.1 Steady-state wall motion

The experimental study of steady-state motion requires the ability to produce wall motion under a constant effective drive for relatively long periods of time, e.g., a few hundred nsecs. The effective drive is composed of the applied bias field plus a contribution from the stray magnetic field from the domain configuration. Therefore, a domain configuration is needed that gives an unchanging contribution to the drive field during wall motion. Stripe domains have this characteristic. A stripe domain, shown in Fig. (4.1), exists when the magnitude of the bias

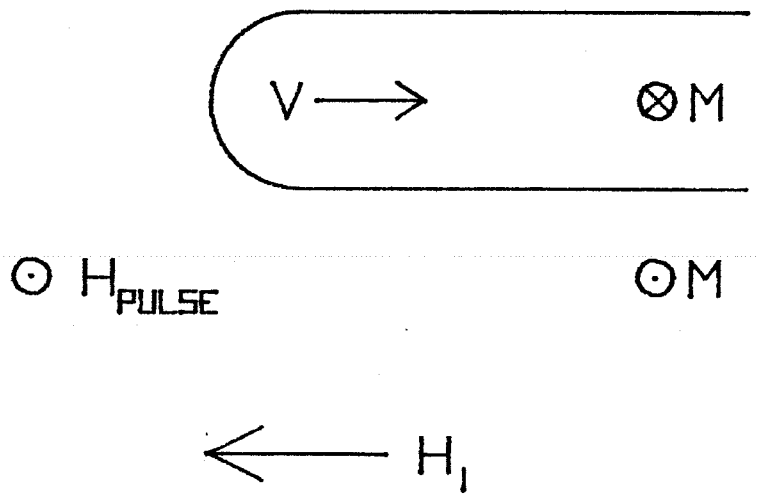

Fig. (4.1). The stripe domain configuration used for the peak velocity experiments.

field is too low for the existence of stable cylindrical domains (see Appendix A). Although stripe domains usually cover the film in a serpentine arrangement, the application of a uniform in-plane field causes them to have straight sides. At a certain critical bias field[1], the stripe is in a state of neutral equilibrium with respect to changes in its length. That is, there is no change in potential energy, including wall energy and magnetostatic energy, when the stripe head moves to expand or contract its length (see Appendix B). When a uniform bias field pulse is applied to the stripe, the stripe will change its length, and to a much smaller extent, its width. The velocity of the stripe head is controlled by the wall structure in the stripe head. By using this experimental arrangement, the steady-state motion of domain walls can be measured simply and accurately.

Measurements of instantaneous wall velocities are made with an optical sampling microscope[2]. A 10 nsec laser flash is used to illuminate the magnetic film; the short exposure time effectively stops the motion. The domains are observed with polarized light, utilizing the Faraday effect. Observations are made with a standard laboratory microscope and the images are recorded on video tape. The time history of the domain motion is determined by using a sampling system; that is, the domain motion is repetitively executed while the position of the laser flash in the cycle is slightly incremented during successive cycles (see Appendix C). This method allows instantaneous velocities to be measured.

Steady-state motion in as-grown films will be discussed first in order to illustrate the general behavior of stripe head motion. The

predictions of a theoretical model will be shown along with the experimental data. The breakdown processes in as-grown films will be discussed in order to give a background for the following discussion of peak stripe head velocity in implanted films.

4.1.1 Stripe head motion in as-grown films

In bubble films, the steady-state domain wall velocity is a nonlinear function of the drive field. Although the velocity is proportional to the drive for fields less than a certain threshold, the velocity above this critical field is relatively constant. This behavior is shown in Fig. (4.2), for a typical film (P197; Appendix F gives the material characteristics for the films). The graph shows an initial linear mobility of 5.4 m/sec/Oe while the breakdown velocity is 16 m/sec. Above the breakdown field of 4 Oe, the wall velocity is relatively constant. The numerical calculations described in Chapter 2 can be applied to the prediction of stripe head velocity by making certain assumptions. The first is that the breakdown of the wall structure at the tip of the stripe head controls the behavior of the stripe. The second is that, even though the wall structure varies around the stripe head, the exchange torques due to this variation are not large enough to significantly affect the breakdown process. In this case, the calculations for a planar wall can be applied to these particular experimental conditions. Numerical calculations of the spin distribution for this film at v=0 and $v=v_p$ appeared in Fig. (2.7). The calculations predict a linear mobility of 5.6 m/sec/Oe and a peak velocity of 13.3 m/sec, which is in agreement with the

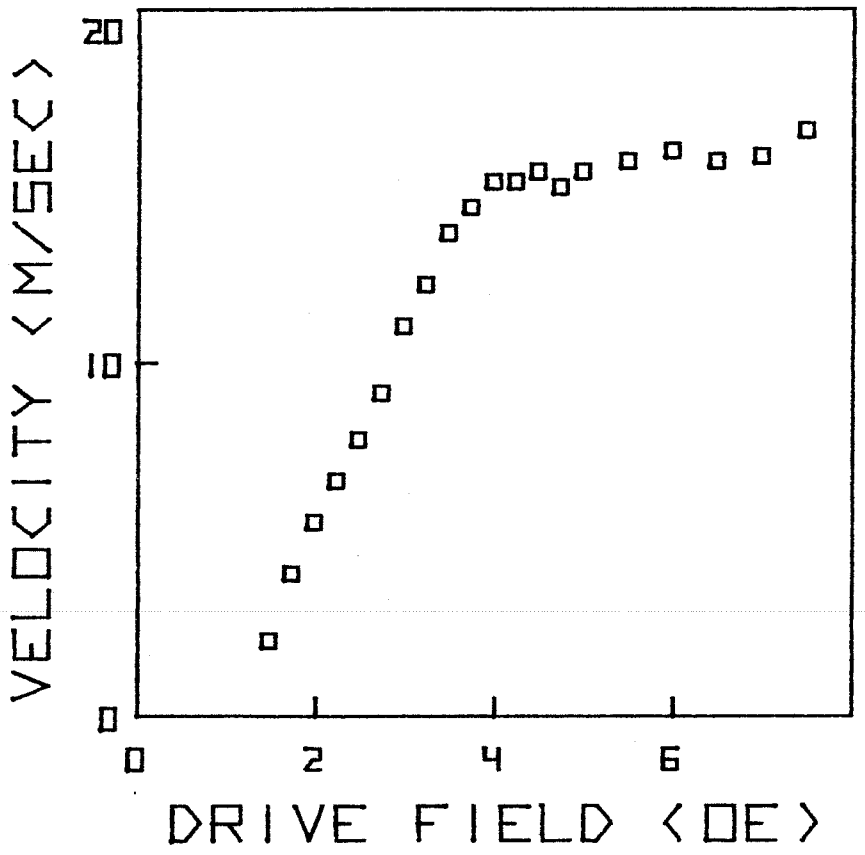

Fig. (4.2). Steady-state wall velcoity as a function of drive field.

data. This value of the breakdown velocity is significantly less than the Walker critical velocity of 71 m/sec for this film. The low peak velocity clearly identifies the breakdown process as that due to HBL nucleation.

The peak steady-state velocity changes significantly with in-plane field. When the field is applied parallel to the sides of the stripe domain, it is perpendicular to the wall section at the tip of the stripe head. As discussed in section 2.2, an in-plane field applied perpendicular to the wall restrains the spins in the wall from precessing away from their equilibrium orientations. Thus the wall configuration is stable for larger values of the velocity. The peak velocity is plotted in Fig. (4.3) as a function of in-plane field magnitude perpendicular to the wall for the film P197. It can be seen that the peak velocity varies from 16 m/sec to 160 m/sec for H_1=0 to H_1=250 Oe. The solid line is the theoretical prediction based on the model given earlier and shows good agreement with the data. The in-plane field has a small effect on the linear mobility. As discussed earlier, the torques from the exchange and anisotropy energies in the wall are much larger than that due to the in-plane field, so it is expected that the mobility does not change dramatically. The success of the predictions for the wall velocity supports the model for the breakdown of the wall structure.

When an in-plane field is applied perpendicular to the domain wall, HBL nucleation does not occur in the same way at the two film surfaces. The in-plane field adds to the stray field at one surface while it subtracts from the stray field at the other film surface. A typical

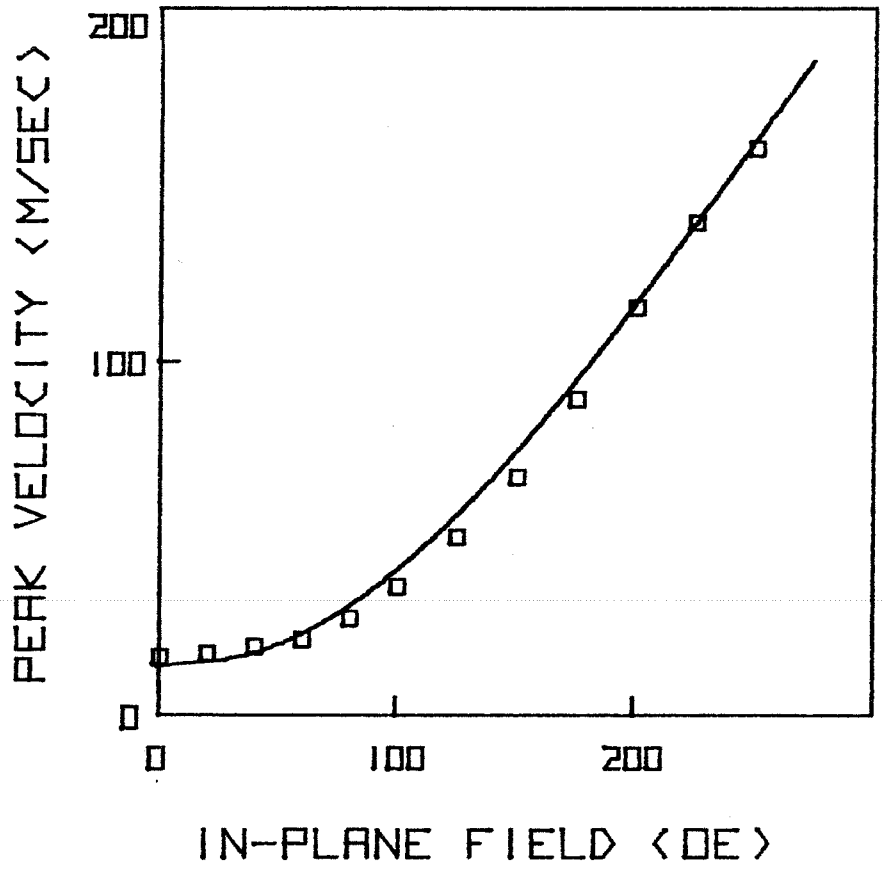

Fig. (4.3). Peak steady-state wall velocity as a function of in-plane field applied perpendicular to the wall.

example is shown in Fig. (2.6), for which the in-plane field is equal to $2\pi M$. At the top film surface, the spins are aligned with the stray field. On the other hand, at the bottom film surface, the spin orientation is rather far from the direction of the stray field there. Because the total in-plane field is higher at the top surface, HBL nucleation occurs there at lower wall velocities than at the lower surface. This asymmetry is independent of the wall chirality or the direction of the pulse field. If the original wall chirality is such that HBL nucleation occurs first at the top surface, the wall will change chirality only once. Then the wall will assume a steady-state configuration unless the pulse field is large enough to cause HBL nucleation at the bottom film surface. It is the surface with the highest breakdown that determines the peak velocity.

When the direction of the in-plane field is reversed, the wall structure also reverses so that the top film surface controls the peak velocity of the wall. Thus the in-plane field polarity can be used experimentally to select that particular film surface for which HBL nucleation determines the peak velocity. In as-grown films, the peak velocity is independent of the in-plane field polarity. This reflects the fact that there is no significant difference in the material characteristics near the film-air interface and the film-substrate interface. Differences should occur, however, in implanted films.

4.1.2 Steady-state motion in implanted films

An implanted layer raises the threshold for HBL nucleation. This produces a higher peak velocity when the in-plane field polarity is such that HBL nucleation takes place at the implanted layer. This effect is shown in Fig. (4.4) for the implanted film P206, nominally identical to the as-grown film P197. The velocity of the stripe head during contracting motion is plotted as a function of drive field. An in-plane field is applied parallel to the stripe, (a) along and (b) opposed to the direction of the stray field at the implanted surface. The in-plane field magnitude is 150 Oe. In (a), it can be seen that the velocity increases linearly with drive for pulse fields less than 11 Oe. Above this threshold, the velocity drops somewhat and remains relatively constant with increasing field. This threshold is the same as that for as-grown films. In (b), the direction of the in-plane field is opposite to that in (a). In this case, the linear region extends to an 18 Oe drive field, with a peak velocity of 120 m/sec. For any in-plane field, the wall motion exhibits a linear mobility and a peak velocity that depends on the polarity of the in-plane field[3,4].

The peak stripe head velocity is plotted in Fig. (4.5) as a function of in-plane field magnitude. The in-plane field is applied parallel to the stripe, along (□) or opposed (+) to the stray field of the stripe head at the implanted surface. It can be seen that the peak velocity increases smoothly with in-plane field magnitude. In the implanted sample, the peak velocity is always highest when the in-plane field is opposed to the stray field at the implanted surface. In this case the

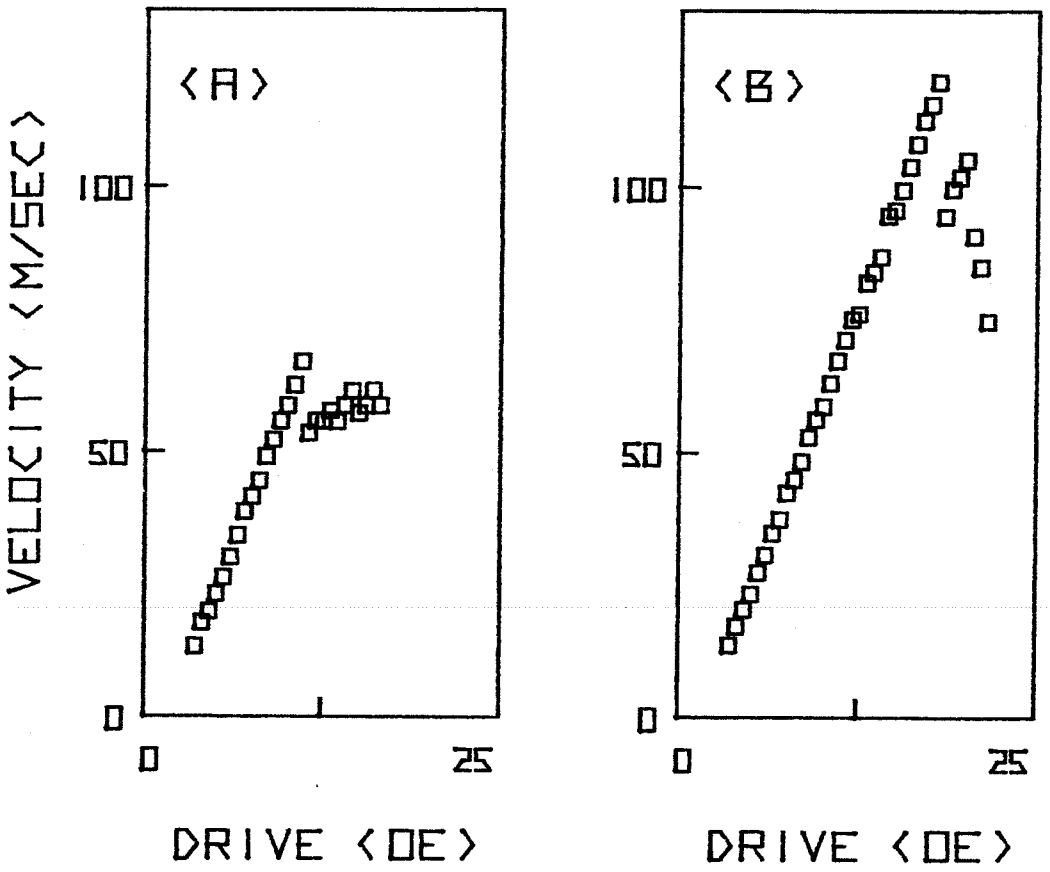

Fig. (4.4). Velocity as a function of drive field for a 150 Oe in-plane field applied (a) along or (b) opposed to the direction of the stray field at the implanted surface.

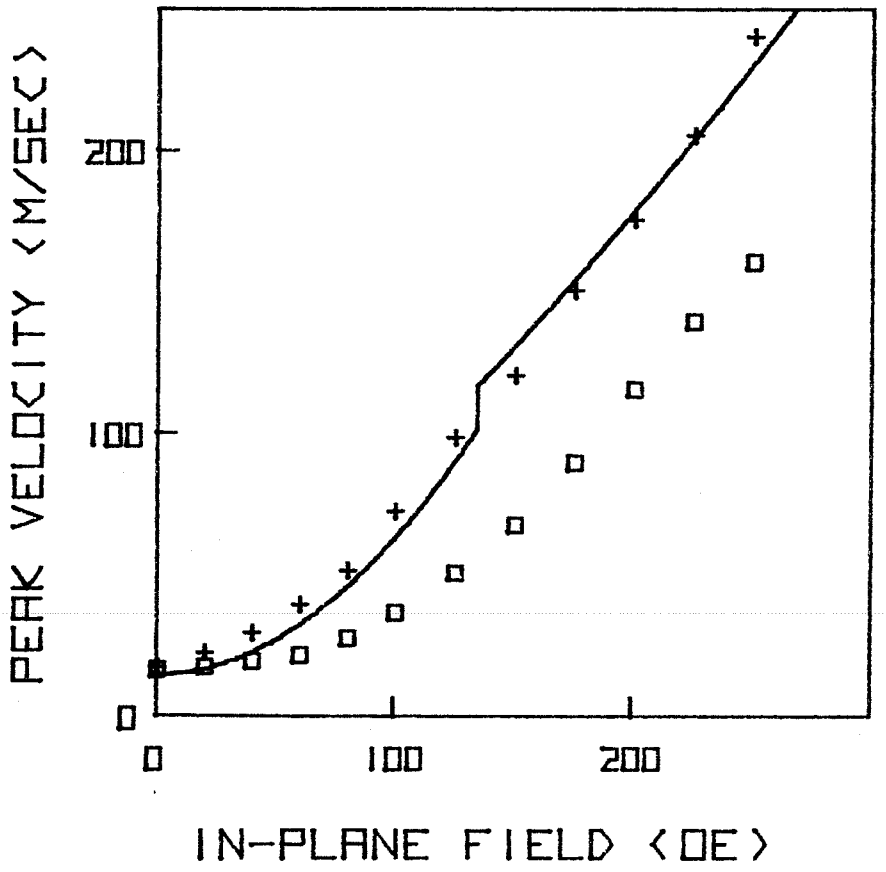

Fig. (4.5). Peak velocity as a function of in-plane field magnitude with an in-plane field direction (□) along or (+) opposed to the direction of the stray field at the implanted surface.

velocity increases from 15 to 280 m/sec when the in-plane field increases from 0 to 250 Oe. When the in-plane field direction is reversed, the peak velocity decreases by an amount which is up to 90 m/sec at 250 Oe. The velocity asymmetry does not occur in as-grown films, in which both in-plane field directions produce a peak velocity that is the same as the peak velocity of the implanted sample when the in-plane field is along the direction of the stray field at the implanted surface.

The velocity asymmetry exists because of the changed characteristics of HBL nucleation at the implanted surface. These changes become apparent under those circumstances in which the implanted surface controls the peak velocity of the domain wall, that is, when the in-plane field is applied opposite to the direction of the stray field at that surface. Implantation introduces two added complications. One is the demagnetizing field that is associated with the closure domain in the implanted layer. Since the magnitude of the total in-plane field at the wall strongly affects the wall velocity, a change in peak wall velocity can be expected. The other effect of implantation is a result of the exchange coupling between the implanted layer and the bulk of the film. It is assumed that the spins in the implanted layer act as a new boundary condition for the spin configuration in the bubble wall. These two effects can be incorporated into the numerical calculations to predict the wall velocity in implanted films.

For an external in-plane field less than the cap switch field, the closure domain exists in the implanted layer over the stripe head when the external field is opposed to the direction of the stray field at the

implanted layer. It is assumed that the width of the closure domain is the same during wall motion as it is statically. In this case, the calculation in Chapter 3 for the demagnetizing field due to the closure domain can be used without modification. In the numerical calculations for the peak velocity, a new form for the stray field is used, consisting of the stray field of the bubble plus the demagnetizing field from the closure domain. The total stray field is therefore less than the bubble stray field alone, causing an increase in peak velocity. This is expected because, as seen in Chapter 2, it is the stray field which produces a low peak velocity by destabilizing the wall structure. The other effect of the implanted layer, the surface pinning condition, does not alter the wall structure below the cap switch field because the surface spins are already aligned in the same direction as those in the implanted layer. The result of the numerical calculation for the predicted peak velocity is shown by the solid line in Fig. (4.5). The closure domain has an effect on the peak velocity for in-plane fields less than the cap switch field, H_1=136 Oe. The predicted wall velocity is quite close to the experimental values.

Above the cap switch field, a different effect is responsible for the increase in peak velocity. The implanted layer is saturated, so that all the spins are aligned with the external in-plane field, even when the in-plane field is opposed to the stray field. The increase in peak velocity is accounted for by assuming that the surface spin is fixed along the direction of the external in-plane field. In the numerical calculation for the spin configuration in the bubble wall, this simply

means that a new boundary condition replaces the previous one, in which $\frac{d\phi}{dz} = 0$ at the two film surfaces.

The calculated spin configuration with the new boundary condition is shown in Fig. (4.6) for the film P206. The azimuthal angle for individual spins in the wall is plotted as a function of normalized position through the film thickness. The implanted layer is at the top surface (z=h). Fig. (4.6a) shows the case for which a 150 Oe in-plane field is oriented in the positive y direction. The velocity is in the negative y direction. Both the static configuration and that corresponding to the peak velocity are shown. The top film surface has the pinning condition $\phi = 90^{o}$. At this surface, the in-plane field is along the direction of the stray field, so that the surface spin would normally be aligned close to the $\phi = 90^{o}$ direction, even without the pinning condition. At the bottom surface, the effectiveness of the stray field in aligning the surface spin near the $\phi = -90^{o}$ direction is reduced by the stray field. No solution exists for velocities greater than 76 m/sec. The HBL nucleates at the bottom surface. The results shown for a 150 Oe in-plane field are typical for in-plane field magnitudes up to 250 Oe.

The calculated spin configuration for a 150 Oe in-plane field in the opposite direction, i.e., in the negative y direction, is shown in Fig. (4.6b). Here the wall chirality opposite to that used in (a) is shown, because we are interested in HBL nucleation at the opposite film surface. The static configuration is labelled v=0. At the bottom (unpinned) surface, the in-plane field is along the stray field, thus aligning the surface spins to the $\phi = -90^{o}$ direction. At the top surface,

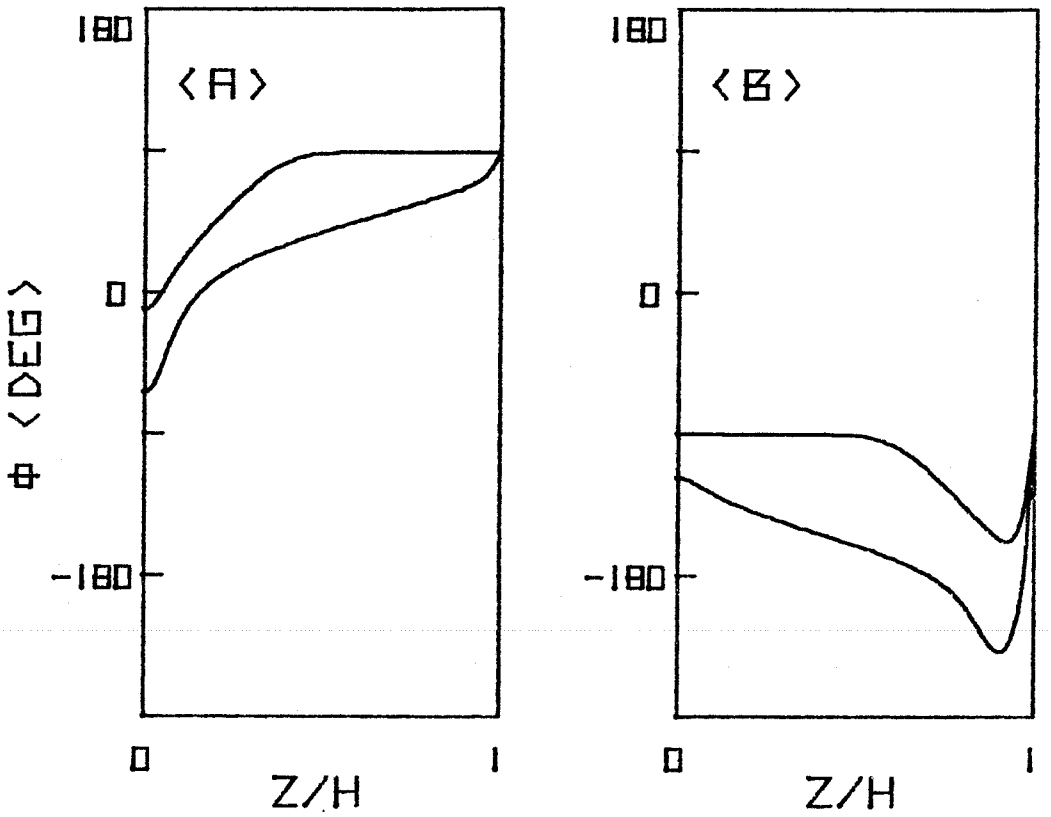

Fig. (4.6). The static (v=0) and dynamic ($v=v_p$) spin cinfiguration in the wall for a 150 Oe in-plane field applied along (a) and opposite (b) to the direction of the stray field at the implanted surface.

where the surface spin is pinned along the $\phi = -90^{o}$ direction, it can be seen that there is a sharp curve in the spin configuration. This occurs because the stray field favors an alignment of the spins just inside the surface toward the $\phi = 90^{o}$ direction. Also shown is the spin distribution corresponding to the 130 m/sec maximum velocity. At breakdown, the spin distribution is unstable near the top surface, instead of the bottom surface. The peak velocity is significantly higher than that for Fig. (4.6a). For in-plane fields up to 250 Oe, the peak velocity is always greatest when the in-plane field is applied opposite to the direction of the stray field at the implanted surface.

Modifications to the dynamic wall structure due to the implanted layer causes a suppression of HBL nucleation. The reason for this can be seen by examining the torques available to produce the wall velocity, as was done in Chapter 2. The velocity is directly proportional to the torque $\frac{\delta\sigma}{\delta\phi}$ from sources internal to the wall. Breakdown occurs when the torque cannot be increased at a particular location in the wall. The implanted layer suppresses breakdown because it introduces a localized twist in the spin structure that has an associated large exchange torque. The twist is located at the region of HBL nucleation. The exchange torque is proportional to $\frac{d^2\phi}{dz^2} = \phi''$. For the case given in Fig. (4.6), a positive ϕ'' contributes constructively to the wall velocity. In (a), the region of HBL nucleation is at the bottom (unpinned) film surface. There, the region of positive ϕ'' is very small and is located just at the film surface. On the other hand, in (b), where the nucleation occurs at the top (pinned) film surface, the region of positive ϕ'' is extensive.

The magnitude of ϕ'' is such that it allows an increase in peak wall velocity of nearly 50 m/sec.

The predicted peak wall velocity above the cap switch field is shown by the solid line in Fig. (4.5). It can be seen that there is a close agreement between theory and experiment, supporting the assumption of pinning at the implanted surface. There is also a discontinuity in the predicted velocity at the cap switch field, as the mechanism for the velocity increase changes. In reality, there are a number of factors which cause a more gradual transition. However, these have been left out of the calculation for reasons of simplicity. The essential features of the implanted layer, the demagnetizing field and the pinning condition, have been seen to account adequately for the velocity asymmetry.

4.2 Bubble state transitions

State changes represent the creation, annihilation or rearrangement of internal wall structures. To change a state into a different statically stable state, an HBL must move to a film surface and disappear. The simplest state change is one in which one of the unichiral states is transformed into the other. This occurs in process of HBL nucleation, propagation, and annihilation at a film surface as described in Chapter 2. Implantation changes the surface properties of the film. It can therefore be expected to affect HBL punch-through and, ultimately, bubble state transitions.

4.2.1 Unichiral state switching

Unichiral state identification can be made in a rapid and non-destructive manner using high speed photography. This method relies on the fact that segments of the bubble wall that contain added wall structure have very different dynamic properties than do wall sections without structure. Although each portion of the bubble wall is connected to other portions, to a significant extent the wall sections act independently of each other, resulting in a dynamic bubble distortion when the wall contains structure. Transient photography can detect these distortions. In particular, a non-destructive test can be made to distinguish the two unichiral states and the two states with a pair of VBL's. The test (see Appendix D) consists of applying a small (about 10 Oe) field in the plane of the film and then applying a small (about 2 Oe) bias pulse, causing the bubble to expand. Under these circumstances, each state has a unique dynamic shape.

The four states have different transient shapes during the pulse, as shown in Fig. (4.7). The static bubble position and shape is shown by the dotted line. During the test pulse, the unichiral states (shown in (a) and (b)) each have a relatively slow wall section that is parallel to the in-plane field. The position of this section is indicated by "P". By comparison, the other wall section that is parallel to the in-plane field moves very fast. The two unichiral states differ from each other because the slow wall sections are on opposite sides of the bubble. These wall sections have this behavior because an HBL structure is created by the in-plane field in the wall section whose center spin is opposed

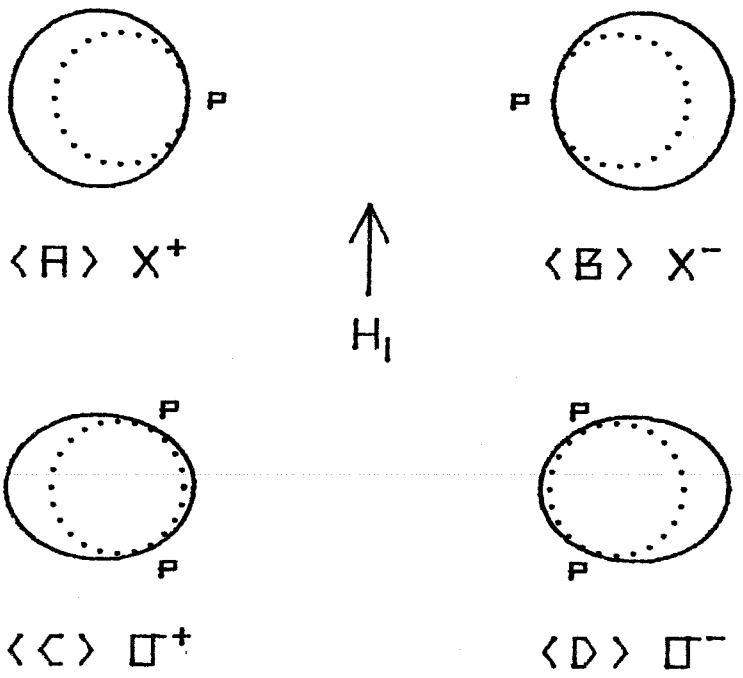

Fig. (4.7). The transient shape (solid line) of the four elementary bubble states during a test pulse with H_1 = 10 Oe. The dotted line shows the equilibrium bubble position.

to the in-plane field (see Appendix E). States with VBL's, such as the two states shown in (c) and (d), have different transient shapes. The sections containing the VBL's (indicated by "P") move slowly[6,7] while the rest of the bubble expands normally. The VBL's have equilibrium positions at opposite ends of the bubble as defined by the in-plane field. The two σ states can be distinguished from each other by the fact that, during wall motion, the VBL's deflect toward opposite sides of the bubble. Thus, with the use of high speed photography, the elementary bubble states can be easily distinguished.

In as-grown films, unichiral state switching is perfectly symmetric, i.e., the impulse required to switch the states is the same in both cases. If an expanding bias step is applied to a unichiral state in the film 2-16-44, the threshold for state conversion is 5.0 Oe. From the equations of motion, Eq. (2.27) and (2.28), it can be calculated that this step produces a change of $\overline{\phi}$ equal to 1.15π, close to the value of π that signifies that one chirality change has occured. Although the switching threshold is the same for the two states, the HBL is actually nucleated at different surfaces. This is shown in Fig. (4.8). For the χ^+ bubble state shown in (a), the initial spin configuration in the wall has an average orientation of -180^o. When a pulse is applied so that ϕ increases, the HBL will nucleate at the surface where the spin structure can bridge the gap between the chiralities in the easiest way, namely, near the bottom surface. The opposite situation holds for the χ^- bubble. If the two film surfaces have different magnetic properties, then an asymmetry would occur in the switching of the two states. In

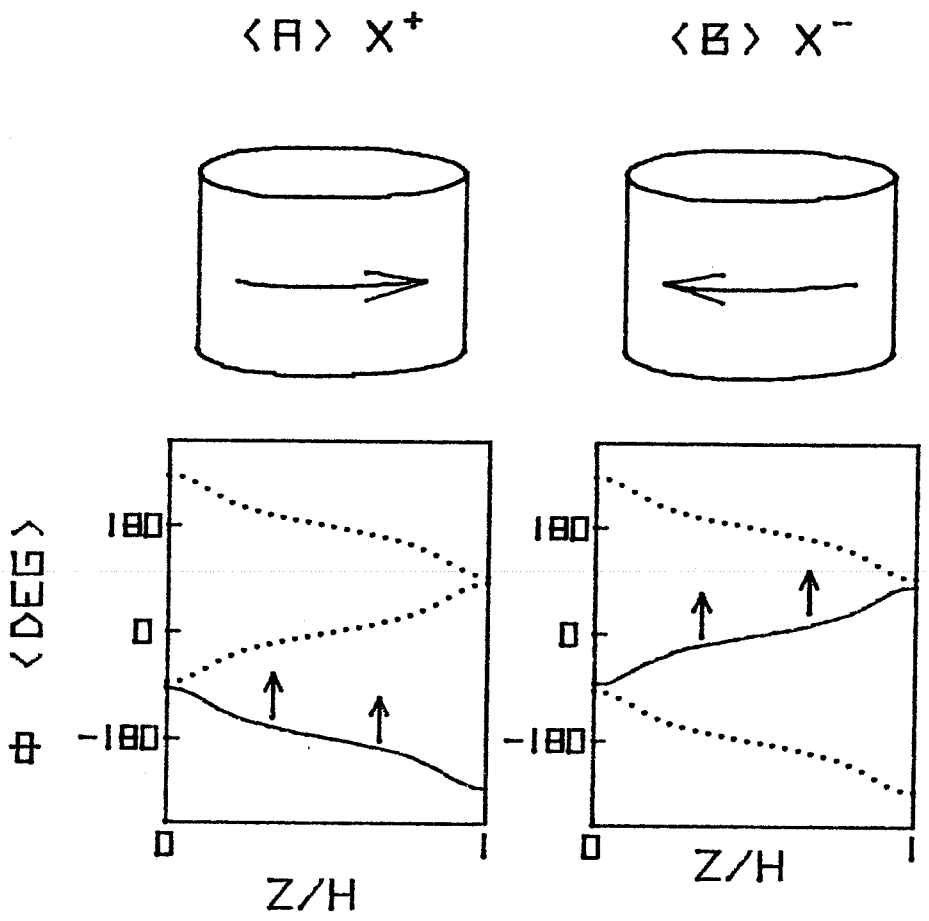

Fig. (4.8). The direction of spin precession in (a) a χ^+ and (b) a χ^- bubble state. The HBL nucleates at opposite film surfaces for the two cases.

as-grown films no asymmetry occurs. Thus the film-air interface has essentially the same properties as the substrate-film interface.

In implanted films, the symmetry between the two unichiral states is broken. When $\overline{M}$ inside the bubble is directed toward the implanted layer, the χ^+ state switches to the χ^- state at the same threshold as in the as-grown film, but the χ^- state never switches to the χ^+ state under the action of an expanding bias field pulse. The model for the implanted layer accounts for this behavior by the assumption that, at the implanted surface, the spins are fixed along the direction of the stray field. Therefore, at the implanted surface, the nucleation of HBL's can occur but not their annihilation. The nucleation process does not require the rotation of the surface spins. On the other hand, the annihilation of an HBL requires a 360^o rotation of the surface spin. When this is prohibited, the evolution of the spin configuration in time is modified. The new motion for a χ^- state is shown in Fig. (4.9). The static unichiral configuration is shown in (a). When an expanding pulse is applied, an HBL nucleates at the as-grown (top) surface, as shown in (b). When the HBL reaches the implanted surface, (c), it cannot punch-through because of the influence of the pinning condition. Meanwhile, since the drive field produces a continual increase in $\overline{\phi}$, a new HBL nucleates at the implanted surface, somewhat further into the bulk than the position of the trapped HBL (d). Except for the region that is closest to the implanted layer, the spin configuration of the wall after the nucleation of the second HBL is the same as in as-grown films. However, if the pulse is terminated at this point, the

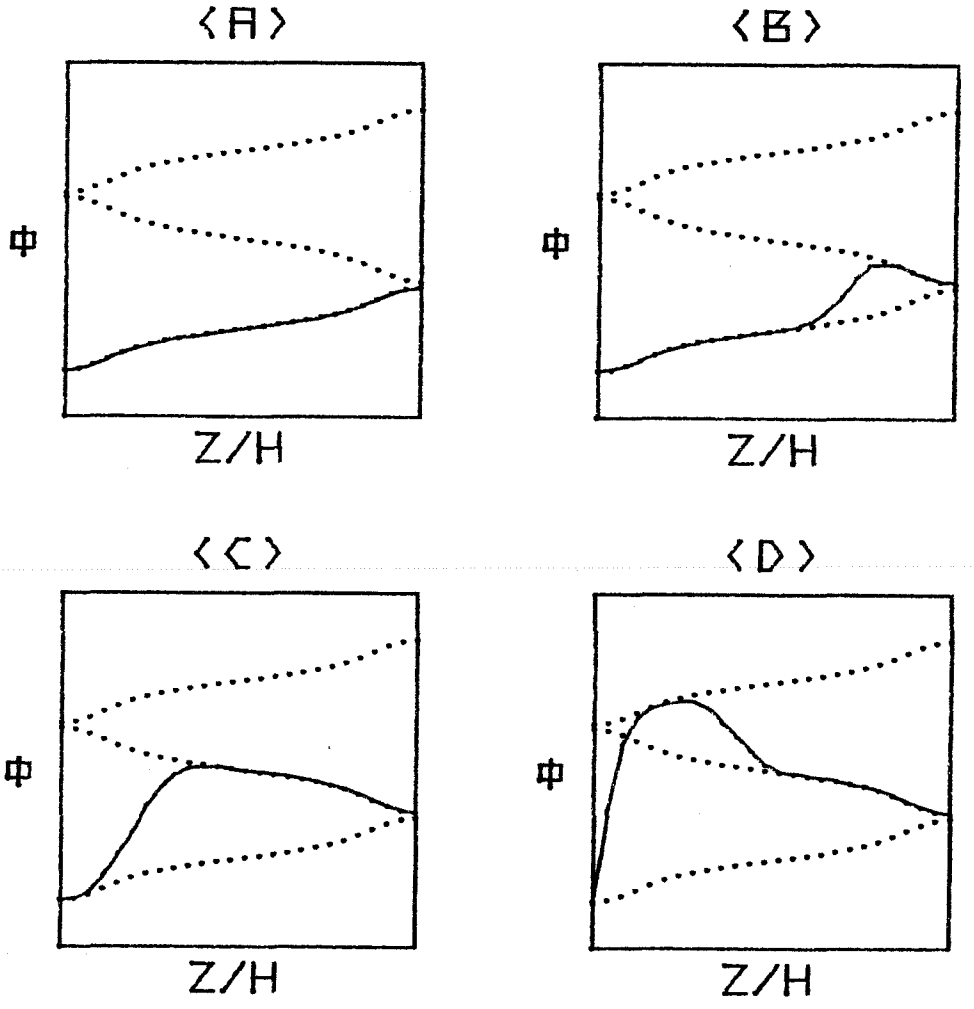

Fig. (4. 9). The time evolution of the spin configuration of a χ^- state when an expanding bias pulse is applied. The bottom film surface is implanted.

spin configuration will relax to the original chirality even though more than 180^{o} of $\bar{\phi}$ rotation occured during the pulse. The state will therefore not switch chirality. On the other hand, if the HBL is nucleated at the implanted surface (as in the χ^{+} state), then it will punch-through at the as-grown surface, changing the state. The behavior of the unichiral states are clearly asymmetric.

Portions of the implanted layer can be etched away to determine to what extent punch-through suppression depends on layer thickness. This experiment was performed on the film F19-32, for etching depths up to 0.2 μm. It was found that punch-through is suppressed for this film if less than 0.15 μm is etched from the implanted layer. This is the same threshold as for the disappearance of hard bubbles, discussed in Chapter 3. It is also the same thickness as that calculated in Chapter 3 that gives an in-plane layer. The transition from punch-through suppression to punch-through also marks the disappearance of closure domains as seen by the ferrofluid technique. Only a small in-plane field is needed for the suppression of punch-through.

4.2.2 Stable horizontal Bloch line states

The presence of an implanted layer in magnetic bubble films provides the necessary condition for the creation of new bubble states[8,9,10] that are not observed in as-grown films. These states have a structure which includes an HBL lying in the film mid-plane, stretching completely around the bubble circumference, as indicated in Fig. (4.10a). An example of this type of wall structure is shown in Fig. (4.10b). The

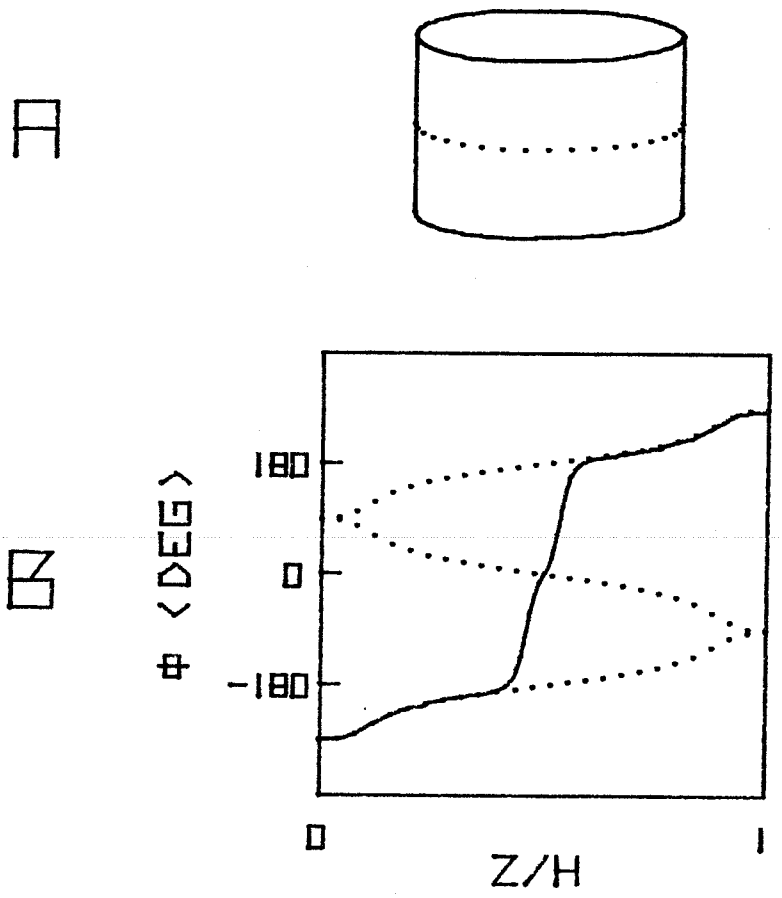

Fig. (4.10). (a) The location of the 2π HBL in the k=2 state.
(b) The spin configuration in the k=2 state.

azimuthal angle of the spin orientation is plotted as a function of position through the film thickness. The structure was calculated numerically with the method described earlier, using the material characteristics of the film 2-12-63. Unichiral wall configurations are shown by the dotted lines. The particular state shown here has a 2π HBL localized in the film mid-plane, separating two halves of a χ^+ wall structure. In a similar fashion, all other members of this group of bubble states also contain two wall sections of the same chirality, either χ^+ or χ^-, separated by an HBL. The total twist in the HBL is some multiple of 2π. Each state has the designation k^i, where k is the number of π twists and i is either + or - depending on the sign of the unichiral wall section. For example, the state in Fig. (4.10b) is a $k=2^+$ state. Unlike the unwinding wall structures with statically stable HBL's[11,12], these so-called k-states have a net twist in the wall over the film thickness that is greater than π. Thus they are the horizontal analog of the vertical winding structures with nonzero net twist that are found in hard bubbles.

The k-states are statically stable in the absence of external in-plane fields, making them different from other structures with HBL's. Because the magnitude of the twist in the spin orientation from one surface to the other is greater than π, a k-state can be destroyed only if the HBL is moved to a film surface and annihilated. Such a process occurs spontaneously if the HBL energy decreases when the HBL approaches a surface. This, in fact, does occur for the normal type of HBL's that are generated during wall motion. As described in Fig. (2.10), these

HBL's have a variable total twist because they connect two wall sections of opposite chirality. The twist in the HBL depends on its location with respect to the film surfaces. Its energy decreases if it moves in such a way as to decrease its total twist. Since this can be accomplished by movement toward the proper film surface, this type of HBL is not statically stable. In k-states, however, this is not the case. The magnitude of the twist in the HBL does not depend on location. Furthermore, the energy of the HBL actually increases as it moves toward the film surface because of the stray field. This occurs because in-plane fields, such as the stray field, increase the HBL energy if the total twist angle is constant. Consequently, the HBL in a k-state has a statically stable positon in the film mid-plane.

Once created, the k-states are expected to be stable in both as-grown and implanted films. Yet the appearance of these states in as-grown films is unlikely because there is no way to create the required net twist in the spin structure. For example, in order to create a k=2 state, a net twist of 6π from surface to surface must be generated. While this can not be done in as-grown films, it can in implanted films because of the pinning of the spins at the implanted layer. During wall motion, twists can be generated because the spins in the bulk precess while the spins at the implanted surface remain pinned. As was illustrated in Fig. (4.9), this leads to localized twists in the spin structure. The surface pinning condition is the essential factor in the production of k-states in implanted films.

The proposed mechanism for the creation of a k=2 state in an implanted film is given in Fig. (4.11). Each graph shows the spin configuration

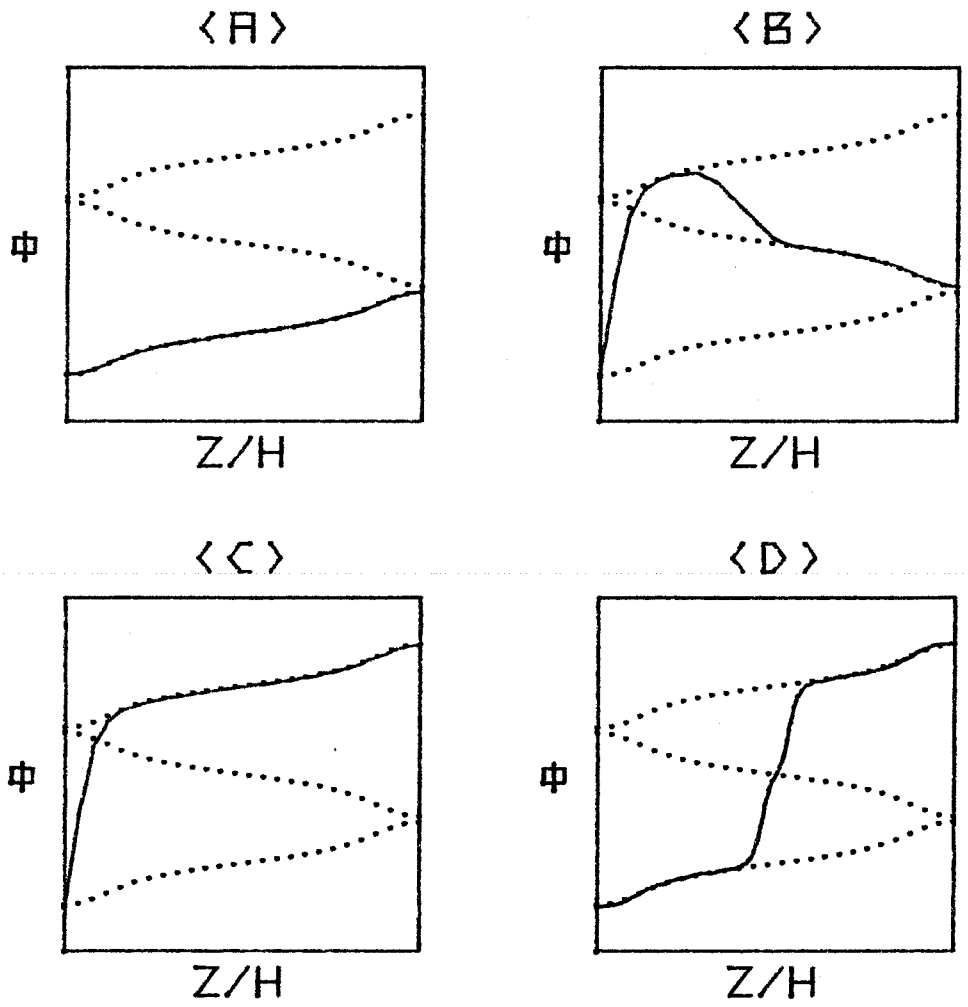

Fig. (4.11). The time evolution of the spin configuration during the creation of a k=2 state.

at a particular time during the pulse. The implanted layer is at the bottom film surface (z=0). The initial state is χ^+. If a pulse is applied so as to cause ϕ to increase, then an HBL is nucleated at the top film surface and travels down the film (see Fig. (4.9)). When it reaches the bottom surface, it does not punch-through. Instead, a new HBL is generated at that surface and begins to move toward the top film surface, as shown in (b). When it reaches the surface, punch-through occurs (c), resulting in a configuration that lies mostly along the χ^+ configuration. Except for those at the implanted surface, all the spins have precessed by 360^o. If the pulse is ended at this time, the HBL at the implanted surface will relax to the lowest energy position at the film mid-plane (d). A $k=2^+$ state is thus generated from a χ^+ state.

In order to create the k=2 state, the impulse applied to the wall by the pulse field must be large enough to cause punch-through of the secong HBL at the as-grown surface. In other words, the value of $\overline{\phi}$ (ϕ averaged over the film thickness) will have to increase by about 2π for the state to be created. This value is approximate because of the presence of the HBL at the implanted surface. Starting from the equations of motion, Eqs. (2.27) and (2.28), one can calculate the change in $\overline{\phi}$ during a pulse[13]:

$$\Delta\overline{\phi}(t) = \gamma\int_{x=0}^{t} H(x)\,dx \quad - \frac{\alpha}{\Delta}v(t) \qquad . \qquad (4.1)$$

In the calculation, the velocity v(t) is taken to be the constant saturation velocity v_s. Another factor to be taken into account is the change in

effective drive field during the pulse because of the change in domain configuration. For the film 2-12-63, the saturation velocity is 5 m/sec and the effective field gradient is 7.3 Oe/ μm. Thus, when using a pulse with a large fall-time, a 2π twist will be generated for a 6.5 Oe pulse field. This value is therefore identified as the threshold for the generation of a k=2 state from a unichiral state.

In the film 2-12-63, a single bias field pulse with a magnitude greater than a 6.8 Oe threshold is found to convert a χ^+ state to a $k=2^+$ state. This threshold is within 5% of the predicted value. The application of two consecutive 6.8 Oe pulses to a χ^+ state produces a $k=4^+$ state. The direction of the pulses is also important for the generation of the k-states. According to the model, if the pulse direction is such as to cause the initial HBL to nucleate at the as-grown surface, then a k=2 state can be generated with $\bar{\phi} = 2\pi$. If, however, the nucleation first occurs at the implanted layer, the unichiral state will have to switch chirality before the k-state can be created. This increases the threshold for k-state generation. Following the convention that the direction of $\bar{M}$ inside the bubble is toward the implanted layer, the model predicts that the k-states are generated using the minimum threshold only for the transition χ^--to-$k=2^-$ for collapsing pulses and χ^+-to-$k=2^+$ for expanding pulses. This is observed experimentally.

The k-states each have unique dynamic properties that allow them to be distinguished from other states using high speed photography. The characteristic motion for each state is revealed using the same experimental conditions described earlier for distinguishing the unichiral states.

During the test pulse, the $k=2^+$ and $k=2^-$ states have the same asymmetric expansion shapes as the χ^+ and χ^- states, respectively. However, the k-states differ from the unichiral states with respect to the magnitude of the velocity of the fast wall section. The unichiral states show a phenomenon called initial rapid motion[14,15,16], in which the wall velocity is momentarily much larger than the saturation velocity. This occurs for a few tens of nsec before the onset of HBL nucleation. Because the k-states have statically stable HBL's, they do not show this type of motion. Consequently, the k-states do not move as far during the pulse, making them easily distinguishable for the unichiral states. The k=4 states show a lower velocity than the k=2 states because of their more complex structure. Thus it is possible to distinguish the elementary bubble states.

The k-states can be reconverted to unichiral states by destroying the statically stable HBL. This is done by applying a pulse of the appropriate sign so that the HBL is pushed towards the as-grown surface. When punch-through occurs, the wall structure assumes a purely unichiral configuration. For example, in order to convert a $k=2^+$ state back to a χ^+ state, a change in $\bar{\phi}$ of π is required. This is different from the $\Delta\bar{\phi}$ necessary for the generation of this state because the two mechanisms are different. On the other hand, the k=4 state requires a change in $\bar{\phi}$ of 2π for conversion because the twist in the HBL is now twice as large. Each of the k-states therefore has a characteristic sign or magnitude of the pulse field threshold necessary to cause a transition back to the unichiral states.

The minimum pulse length required for the reconversion of a k-state back to the original state is shown in Fig. (4.12). The experimental procedure consists of setting the collapse pulse height to 5 Oe and then steadily increasing the pulse width until all k-states have been recoverted. In (a), all the initial states were k=2 states. It can be seen that the average pulse length required for conversion is 78 nsec. Equation (4.1) can be used to calculate the change in $\overline{\phi}$ produced by this pulse. Using the measured v_s = 1.3 m/sec for the k=2 state gives a $\Delta\overline{\phi}=1.16\pi$. This is quite close to the predicted value. In (b), the data was taken for a group of bubbles that were converted from χ^+ states using two creation pulses. It can be seen that when the destruction pulse is applied, two peaks occur in the data. The first corresponds to those bubble states which were not originally converted to k=4 states. Instead, the two creation pulses sometimes produced k=2 states. This illustrates the somewhat random nature of the creation process for the higher k-states. The second peak, at the higher pulse length, corresponds to those bubble states which were originally converted to k=4 states. The average pulse length required for conversion is 138 nsec. Using Eq. (4.1) to calculate the $\Delta\overline{\phi}$ produced by the pulse gives a value of 1.77π, close to the value of 2π predicted by the model. Apparent deviations from the theoretical values for the k=2 and k=4 states are due to the difficulty of accurately measuring the wall velocity of these states during the short pulse times.

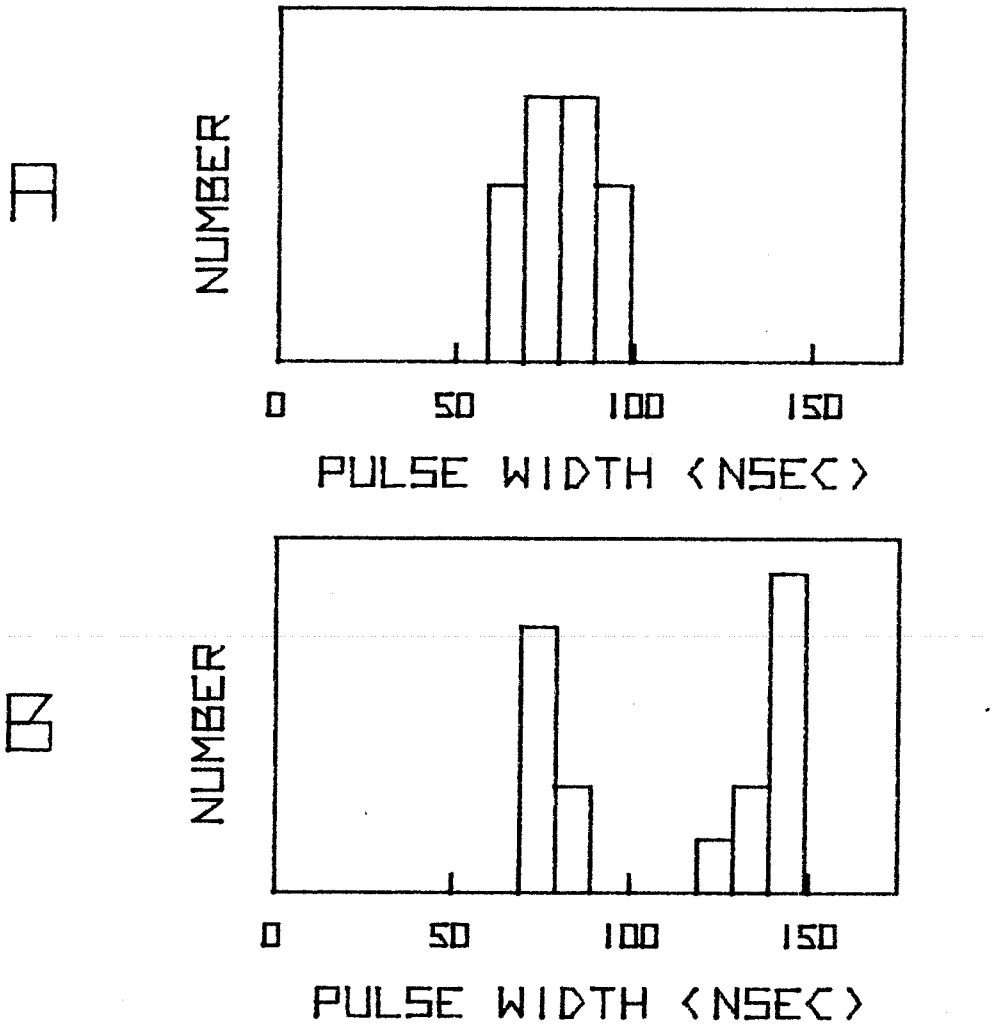

Fig. (4.12). The pulse width required to reconvert k-states back to the original unichiral states. The pulse was 5 Oe. In (a), the states were k=2 states. In (b), the states were a mixture of k=2 and k=4 states.

4.3 Conclusions

The presence of the implanted layer introduces two new effects in domain wall dynamics: the demagnetizing field associated with the closure domain in the implanted layer and the surface pinning condition. Both of these effects cause an increase in peak wall velocity when breakdown occurs at the implanted surface. Below the cap switch field, the increase is mainly due to the closure domain demagnetizing field while above the cap switch field, the increase is due to the surface pinning condition. The pinning condition also influences the transitions between bubble states. Horizontal Bloch line punch-through is suppressed at the implanted layer, causing an asymmetry in unichiral state switching. When punch-through is suppressed, a class of new bubble states can be generated. These states have statically stable horizontal Bloch lines located at the film mid-plane. As a result, they have unique dynamic characteristics.

References

1. L. Gal, Phys. Status Solidi A 31, K133 (1975).
2. F. B. Humphrey, IEEE Trans, MAG-11, 1679 (1975).
3. F. H. de Leeuw, R. van den Doel, and J. M. Robertson, 49, 768 (1978).
4. T. J. Gallagher and F. B. Humphrey, J. Appl. Phys. 50, 7856 (1979).
5. T. J. Gallagher, Kochan Ju, and F. B. Humphrey, J. Appl. Phys. 50, 997 (1979).
6. A. P. Malozemoff and J. C. Slonczewski, Phys. Rev. Lett. 29, 952 (1972).
7. T. M. Morris, G. J. Zimmer, and F. B. Humphrey, J. Appl. Phys. 47, 721 (1976).
8. E. Schlomann, AIP Conf. Proc. 10, 478 (1972).
9. A. Hubert, J. Appl. Phys. 46, 2276 (1975).
10. T. J. Gallagher and F. B. Humphrey, to be published in J. Mag. and Magn. Mat.
11. T. J. Beaulieu, B. R. Brown, B. A. Calhoun, T. Hsu and A. P. Malozemoff, AIP Conf. Proc. 10, 458 (1972).
12. T. J. Gallagher and F. B. Humphrey, J. Appl. Phys. 50, 7093 (1979).
13. J. C. Slonczewski, J. Appl. Phys. 44, 1759 (1973).
14. B. E. Argyle and A. P. Malozemoff, AIP Conf. Proc. 10, 344 (1972).
15. G. J. Zimmer, L. Gal, and F. B. Humphrey, AIP Conf. Proc. 29, 85 (1975).
16. B. E. MacNeal and F. B. Humphrey, IEEE Trans. MAG-15, 1272 (1979).

Appendix A

Domain Statics

The domain structure in magnetic bubble films has a variable geometry that depends on the magnitude of the bias field. In the absence of a bias field, the domain structure has a serpentine appearance, in which each domain is a long stripe of indefinite length. The magnetization direction in adjacent stripes is of alternating sign. If a bias field is applied, those stripes are favored whose magnetization is along the direction of the bias field. Consequently, those stripes expand in area while the others contract. At higher bias fields, there are a few isolated stripes, in which $\overline{M}$ is opposed to the bias field, surrounded by a large area in which $\overline{M}$ is along the bias field. At still higher fields, the stripes contract into circular bubble domains. Bubbles are stable for a range of bias fields, with the bubble diameter decreasing for increasing bias. At a certain bias field, called the collapse field, bubbles disappear, leaving a saturated film.

The static size and stability of bubble domains have been exhaustively analyzed[1]. These properties can be described using a model of the domain wall in which only its surface energy density is taken into account. The domain size is found by considering the total energy, composed of wall energy, demagnetizing energy, and applied field energy. For a bubble of radius r in a film of thickness h, the total energy is

$$E_T = 2\pi rh\sigma_w + E_D + 2MH_B\pi r^2 h \quad , \qquad (A.1)$$

where σ_w is the wall surface energy density, H_B is the bias field, and E_D is the demagnetizing energy. The demagnetizing energy involves the magnetic fields arising from the divergence of the magnetization at the film surfaces.

The bubble radius is found by considering changes in the total energy produced by changes in the radius. The derivative of the total energy with respect to the radius is

$$\frac{dE_T}{dr} = 2\pi h\sigma_w + 4\pi Mrh\bar{H}_D + 4\pi MH_B rh \quad , \qquad (A.2)$$

where $\bar{H}_D$ is the z component of the demagnetizing field at the domain wall, averaged over the film thickness. An exact representation for $\bar{H}_D$ involves elliptic integrals. However, an approximation has been derived[2]:

$$\bar{H}_D = \frac{-4\pi M}{1+3r/2h} \quad , \qquad (A.3)$$

which is within a few percent of the exact value. Using standard methods, the static bubble radius can be found as a function of bias field. The results are shown in Fig. (A.1) for a typical film (σ_w = 0.23 erg/cm^2, h = 6.8 μm, 4πM = 184.4 Oe). In this case, the radius decreases from about 10 μm at 50 Oe bias field to a radius of 2.1 μm at the 88 Oe collapse field.

In a similar manner, the width of a stripe domain can be calculated. In this case, the energy per unit length is

$$E_T = 2h\sigma_w + E_D + 2hwH_BM \quad , \qquad (A.4)$$

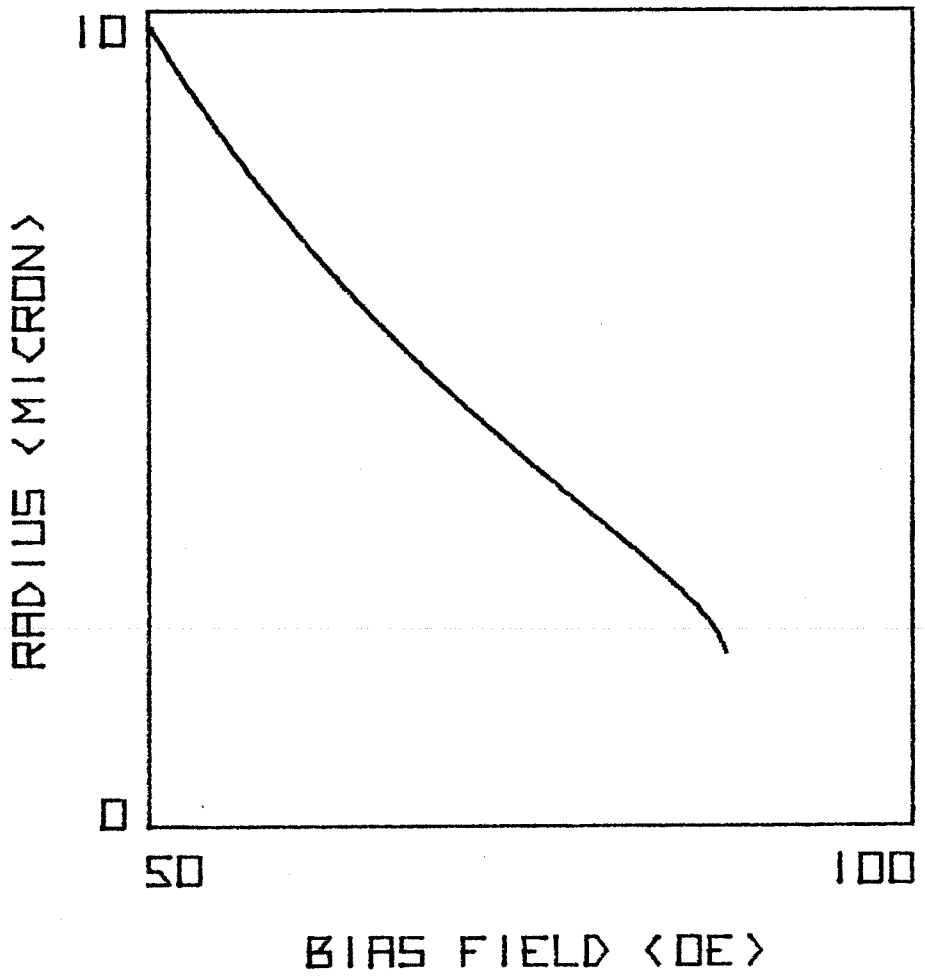

Fig. (A.1). Radius versus bias field for a bubble domain.

where w is the width of the stripe. The demagnetizing energy E_D is given by[3]

$$E_D = -8hwM^2 \{2\tan^{-1}(\frac{h}{w}) + \frac{h}{2w}\ln(1+\frac{w^2}{h^2}) - \frac{w}{2h}\ln(1+\frac{h^2}{w^2})\} \quad . \quad (A.5)$$

The width can be found in the standard way by minimizing the total energy.

Of greater interest to the work on stripe head propagation in Chapter 4 is the determination of the critical field[4] for which the stripe head is in a state of neutral equilibrium. Such a state exists when changes in the stripe length cause no change in total energy. Thus the conditions for neutral stability are

$$E_T = 0 \quad (A.6)$$

and

$$\frac{dE_T}{dw} = 0 \quad . \quad (A.7)$$

The critical field for a typical film is usually between .3(4πM) and .4(4πM). For the film used in the figure, the calculation gives a critical field of .397(4πM) = 73 Oe.

References

1. A. A. Thiele, J. Appl. Phys. 41, 1139 (1970).

2. H. Callen and R. M. Josephs, J. Appl. Phys. 42, 1977 (1971).

3. F. A. de Jonge and W. F. Druyvesteyn, Festkörperprobleme, 12, 531 (1972).

4. L. Gal, Phys. Status Solidi, A 31, K133 (1975).

Appendix B

Stripe Head Propagation Experiment

Straight isolated stripes are necessary for the stripe head experiment. One way[1] to achieve this is by depositing a current conductor on the film surface, in the shape of a hairpin loop. When current is sent through the conductor, the resulting magnetic fields produce a potential well to confine the stripe to the desired location. However, another method[2] is available which avoids the use of the inconvenient conductor pattern. In this method, a large uniform in-plane field (typically 200 Oe) is used to create an array of straight stripes. This is effective because the domain wall energy is minimized when the external in-plane field is parallel to the wall. The parallel stripe array is established by first saturating the film with a high bias field and then lowering the bias field while applying the in-plane field. This causes the film to demagnetize in such a way that the newly formed stripe domains are all parallel. The stripes can be chopped[3] into a few segments by applying short collapse pulses. In this way, the stripe heads of a number of straight stripe domains can be produced in the field of view of the microscope.

In order that the stripe head be in a state of neutral stability, the bias field must be set at a certain critical value (Appendix A). For bias fields slightly above the critical field, the stripe domains will contract spontaneously, while for fields below the critical field, the stripe domains expand spontaneously. If magnetic films had no coercive force, then the critical field could be set exactly by

observing the response of the stripe heads. However, in real films, wall motion is prevented unless the drive field on the wall is greater than the coercive field (typically 1 Oe). This defect can be overcome, allowing the bias field to be set exactly, with the following method. A sequence of identical bias field pulses, but of alternating sign, is applied to the stripe. Each pulse has a magnitude slightly greater than the coercive field and a width of a few hundred nsec. These pulses cause the stripe head to move back and forth, in an alternating sequence of expanding and contracting motions. If the bias field is not set at the critical field, the stripe head will drift in one direction during the alternating motion. If the bias field is too high, the stripe will steadily contract; if it is too low, the stripe expands. The bias field can then be adjusted until there is no drifting motion. Typically, the bias field must be set to within a few tenths of an Oe for the stripe to remain motionless.

The critical field varies slightly with in-plane field. Thus it must be determined for every in-plane field for which experiments will be performed. Experiments with stripe head propagation can be done even in the absence of an in-plane field. This is accomplished by establishing a straight stripe at a high in-plane field and then lowering the in-plane field gradually to zero while constantly readjusting the bias field to the critical value.

Once the critical field is set, the velocity of the stripe head can be measured by applying single bias field pulses to move the wall. The stripe head can be propagated over long distances (e.g. 50 μm)

at a constant drive field. In some magnetic films there is no overshoot after the pulse ends, so that high speed photography is not even required to measure the wall velocity.

References

1. G. J. Zimmer, L. Gal, and F. B. Humphrey, J. Appl. Phys. 48, 362 (1977).

2. T. J. Gallagher and F. B. Humphrey, J. Appl. Phys. 50, 7856 (1979).

3. T. J. Gallagher and F. B. Humphrey, Appl. Phys. Lett. 31, 235 (1977).

Appendix C

Optical Sampling Microscope

The optical sampling microscope[1] provides single exposure photographs of bubble domains in motion. It consists of a pulsed laser, a polarizing microscope, a video recording system, magnetic field generators, and a timing control unit. The control unit allows a programmed sequence of magnetic field variations to be applied to the magnetic film. The laser can be triggered at any desired time during this sequence. By controlling the timing of the laser, the instantaneous bubble velocity can be measured.

A block diagram of the optical sampling microscope is shown in Fig. (C.1). The vertical synchronization signal of the TV camera is used to initiate the trigger amplifier of the control unit. As specified by the program stored in the control unit, trigger pulses are sent to particular pulse generators and to the laser. The laser trigger is delayed for a time interval set either manually or by an automatic sweep unit. The output of the pulse generators is monitored using a current transformer while the laser flash is monitored by a photodiode. By displaying both signals on an oscilloscope, the relative timing of the magnetic field pulse and the laser can be determined.

The laser system consists of a dye cell containing Rhodamine 6G laser dye, pumped by a flowing nitrogen laser. The nitrogen laser produces a 10 nsec ultraviolet light pulse with a peak power of 100 kw. The output of the dye cell is in the visible spectrum, with a wavelength

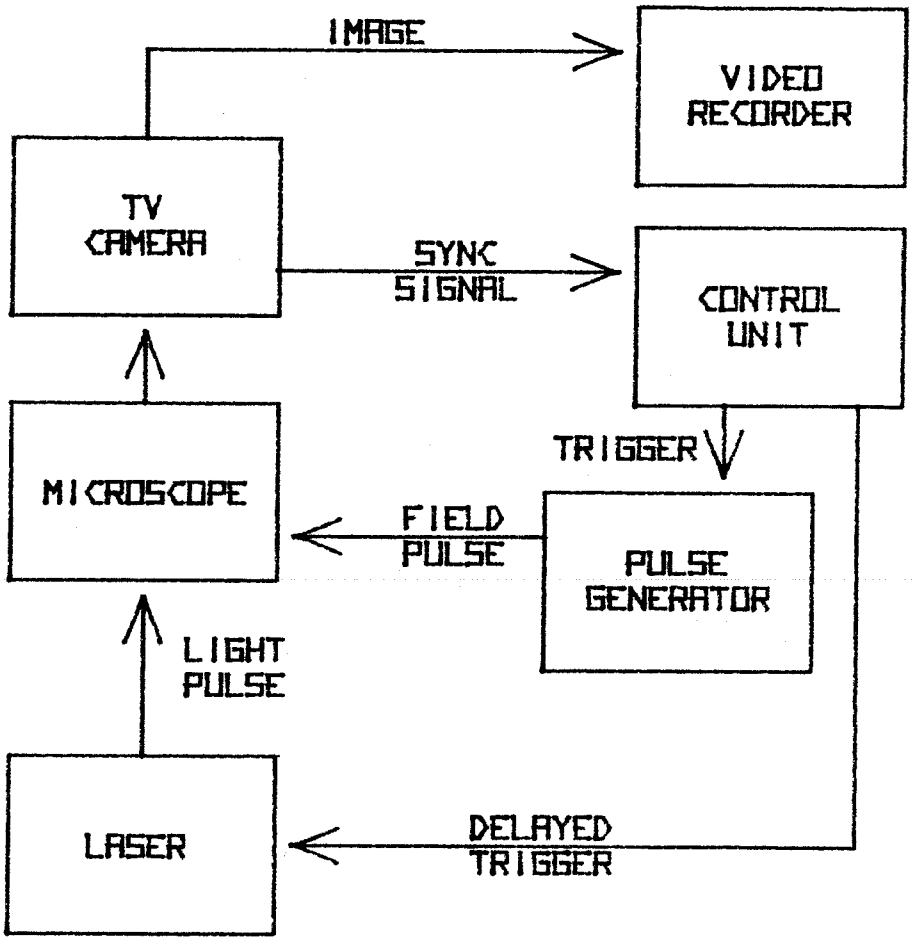

Fig. (C.1). Block diagram of the optical sampling microscope.

of 5800 $\mathring{A}$, and a peak power of about 1 kw. At this wavelength, bubble garnet films have a relatively low absorption and a large enough Faraday rotation (about 1^{o}) to permit the observation of the domains.

Magnetic field pulses are generated using a small pancake coil (1 mm in diameter) driven by one or more HP 214 pulse generators. The rise-time of the combined system is about 10 nsec.

References

1. F. B. Humphrey, IEEE Trans. MAG-11, 1679 (1975).

Appendix D

State Identification Experiment

Bubble states are identified by their characteristic shape during bias field pulsing in the presence of an in-plane field[1]. High speed photography is used to observe the domains; the images of the bubbles in motion are displayed using a TV camera and video recorder. The use of the proper bias field pulse and in-plane field (Appendix E) allows a non-destructive identification of bubble states to be made instantaneously.

The pulse sequence used to test the bubble shape is shown in Fig. (D.1). The transient bubble shape is observed during a burst of bias field test pulses. The laser is positioned both before each pulse and at some point near the end of each pulse. During the burst of test pulses, a low amplitude uniform in-plane field is also applied to the film. The state is identified during a single burst of test pulses. Each group of pulses is separated by a large enough time to allow switching pulses (dotted line) to be applied, if desired. The complexity of the pulse sequence makes mandatory the ability to program the various pulse generators, the in-plane field power supply, and the laser trigger.

The effect of triggering the laser at twice the frequency of the test pulses is to create a double exposure of the bubble domain on the TV screen. The static position of the bubble is revealed by the laser flash set before the test pulse while the transient shape is revealed by the laser flash set during the pulse. A burst of test pulses, with each pulse separated by about 30 msec, is used to prolong the image on

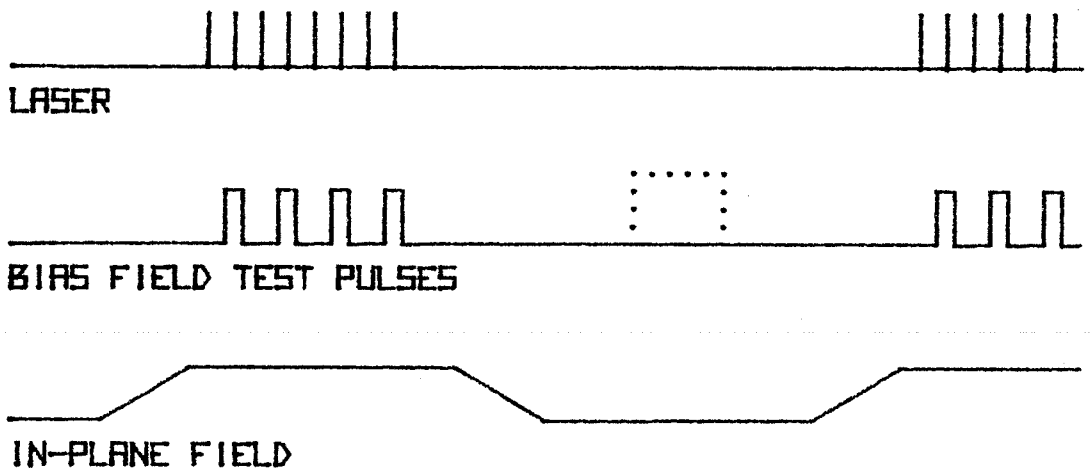

Fig. (D.1). Pulse sequence for the state identification experiment.

the TV monitor. As a result, the motion of individual sections of the bubble wall can be observed easily and the state identification made immediately.

References

1. T. J. Gallagher, Kochan Ju, and F. B. Humphrey, J. Appl. Phys. 50, 997 (1979).

Appendix E

Dynamics of Unichiral Magnetic Bubbles with In-Plane Field

E.1 Introduction

Bubble wall structure can be detected by the use of high speed photography. Chains of VBL's can be detected because they slow the wall sections containing them[1,2]. Transient photographs of moving domain walls can therefore be used to measure the position and velocity of such wall structure. Single VBL's can also be detected by high speed photography when an in-plane field is applied during low amplitude bias field pulsing. Unichiral bubbles can also be distinguished. In a unichiral bubble, the wall sections parallel to the in-plane field have quite different velocities during radial expansion[3]. The wall section whose magnetization direction is opposed to the in-plane field has a very low initial velocity compared to the velocity of the wall whose magnetization is along the in-plane field. The two unichiral states can therefore be distinguished because the slow wall is on opposite sides of the bubble. Thus the use of high speed photography provides a simple, direct way of bubble state determination.

In-plane fields can form statically stable HBL's. Such structure arises because of the static horizontal wall twist produced by the surface stray field. This stray field, caused by the divergence of the magnetization at the film surfaces, is directed in the plane of the film and perpendicular to the domain wall. It is zero in the center of the film and increases in magnitude, but in opposite directions, nearer the two

film surfaces. When no in-plane field is applied, the azimuthal angle of the spins changes by about 180^{o} from one surface to the other. Applied fields change the twist structure. If an in-plane field is applied along the direction of the mid-wall magnetization, this total twist is reduced. This occurs because the surface spins are rotated toward the direction of the spin in the center of the wall. On the other hand, if the in-plane field is applied in a direction opposite to that of the mid-wall magnetization, a more complicated twist is expected, as was first calculated by Hubert[4]. The spins near the surface rotate to a direction nearer that of the in-plane field, while the spins in the center of the film remain opposed to the in-plane field direction. The result is a rather localized 2π twist in the center of the film. The magnitude of the in-plane field necessary to stabilize this structure is on the order of 10 Oe for typical bubble garnet materials. For those wall sections of the bubble that are not parallel to the in-plane field, the twist is different. Beaulieu, et al.[5] have qualitatively described this twist when an in-plane field is applied. They used their model to account for the switching to other bubble states during gradient propagation.

This appendix[6] studies the statics and dynamics of unichiral bubbles in the presence of an in-plane field. The static structure of the two walls parallel to the in-plane field will be discussed. The dynamic properties of these two wall sections will be investigated. It will be seen that the motion of the wall section whose center spin is along the in-plane field is best described by a one-dimensional wall

model whereas the motion of the wall whose center spin is opposed to the in-plane field requires a 2π HBL. Punch-through of the 2π HBL will be used to explain the switching of unichiral bubble states to those states with two opposite-winding VBL's.

E.2 Theory

The calculated static spin configuration in the domain wall with an in-plane field applied along the direction of the center spin is shown in Fig. (E.1a). The numerical calculation was made as described in Chapter 2. The azimuthal angle for individual spins in the wall is plotted as a function of position through the thickness, with the in-plane field H_1 as a parameter. It can be seen that the spin structure is gradually twisted about the center of the film. Without the in-plane field, the total angular twist in the wall is nearly 180^{o}. When an in-plane field is applied, the total twist angle is decreased while the form of the twist is retained. There is an 18% change in total twist when the in-plane field chnages from 0 to 20 Oe. For this wall, with the center spin along the in-plane field, the in-plane field has a rather small effect on the spin structure.

For the wall with an in-plane field applied in a direction opposite to the center spin, the calculated static spin configuration is shown in Fig. (E.1b). The azimuthal angle for individual spins within the wall is plotted as a function of position through the thickness, with in-plane field magnitude as a parameter. It can be seen that the effect of the in-plane field is to increase the wall twist, while retaining the

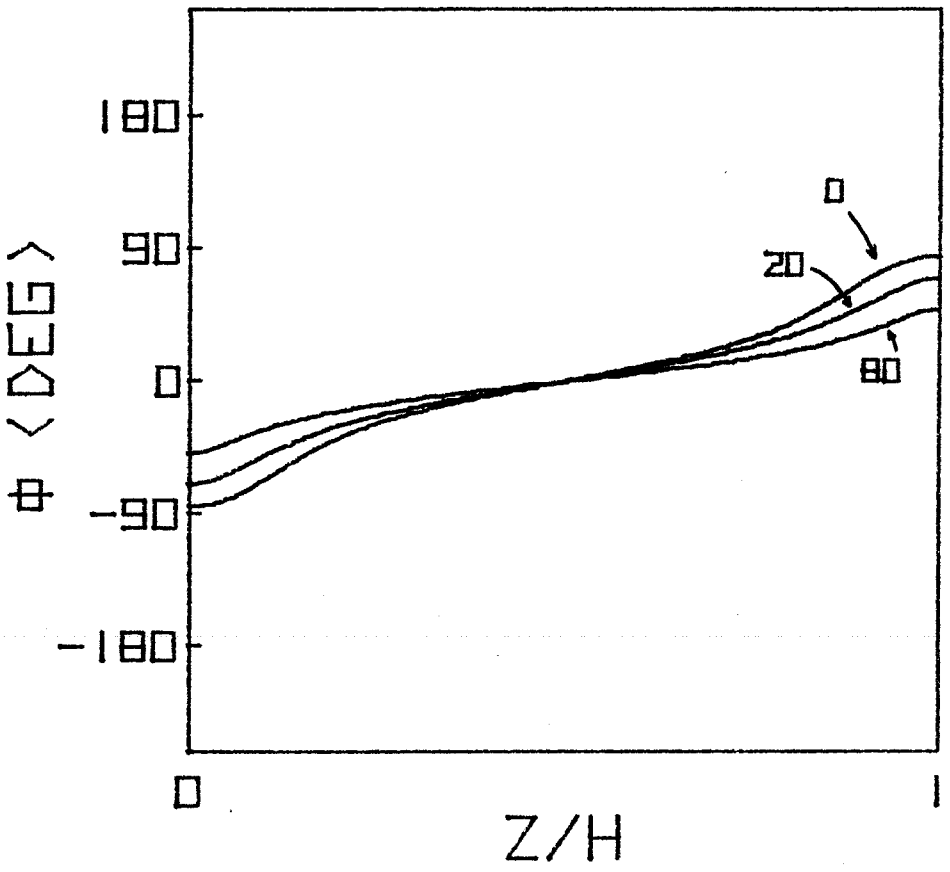

Fig. (E.1a). Wall structure for in-plane fields applied along the center spin.

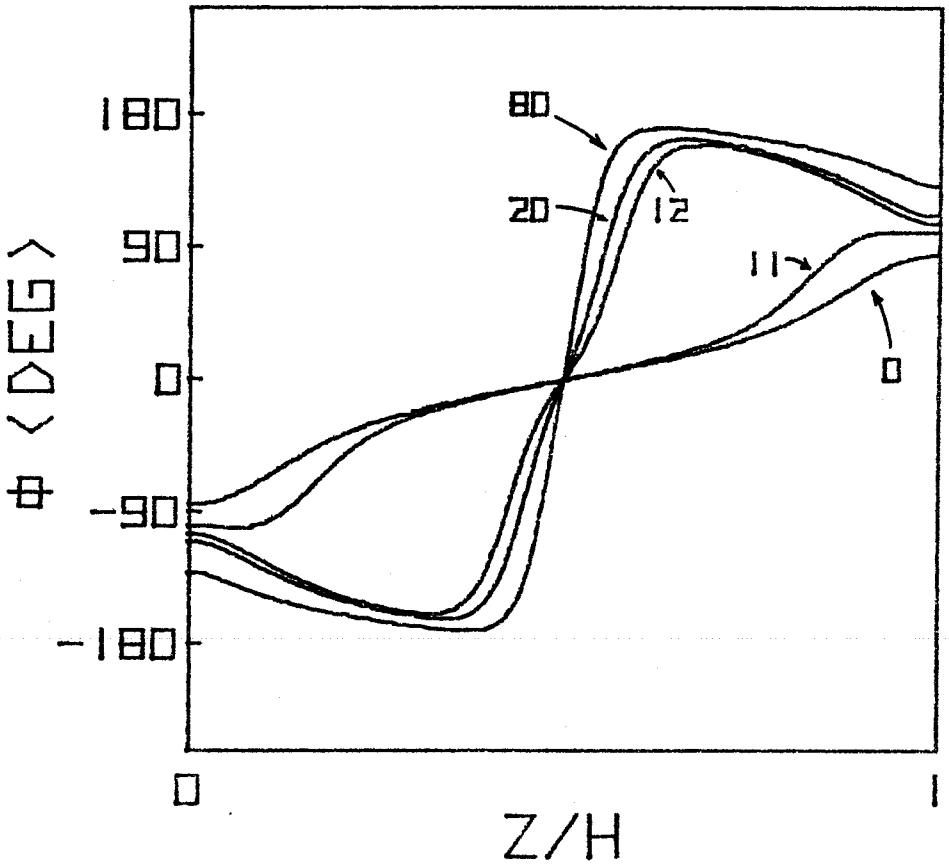

Fig. (E.1b). Wall structure for in-plane fields applied opposite to the center spin.

symmetry about the center of the film. For an in-plane field less than 11 Oe, the distribution has essentially the same shape as the zero in-plane field solution. However, above a threshold, which in this case is 12 Oe, the distribution changes radically. A localized 2π twist, called a 2π horizontal Bloch line (HBL) is formed in the center of the film. This 2π HBL becomes compressed as the in-plane field magnitude is increased. The existence of the 2π HBL makes the static structure of this wall very different from a wall with an in-plane field applied in the opposite direction.

The nucleation field of the 2π HBL is determined by a balance between the compressional force on the HBL due to the in-plane field and the expanding force due to the Bloch line energy. Numerical calculations give the value of the nucleation field as

$$\frac{H_{nucl}}{4M} = 3.95 \left(\frac{\sqrt{A}}{\sqrt{\pi M^2 h^2}} + .008\right) \qquad \text{(E.1)}$$

for $0.025 < \frac{\sqrt{A}}{\sqrt{\pi M^2 h^2}} < 0.06$, which is the range for this factor found in the usual bubble materials. This formula was derived in the limit of high Q using the same functional form of the stray field as was used for the curves in Fig. (E.1). It is interesting to compare this result with an estimate made by Argyle, et al. (Appendix C of Ref. 7):

$$\frac{H_{nucl}}{4M} = \pi\sqrt{2}\ \frac{\sqrt{A}}{\sqrt{\pi M^2 h^2}} \quad . \qquad \text{(E.2)}$$

Even though the estimate was derived using a number of assumptions involving the Bloch line energy that are unnecessary in the numerical calculations, it is certainly a good approximation, yielding a value of

11 Oe for the film used here, when the actual field as given by the numerical calculations is 12 Oe. The magnitude of the in-plane field required to nucleate a 2π HBL in the wall section whose center spin is opposed to the in-plane field is very moderate in most materials.

The effect of the angle between the in-plane field and the domain wall must be considered, since an in-plane field applied to a cylindrical bubble domain has sections of wall at all angles. For in-plane field orientations with a component along the center spin, little effect should be expected, as in Fig. (E.1a). For other angles, however, a 2π HBL should exist as long as the component of field along the wall is greater than the nucleation field for the 2π HBL. The calculated static spin distribution for this case is shown in Fig. (E.2). Figure (E.2a) shows the azimuthal angle for individual spins in the wall, plotted as a function of position through the thickness, with the orientation of a 20 Oe in-plane field as a parameter. The angle of the in-plane field is defined using the same reference system as that for the azimuthal angle of the spins. For all angles shown, the component of field along the wall is greater than the nucleation threshold so that a 2π HBL is expected. It can be seen that a 2π HBL exists for each of the angles shown, and that the position of the HBL depends on the angle of the applied field. The center of the 2π HBL moves nearer the film surfaces for angles further from $\theta = 180^{o}$. The 20 Oe in-plane field stabilizes the 2π HBL over a 106^{o} arc of the bubble wall with the 2π HBL oriented at an angle to the film surfaces.

A more qualitative view of the static 2π twist can be seen in Fig. (E.2b). The twist over the entire bubble wall can be described

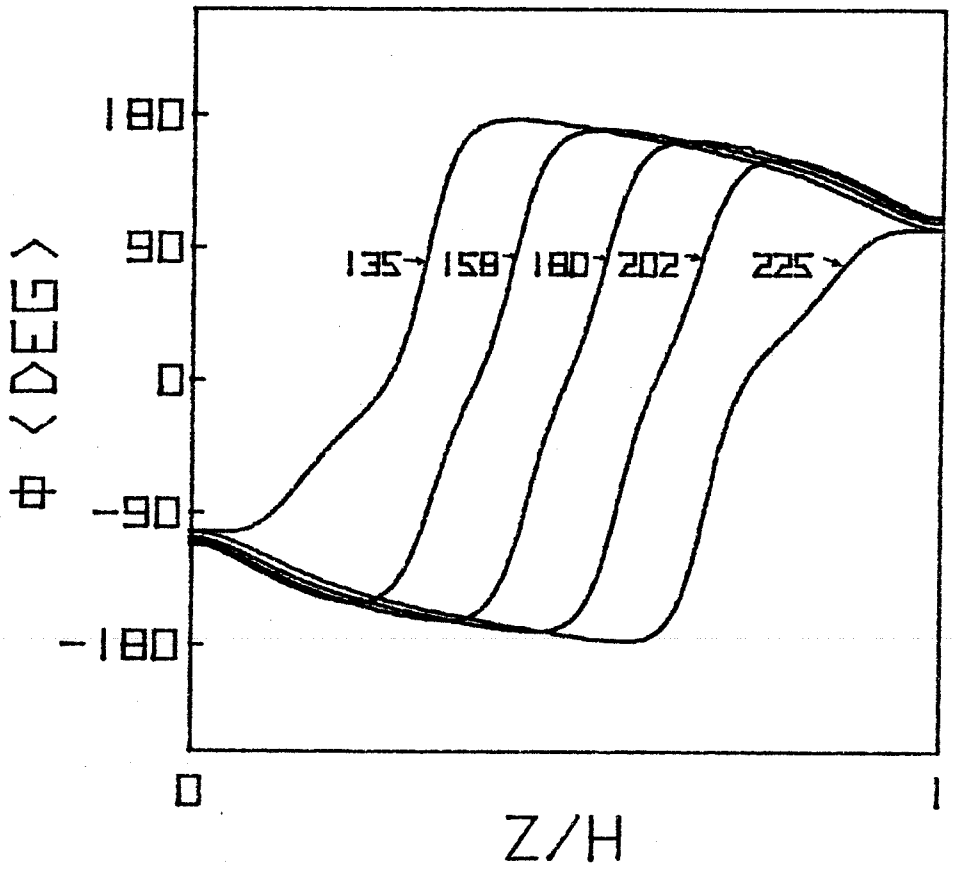

Fig. (E.2a). Wall structure for a 20 Oe in-plane field, with angle of the applied in-plane field as a parameter.

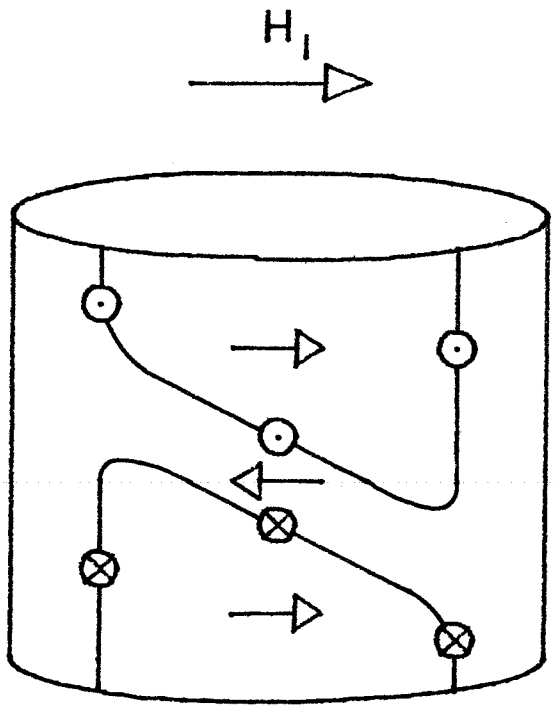

Fig. (E.2b). The location of the wall twist in a unichiral bubble for a 20 Oe in-plane field. The arrows show the direction of $\overline{M}$.

as a slanted HBL flanked by a pair of vertical Bloch lines (VBL's). This configuration is the 1H bubble state described by Beaulieu, et al.[5] except that this more exact analysis shows that the 2π HBL is slanted. These numerical calculations can not deal with the vertical twist in the wall because the exchange torque due to changes in ϕ along the wall in the horizontal direction was not included; however, VBL's as shown are certainly reasonable, separating that section of the wall where the component of the in-plane field is below H_{nucl} from that section of the wall where the in-plane field is greater than H_{nucl}. Also, because the 3 μm radius of curvature of the bubble wall is so much larger than the wall width, wall curvature effects are minimal. Certainly Fig. (E.2b) must be very close to the actual spin arrangement.

The dynamic behavior of unichiral bubbles in an applied in-plane field can be analyzed by focusing on the various wall sections individually in much the same way that the static case was done. The most important sections are those that are parallel to the in-plane field. For the normal wall section, which has the gradually twisting wall structure shown in Fig. (E.1a), the one-dimensional wall model[8,9] will be used, as described in Chapter 2. This model has the advantage of being conceptually simple. It assumes that the spins in the wall lie in a plane and precess uniformly. In this analysis, it will also be assumed that the wall width always remains constant. With these assumptions, the fundamental equations of motion for a one-dimensional wall can be written as

$$\dot{\phi} = \gamma H_z - \frac{\alpha}{\Delta}\dot{q} \qquad (E.3)$$

and

$$\dot{q} = 2\pi\Delta\gamma M \sin 2\phi + \frac{\pi\Delta\gamma}{2} H_x \sin\phi + \alpha\Delta\dot{\phi} \quad , \qquad (E.4)$$

where γ is the gyromagnetic ratio and q is the wall displacement. Direct numerical integration gives the displacement of the normal wall as a function of time.

The wall section with a 2π HBL is modeled following Slonczewski's analysis of HBL motion. It is assumed that the wall is always in a state of static equilibrium in a coordinate system moving along with the wall. The spin configuration is determined by minimizing the total energy with $\bar{\phi}$, the value of the azimuthal angle averaged over the film thickness, held constant. In numerical calculations, this means that the following differential equation is solved for a given wall velocity, $\dot{q}$, subject to the boundary condition that $\frac{d\phi}{dz} = 0$ at the film surfaces (Equation 3.1 of Ref. 10):

$$\frac{\delta\sigma}{\delta\phi} = \frac{2M\dot{q}}{\gamma} \quad , \qquad (E.5)$$

where σ is defined as in Chapter 2 and $\frac{\delta}{\delta\phi}$ is the functional derivative. The solution gives the relation between the wall velocity and the average azimuthal angle. This relation, along with the momentum conservation relation, $\dot{\bar{\phi}} = \gamma H_z - \frac{\alpha}{\Delta}\dot{q}$, allows the motion of the 2π twisted wall to be predicted.

The spin configuration of the moving 2π twisted wall is shown in Fig. (E.3) for a 20 Oe in-plane field applied directly opposite to the center spin. Here the azimuthal angle for individual spins in the wall is plotted as a function of position in the wall with the steady-state

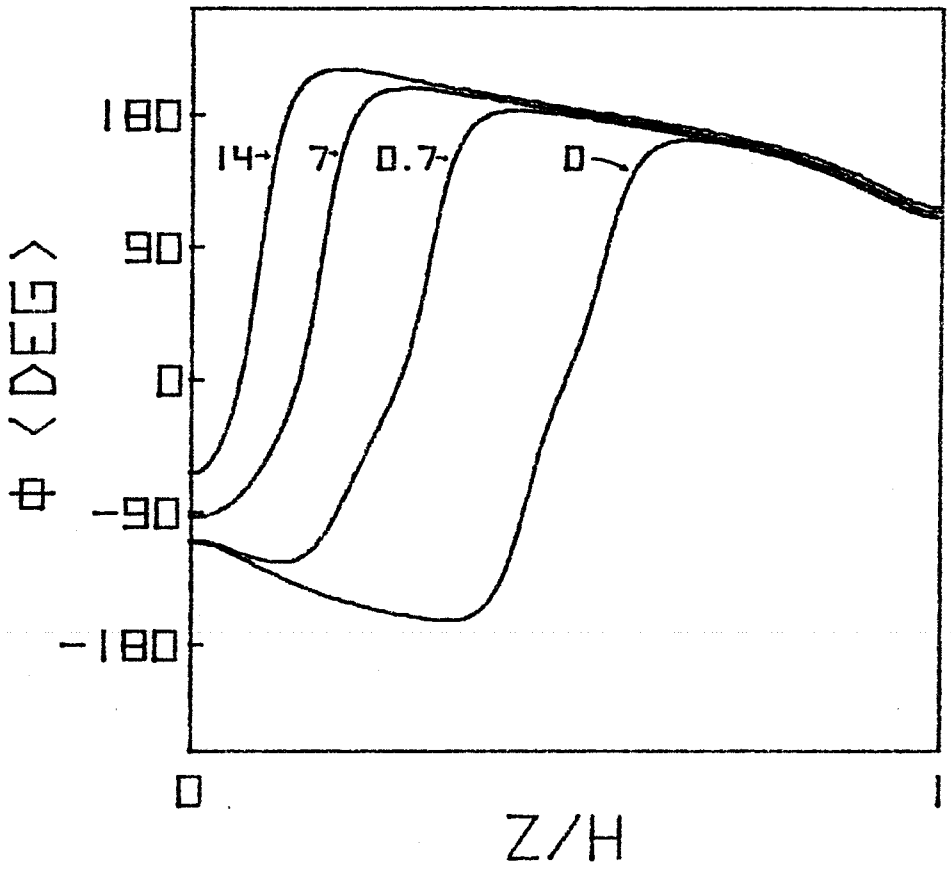

Fig. (E.3). Wall structure with steady-state velocity (m/sec) as a parameter. A 20 Oe in-plane field is applied opposite to the center spin.

velocity as a parameter. The zero velocity curve is the distribution seen previously for static equilibrium with a 20 Oe in-plane field. As the steady-state velocity increases, the position of the 2π HBL changes, moving closer to the film surface (for the bubble of Fig. (E.2b), the bottom surface). The highest velocity (v = 14 m/sec) for which there is a stable solution corresponds to a $\overline{\phi}$ of 155^{o}. This value of the peak velocity can be compared to the 20 m/sec peak velocity obtained from the standard HBL model, proposed by Slonczewski[10], in which the HBL also has a 2π twist at punch-through. The difference occurs because Slonczewski does not consider the effect of an in-plane field and because the numerical procedure used in the present work avoids a number of assumptions necessary to solve the problem analytically. This peak velocity corresponds to a peak effective drive on the wall of 2.5 Oe, obtained by dividing the velocity by the theoretical mobility, $\frac{\gamma\Delta}{\alpha}$. Above the peak value of 14 m/sec, no steady-state solution containing a 2π HBL exists. When $\overline{\phi}$ reaches 155^{o}, the process of punch-through begins, in which the 2π HBL disappears by an irreversible rotation of the spins at the surface.

Motion of the entire side of the bubble containing the 2π HBL can be deduced by calculating a spin profile similar to Fig. (E.3) for various positions along the 106^{o} length of bubble wall containing the 2π HBL. Except for the change in starting position reflecting the tilt of the 2π HBL (see Fig. (E.2)), the relative position of the 2π HBL for various wall velocities was very similar to that shown in Fig. (E.3) for the center section. A complete analysis of the actual bubble wall

motion that includes the interactions between neighboring wall elements, each with a different in-plane field orientation, is very difficult to solve and can be avoided. Since the 2π HBL moves towards the surface as a rigid structure, it is reasonable to assume that the motion of the planar wall section whose center spin is opposed to the in-plane field direction reflects the motion of the entire 2π HBL bubble wall. The wall velocity as a function of average azimuthal angle is shown in Fig. (E.4). It can be seen that the velocity of the wall is small until $\overline{\phi}$ increases to about 90^{o}. This low velocity reflects the fact that the Bloch line energy changes only slightly for a movement of the 2π HBL through the middle portion of the film, and thus $\overline{\phi}$ can increase without a large increase in energy. The wall velocity increases as the 2π HBL nears the surface because of the rapidly increasing stray field and the compression of the 2π HBL. This relatively large range of $\overline{\phi}$ for which the wall velocity is extremely low gives the very distinctive difference in motion between the normal and the 2π HBL wall section that is the basis for the chirality determination method[3].

E.3 Experimental

Bubble domains were observed using a sampling optical microscope that has been described in detail in Appendix C.

Measurements were made of the displacement of particular bubble wall sections during bias field pulsing by observing transient single exposure pictures taken at various times after the application of a bias field step change. Before each transient picture, a picture of the

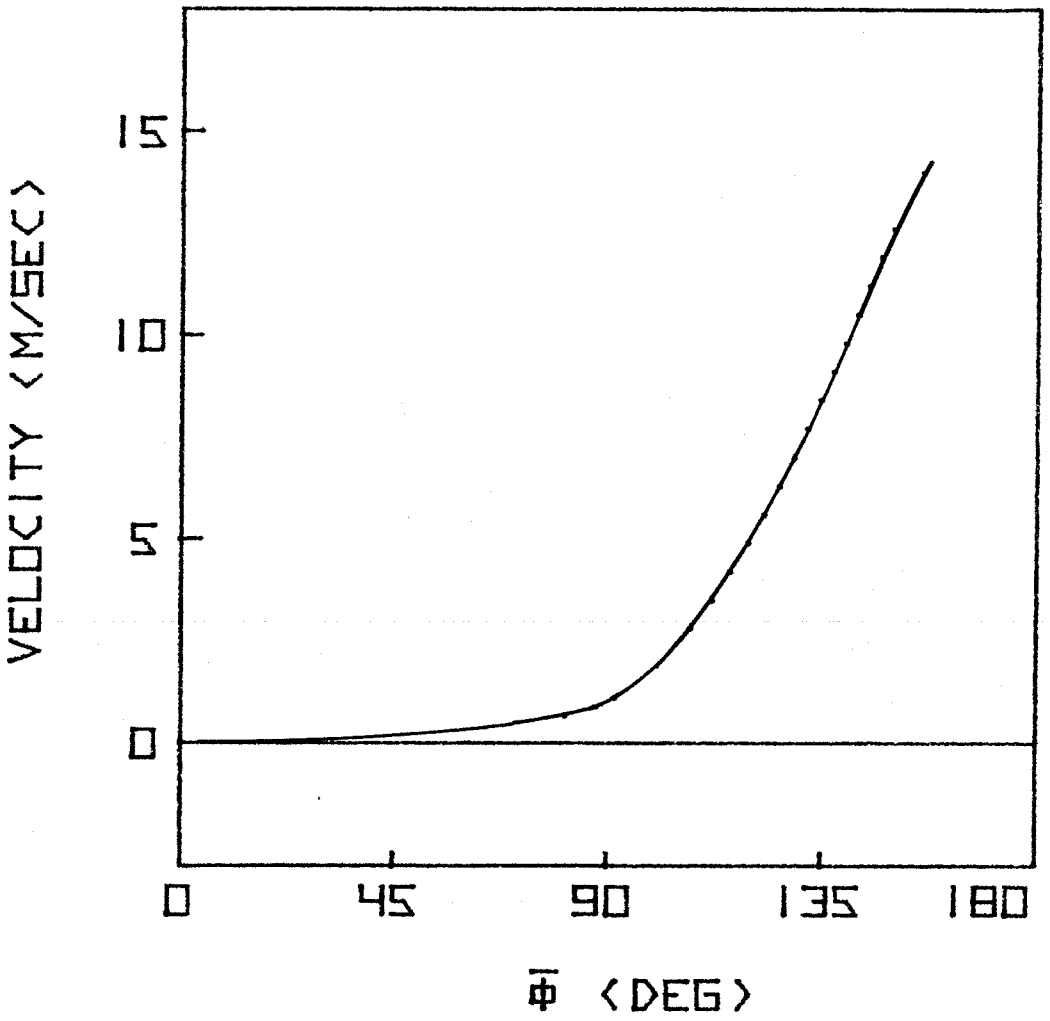

Fig. (E.4). Steady-state wall velocity as a function of average azimuthal angle.

bubble in the uniform bias field was taken so that the absolute displacement of each wall section could be accurately measured independently of the motion of the other wall sections. Bias field step changes were made by using "pulses" with a fall-time greater than 10 μsec. The first 70 nsec of wall motion was of most interest because it is the initial motion which best shows the drastic effects of static wall structure. Time sweeps were made of the delay of the light flash in respect to the bias pulse. The delay was automatically incremented by 0.2 nsec after every bias field step pulse. Data points in 2 nsec intervals were averaged; it is felt that this convenient procedure is essentially the same as taking ten measurments at a given laser delay and then incrementing the delay by 2 nsec. The diameter of the transient bubble was also obtained so that the effective drive field could be calculated.

In these experiments, the bubble state is important. The states of interest are the two unichiral states, χ^+ and χ^-, and the σ^- state, which has two opposite-winding VBL's. The χ^+ bubble is defined as having its mid-wall spins point clockwise around the bubble, when looking along the direction of the magnetization inside the bubble; the state with the counter-clockwise-directed spins is χ^-. The VBL's in the σ^- state have center spins that point radially outward from the bubble. The other possible state with two opposite-winding VBL's, σ^+, does not exist in implanted films. A convention is made for the experiments in which the direction of magnetization inside the bubble is toward the implanted layer. The existence of the implanted layer affects bubble state conversions. When bias field step changes are applied to a χ^+ bubble so as to

make the bubble expand, no state conversion ever occurs. This is not the case in as-grown films, in which suitably sized step changes cause a χ^+-to-χ^- coversion for zero in-plane field and a χ^+-to-σ^- coversion if an in-plane field of appropriate size is used[3]. On the other hand, implantation does not affect the χ^--to-χ^+ conversion without an in-plane field or the χ^--to-σ^- conversion when in-plane fields are applied. Thus, χ^+ states are used for the wall displacement measurements described earlier, for which state conversions are inconvenient, while χ^- states are used for experiments involving state conversions.

State switching occurs in certain ranges of bias pulse amplitude, depending on the chirality of the bubble. In this case, for measurements of wall displacement of a particular bubble state, a bias pulse of the appropriate size was applied after the first pulse to convert the bubble back to the original state. For state switching experiments, such as those associated with Fig. (E.6), a more complicated pulse and observation sequence was used so that state switching could be continuously monitored[3]. Between each bias pulse, the state was monitored by observing the double exposure picture of the bubble in static equilibrium together with the transient shape 30 nsec after the application of a 7 Oe expansion pulse in a 20 Oe in-plane field. For these conditions, the two chiralities of a unichiral bubble can be easily and nondestructively identified by observing which side of the bubble has the slow wall in the transient picture. For σ^+ and σ^- bubbles, the characteristic shape of the transient bubble is used.

The sample is an implanted film of composition

$Y_{1.9}Sm_{.1}Lu_{.1}Ca_{.9}Ge_{.9}Fe_{4.1}O_{12}$ whose material characteristics are given in the Appendix F for the film P206. Other samples[11] were briefly examined to verify that the general phenomena reported here exist in other films. In particular, an as-grown film similar to the implanted film was used for comparison.

E.4 Results

The transient position of the individual wall sections of unichiral bubbles during radial expansion was observed using an optical sampling microscope with 10 nsec laser pulse illumination. The instantaneous position of the two wall sections that are parallel to a 20 Oe in-plane field is plotted as a function of time in Fig. (E.5). Also shown, on the same time scale, is the applied bias field step pulse (solid line) as well as the instantaneous drive field (□), which is calculated using the observed bubble diameter and the experimentally determined relation between the stable bubble diameter and the bias field. Only the initial step change of the pulse is significant since the pulse has a fall-time greater than 10 μsec. The displacement in a radially outward direction is plotted for the normal wall whose center spin is along the in-plane field (□) and the twisted wall, whose center spin is opposed to the in-plane field (+). The vertical bar through each symbol represents twice the standard deviation of ten measurements. The solid curves are theoretical predictions that will be discussed later. A bias step of 7 Oe is used for Fig. (E.5a) and 11 Oe for Fig. (E.5b). In Fig. (E.5a) it can be seen that the two wall sections move at very different velocities even

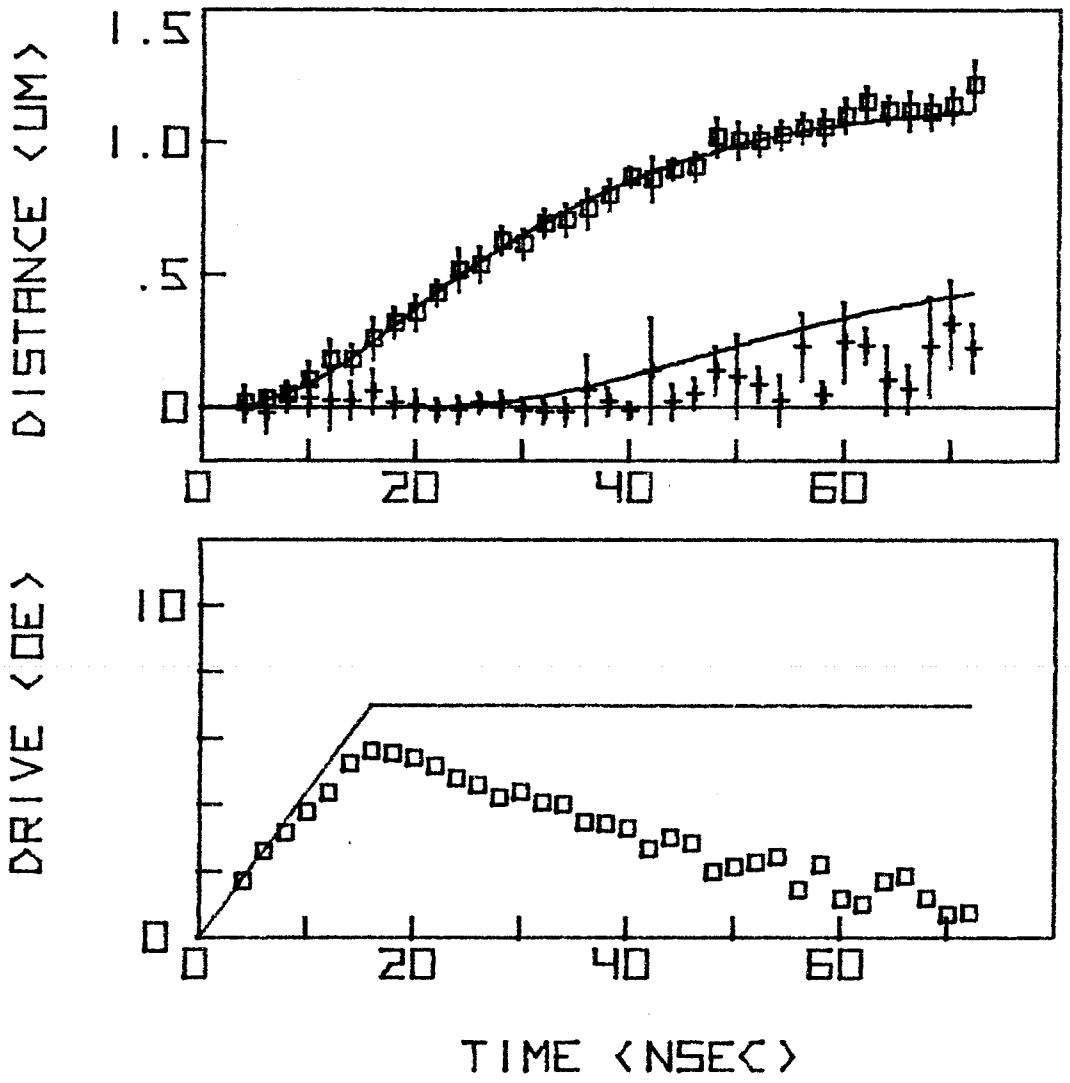

Fig. (E.5a). Displacement of the wall as a function of time after the start of a 7 Oe bias pulse. Also plotted is the instantaneous drive.

though the drive on each is identical. The slow wall has not moved perceptibly until 40 nsec after the pulse is applied. By the time the drive has dropped to 1 Oe, the normal wall has moved 1.1 μm compared with 0.3 μm for the 2π twisted wall. This asymmetric motion of the two walls is typical of both expanding and collapsing pulses of magnitudes less than 9 Oe.

The displacement of the two walls parallel to the 20 Oe in-plane field during an 11 Oe bias pulse is plotted in Fig. (E.5b) as a function of time after the start of the pulse. It can be seen that the characteristics of the motion of the normal wall (□) are essentially the same as that for the 7 Oe pulse, shown in Fig. (E.5a). The 2π twisted wall (+) shows the same initial lack of motion observed for the 7 Oe pulse, although the period of immobility is only 20 nsec. An abrupt increase in wall velocity after this 20 nsec period can be seen, which was not evident during the 7 Oe drive. The velocity jumps to a value comparable to that of the normal wall and remains at that value until the drive vanishes. This sharp transition in the motion of the 2π twisted wall to a sustained high velocity is characteristic for pulse amplitudes greater than 9 Oe.

The transition of the 2π twisted wall from an immobile wall to one having a high velocity can be correlated with bubble state conversions. State identification is made before and after a given pulse. The pulse width required to cause a χ^--to-σ^- state switch is plotted in Fig. (E.6) as a function of bias pulse amplitude. The χ^- state switches to σ^- because of the 20 Oe in-plane field; χ^+ does not switch at all because of the implanted layer. The end of the pulse is defined as the time at which the effective drive on the bubble decreases to 2.5 Oe, the

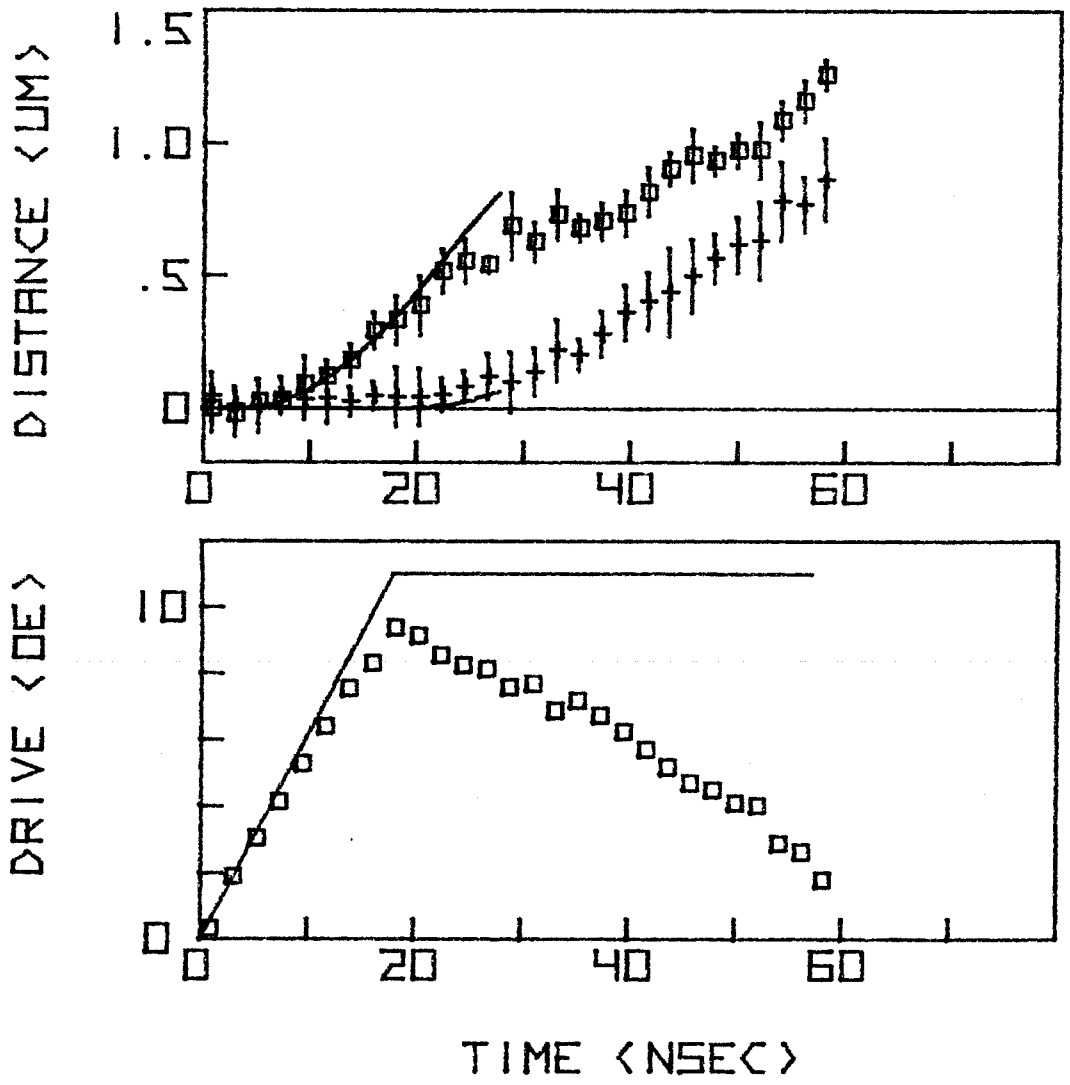

Fig. (E.5b). Displacement of the wall as a function of time after the start of an 11 Oe bias pulse. Also plotted is the instantaneous drive.

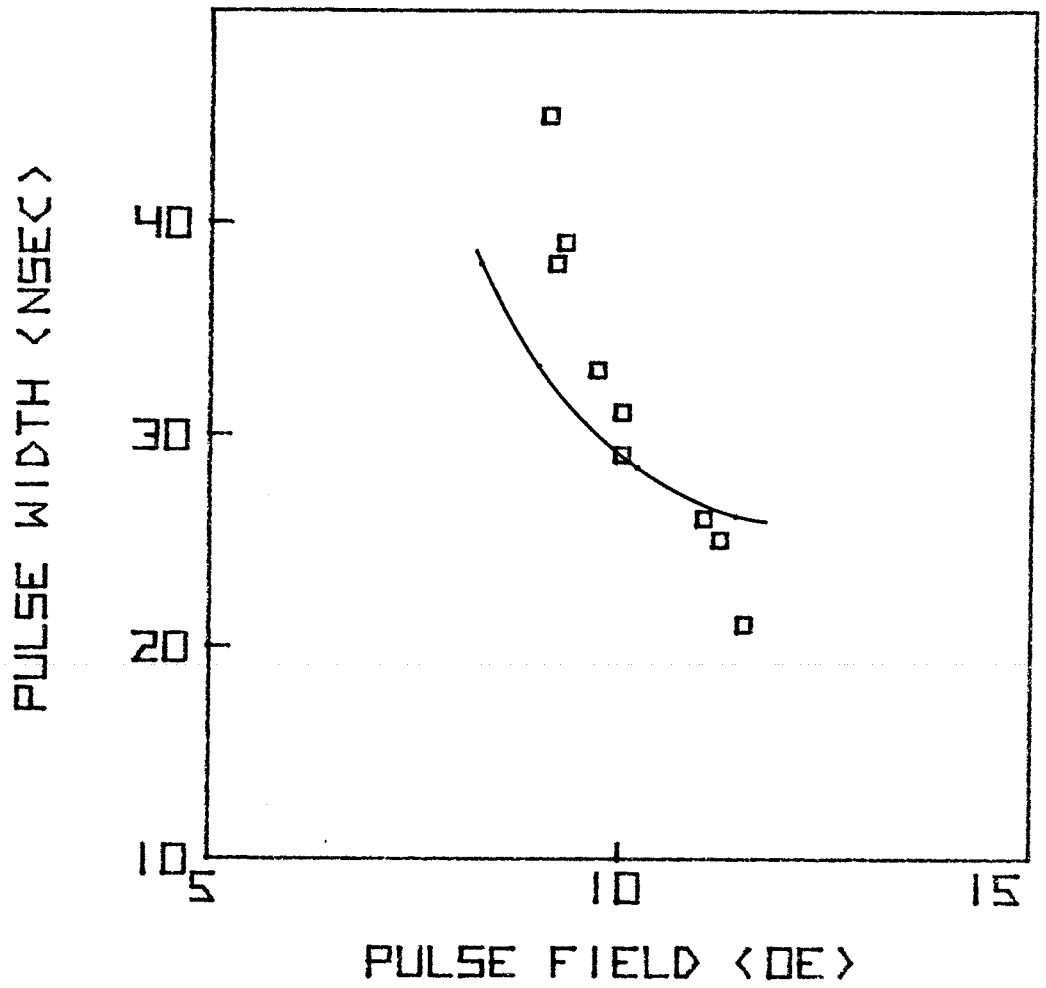

Fig. (E.6). The pulse width required to produce a χ-to-σ state switch as a function of pulse amplitude, for a 20 Oe in-plane field.

minimum drive for punch-through described earlier. In this way, the pulse width can be compared directly with theoretical predictions of the time required for punch-through of the 2π HBL. The solid line is a theoretical prediction that will be discussed later. It can be seen that pulse width for a state switch decreases sharply from 49 to 19 nsec as the pulse amplitude increases from 9.1 to 11.5 Oe. For any pulse width, state changes occur only if the pulse field is more than 8.6 Oe.

E.5 Discussion

The predicted motion of each of the walls parallel to a 20 Oe in-plane field during a 7 Oe bias pulse is shown by the solid curves in Fig. (E.5a). The motion of the normal wall (□) was predicted using the one-dimensional wall model. The resulting curve for the 7 Oe pulse lies within the error bars of each of the data points. The dynamic behavior of the 2π twisted wall section (+) was modeled using a 2π HBL. This model predicts the immobility of the wall that occurs during the first 30 nsec of the pulse, but it gives a wall displacement about a tenth of a micron too large for later times. As can be seen from the velocity versus $\overline{\phi}$ relation shown in Fig. (E.4), this initial immobility is expected to occur until $\overline{\phi}$ has developed a significant value (90^{o}) which is when the 2π HBL approaches a film surface. For the 7 Oe pulse, the largest wall velocity can be calculated to occur 46 nsec after the pulse begins, at which time $\overline{\phi}$ reaches its maximum value of 146^{o}, corresponding to a position of the HBL about 0.5 μm from the film surface. The data in Fig. (E.5a) suggests that this actually occurs at about 50 nsec, when

the effective drive drops below 2.5 Oe. Punch-through of the 2π HBL is not expected. This is consistent with the data in Fig. (E.6), showing that state conversions do not occur for pulse amplitudes less than 8.6 Oe. By comparison, $\overline{\phi}$ for the normal wall section reaches a maximum of 11^{o} at a time 18 nsec after the pulse begins. This lower rate of spin precession, as compared with that of the 2π twisted wall, is related to the higher wall velocity via Eq. (E.3). The close agreement between the data and the prediction for the normal wall shows that the uniform rotation assumption in the one-dimensional wall model is valid for the small spin precession occurring during low amplitude pulses. The initial immobility of the 2π twisted wall on the other side of the bubble is a consequence of 2π HBL motion through the central portion of the film.

The predicted motion of each of the walls parallel to a 20 Oe in-plane field during an 11 Oe bias pulse is shown by the solid curves in Fig. (E.5b). The predicted motion of the normal wall (□) is close to the actual motion only for the first 20 nsec, after which a large deviation exists. This breakdown of the one-dimensional model is expected on the basis of results obtained from more accurate numerical calculations of the kind used in the analysis of the dynamics of the 2π twisted wall. When that numerical procedure is applied to the normal wall, it is found that the one-dimensional model is only appropriate for values of $\overline{\phi}$ less than 21^{o}. Above this value, numerical calculations show that HBL nucleation occurs, so that the wall structure will clearly not remain one-dimensional. For the 11 Oe pulse, a break in velocity occurs 20 nsec after the pulse begins, at which time $\overline{\phi}$ is 18^{o}. This value of $\overline{\phi}$ roughly agrees with the predicted breakdown angle of 21^{o}. The normal

wall motion, therefore, shows agreement with the one-dimensional model before the breakdown to HBL motion at the expected threshold.

For the moving 2π twisted wall (+), the 2π HBL model predicts that the 2π HBL punches through the film surface at about 27 nsec after the start of the pulse, with the wall structure converting to one typical of the normal wall. It can be seen in Fig. (E.5b) that the wall velocity increases significantly at the time punch-through is expected to take place, showing that the 2π HBL has indeed been annihilated. This is supported by the data in Fig. (E.6), which shows that a switch to a σ state occurs whenever an 11 Oe pulse has a width greater than 26 nsec. The increased wall velocity after punch-through is thought to be due to the nucleation and propagation of the standard type of HBL's that cause the saturation velocity, as in the normal wall. No prediction of the wall displacement was made for this situation because the existing analytical model[10] does not include the effects of an in-plane field, and the numerical procedure described earlier cannot be applied successfully to this case.

After punch-through occurs, the vertical part of the twisted wall remains; the two VBL's travel to opposite ends of the bubble under the influence of the in-plane field, thus forming a σ state. The results of the numerical calculation for the pulse width required to convert a χ to a σ state for a given pulse amplitude are shown by the solid curve in Fig. (E.6). It can be seen that good agreement is obtained, particularly for the higher pulse fields. The minimum pulse field able to produce a state switch is calculated to be 8.03 Oe, in agreement with the 8.6 Oe experimental value mentioned earlier.

Annihilation of the entire 2π HBL during punch-through does not occur instantaneously. The tilt of the 2π HBL implies that the portion of the HBL statically located nearest the film surface will take a shorter time to reach the surface than another portion. Therefore, the conversion to a normal wall at punch-through occurs first at a particular wall section. Because this conversion is associated with an increase in wall velocity, it is evident that an asymmetric bubble shape occurs as the velocity increases at different times along the bubble perimeter. Such an asymmetric transient shape, caused by the tilt of the 2π HBL, is indeed observed.

E.6 Conclusions

The asymmetric radial expansion of unichiral bubbles in the presence of a 20 Oe in-plane field, as observed by transient photography, demonstrates the presence of different spin structures in the two wall sections parallel to the in-plane field. The in-plane field reduces the twist in the normal wall section, whose center spin is along the in-plane field, resulting in velocities characteristic of one-dimensional walls. In the wall section whose center spin is opposed to the in-plane field, a 2π HBL is nucleated for in-plane fields above the 12 Oe threshold, causing this wall section to be essentially immobile. The application of a one-dimensional model to the normal wall and a numerical finite difference approach to the 2π twisted wall gives results in general agreement with experiment. Bubble state conversions are caused by punch-through of the 2π HBL, which leaves two opposite-winding VBL's.

References

1. T. M. Morris, G. J. Zimmer, and F. B. Humphrey, J. Appl. Phys. 47, 721 (1976).
2. Kochan Ju, G. J. Zimmer, and F. B. Humphrey, Appl. Phys. Lett. 28, 741 (1976).
3. T. J. Gallagher and F. B. Humphrey, J. Appl. Phys. 50, 997 (1979).
4. A. Hubert, J. Appl. Phys. 46, 2276 (1975).
5. T. J. Beaulieu, B. R. Brown, B. A. Calhoun, T. Hsu, and A. P. Malozemoff, AIP Conf. Proc. 34, 138 (1976).
6. T. J. Gallagher and F. B. Humphrey, J. Appl. Phys. 50, 7093 (1979).
7. B. E. Argyle, S. Maekawa, P. Dekker, and J. C. Slonczewski, AIP Conf. Proc. 34, 131 (1976).
8. N. L. Schryer and L. R. Walker, J. Appl. Phys. 45, 5406 (1974).
9. H. C. Bourne and D. S. Bartran, IEEE Trans. MAG-10, 1081 (1974).
10. J. C. Slonczewski, J. Appl. Phys. 44, 1759 (1977).
11. G. J. Zimmer, L. Gal, and F. B. Humphrey, J. Appl. Phys. 46, 4976 (1975).

Appendix F

Table of Material Characteristics of the Garnet Films

Sample number	$4\pi M$ (Oe)	γ ($Oe^{-1}sec^{-1}$)	H_k (Oe)	α	h (μm)
2-16-44	184.4	1.1×10^7	3082	0.026	6.8
2-12-63	205	1.1×10^7	3399	0.029	6.9
P206	180	1.83×10^7	1520	0.14	4.1
P197	--- nominally identical to P206 -------				
F19 series	289	1.79×10^7	1310	0.13	3.4

Films 2-12-63 and P206 were implanted at 80 keV with a dosage of $2 \times 10^{14}/cm^2$, while the series F19 was implanted with the same dosage at 100 keV.

For all the films, the exchange constant is taken to be $A = 2 \times 10^{-7} erg/cm$.